POLITECNICO DI TORINO

MECHANICAL ENGINEERING

Master degree thesis

Preliminary design of an additively manufactured micro piezoelectric energy harvester for a rechargeable pacemaker

Supervisor:

Prof. Eugenio Brusa

Author:

Enrico Tagliaferri

2019

SUMMARY

ABSTRACT

The thesis wants to study the most recent developments in additive manufacturing for micro scale components. An introduction presents the main additive manufacturing technologies and subsequently an approach to study the possibility of determining the level of micro scale reachable by the techniques is shown. In the following chapters, an overview of the different types of materials involved by this research field is presented, with attention on the articles in literature showing the most interesting and various aspects. Obviously, with this approach some important works are not analyzed, but this is anyway not avoidable because of the great amount of studies made in recent years.

An example of totally additively manufactured device with micro size features is provided. Finally, a project about the preliminary design of a piezoelectric-based energy harvesting micro system is presented. This device is aimed at recharging a pacemaker, making unnecessary the presence of a battery, that usually requires the substitution of the whole medical implant every 10 years.

1. INTRODUCTION

1.1. GENERALITIES

Additive manufacturing (AM), also known as layered manufacturing, indicates the process in which a part is produced by adding material layer-by-layer. Rapid prototyping stays, instead, for a rapid process of production before commercialization. Hence, it is a sub-group of AM techniques.

AM technologies require five main steps in production [1, 2]:

1. Elaboration of the CAD model as input for the machine;
2. Conversion of the CAD model in STL format;
3. Slicing of the STL model in horizontal layers;
4. Printing the part layer-by-layer;
5. Post-processing the part.

The physical state of the starting material can be a criterion of classification of the AM technologies. It can be solid (polymeric, metallic, composited) to enhance mechanical properties, liquid (polymeric) to enhance the surface finish, powdered (polymeric, metallic, ceramic).

The main advantages of the concept of AM are:

- Economic production
- Fabrication of complex geometries
- Spare of time in prototyping and production

- High level of automation with subsequent few possible human errors and not high-skilled required personnel
- High material use efficiency
- Low environmental impact

Drawbacks of AM technologies are:

- A lot of required time for producing large-sized parts
- Low surface finish quality
- High cost of the machine

According to the printing principle, AM technologies can be collected in different families, that are clarified in table 1.1, although continuous innovations and implementations create hybrid machines and the classification is without clear boundaries, hence a technology can be seen as belonging to two different families.

Table 1.1. *Families of AM technologies*

Family	**AM technology**
Binder Jetting	DOP (Drop On Powder)
	3DP
Direct Energy Deposition (DED)	LENS
	EBF^3
	LMD
Material Extrusion	FDM
	FDC
	DIW
	APF (Arburg Plastic Freefroming)
Material Jetting	DOD
	CIJ
	EIJ

	LIFT (Laser Induced Forward Transfer)
	PolyJet
	MJM
	SGC
Powder Bed Fusion (PBF)	SLS
	SLM
	DMLS
	SHS
	EBM
	3DP
Sheet Lamination	LOM
	UAM (Ultrasonic Additive Manufacturing)
Vat Polymerization (VP)	SLA
	DLP (Digital Light Processing)
	CLIP
	DLW
	2PP

The main additive manufacturing technologies, that can be implemented or adapted in order to obtain micro scale components, are listed and briefly described in this chapter [3-12].

1.2. FDM (FUSED DEPOSITION MODELING)

A spool gives a thermoplastic polymer in the form of two filaments (one for the build material and the other one for the support material) to a horizontally-moving extrusion head, that is provided with two liquefiers that melt the filaments at a temperature slightly above their melting points and two extrusion nozzles that are placed on top of the vertically-moving build platform. Solidification of the material occurs immediately after extrusion and, after it, the support material has to be removed. The system can be evolved in order to process metals, ceramics (in this case the technique takes the name FDC, that stays for Fused Deposition of Ceramics) and composites.

It is also known as FFF (Fused Filament Fabrication). Implementations of this technology have brought to EPAM (Electric Poling-assisted Additive Manufacturing). DIW (Direct Ink Writing), also known as Robot Casting, differs from FDM because the extrusion head does not move and the build platform, where the product is printed on, moves vertically and horizontally.

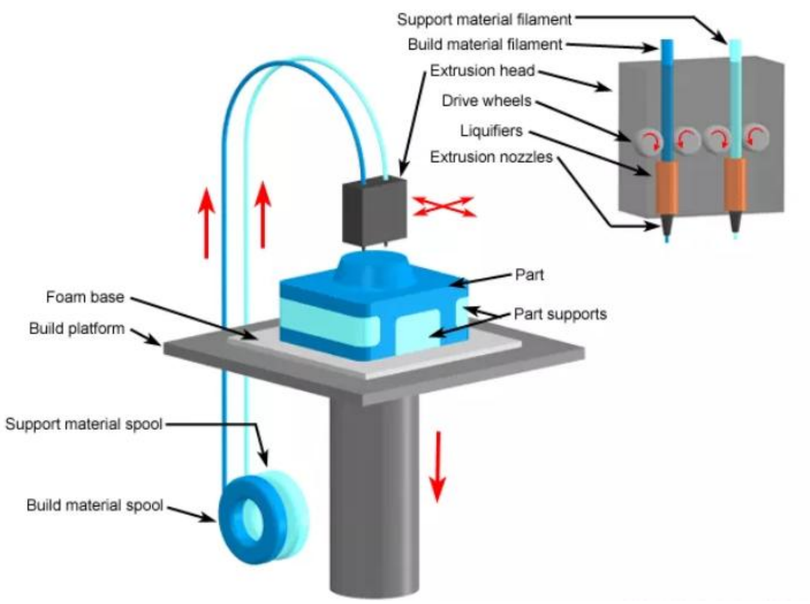

Figure 1.1. *FDM scheme [13]*

1.3. LOM (Laminated Object Manufacturing)

A thin sheet of paper, metals, thermoplastics, fabrics, synthetic materials or composites is wrapped in a supply roll that gives the material, after it is heated, to the build platform, where a laser beam designs the slice taken from the STL file on the sheet, thus creating the layer of the part. A second roll retrieves the recyclable wasted part of the sheet, that acts as support material. The sheet is adhesive thanks to the increase of temperature because of the laser, to the pressure between two subsequent layers and to the presence of a thermal adhesive coating.

The build platform moves vertically, while an optic head moves horizontally in order to address, with the help of a mirror, the laser beam to the desired position. This technique combines additive with subtractive manufacturing.

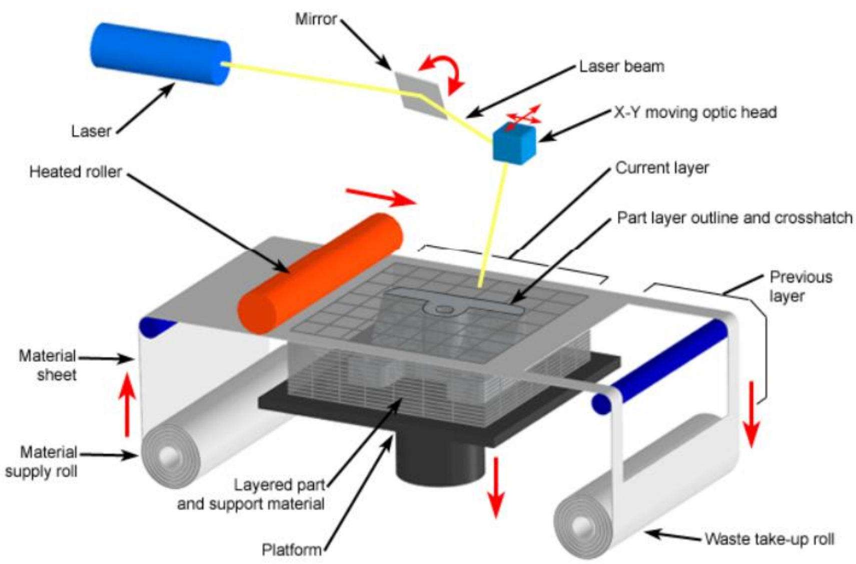

Figure 1.2. *LOM scheme [14]*

1.4. LENS (LASER ENGINEERED NET SHAPING)

The vertically-moving head has got a double function: it addresses the laser beam in order to melt the metal powder and it delivers the material through an argon pressurized nozzle on a support on top of a horizontally-moving build platform. After solidification the support material has to be removed. A wire or filament form feed material can be adopted.

It is also known as LMD (Laser Metal Deposition), DMD (Direct Metal Deposition), DLD (Direct Laser Deposition), LDW (Laser Deposition Welding), LSF (Laser Solid Forming), DLF (Directed Light Fabrication), EBDM (Electron Beam Direct Manufacturing) and PFW (Powder Fusion Welding). EBF^3 (Electron Beam Freeform Fabrication) differs from LENS because it uses an electron beam instead of a laser beam and it requires an environment in which vacuum has been created.

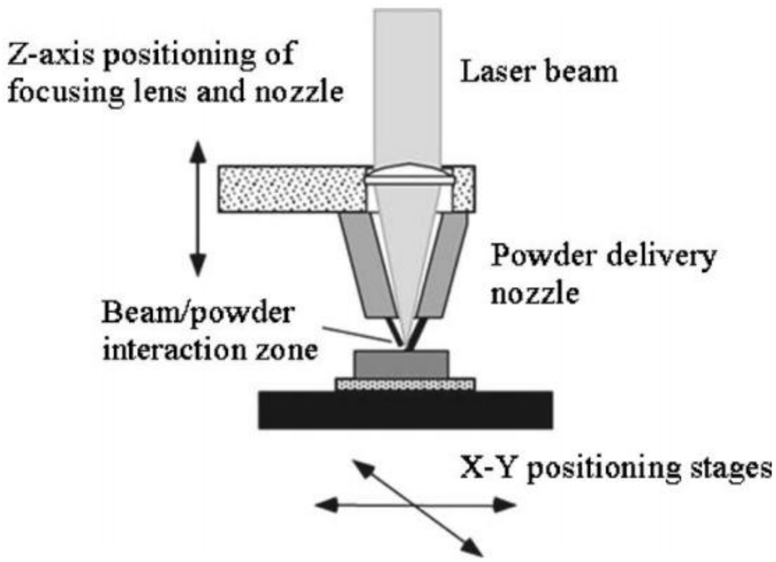

Figure 1.3. *LENS scheme [15]*

1.5. 3DP (THREE DIMENSIONAL PRINTING)

It is a Binder Jetting, but it can be evaluated as a PBF technique using a liquid binder. A roller distributes the powder (the material can be ceramic, metal, polymer, composite) on the vertically-moving build platform and a horizontally-moving inkjet head sprays the binder in order to aggregate the particles. Thermal post process is usually required for the binder and the non-processed powder acts as recyclable support material.

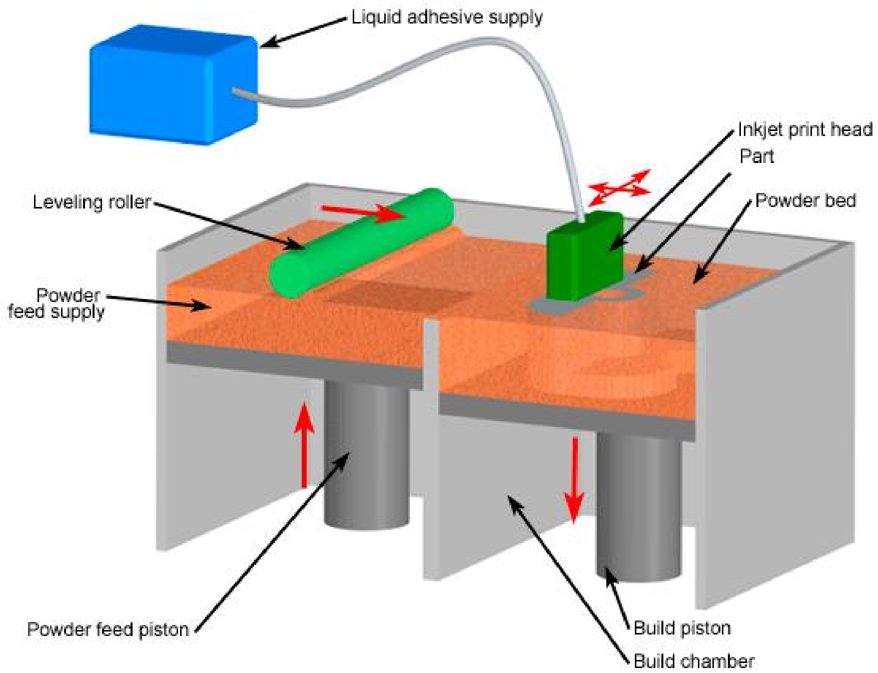

Figure 1.4. *3DP scheme [16]*

1.6. SLA (STEREOLITHOGRAPHY APPARATUS)

A UV laser beam is deviated by a mirror in order to hit in the desired point a photo polymerizable liquid resin contained in a vat where a vertically-moving build platform is immersed and prepared with supports to be removed after the solidification of the part. When every layer is completed, a sweeper levels the resin and the next layer can be generated. After the printing of the last layer, the product is placed in a UV oven in order to solidify also the internal regions that are still filled with liquid resin, because the laser beam hits only the external perimeter of the component to save production time.

It is also known simply as SL (StereoLithography). Implementations from this technology have brought to DLW (Direct Laser Writing), also known as Direct Laser Lithography or Multiphoton Lithography, and CLIP (Continuous Liquid Interface Production), that is faster. 2PP (Two-Photon-Photopolymerization), also known as TPL (Two Photon Lithography), differs from SLA because it simultaneously uses two photons, instead of only one, in order to get higher resolution.

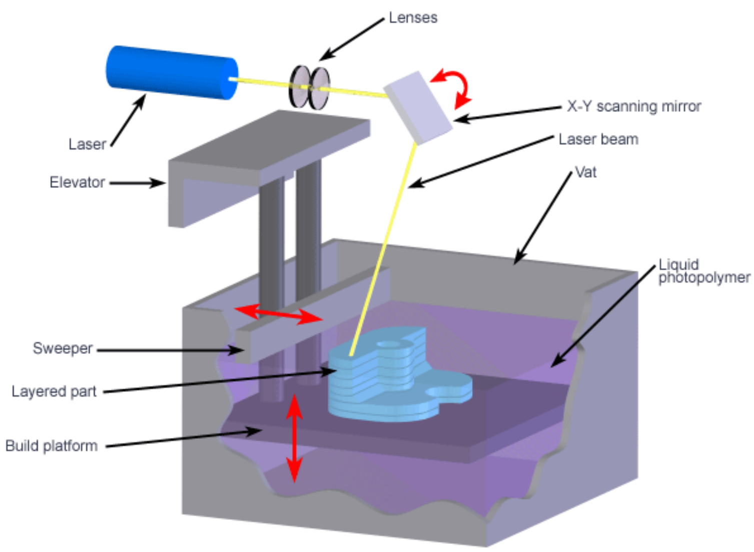

Figure 1.5. *SLA scheme [17]*

1.7. SLS (Selective Laser Sintering)

A roller distributes the powder (the material can be ceramic, metal, thermoplastic polymer, composite) on the vertically-moving build platform and a mirror deflects a laser or electron beam in the desired point in order to sinter the particles. The non-processed powder acts as recyclable support material and to avoid oxidation an inert environment is required.

It is also known as DMLS (Direct Metal Laser Sintering) when the processed material is a metallic alloy. Implementations from this technology have brought to SHS (Selective Heat Sintering) that has got a heated head instead of the laser, SLM (Selective Laser Sintering) that does not sinter, but melts metallic particles, EBM (Electron Beam Melting) that is equivalent to SLM but it uses an electron beam and it requires an environment in which vacuum has been created.

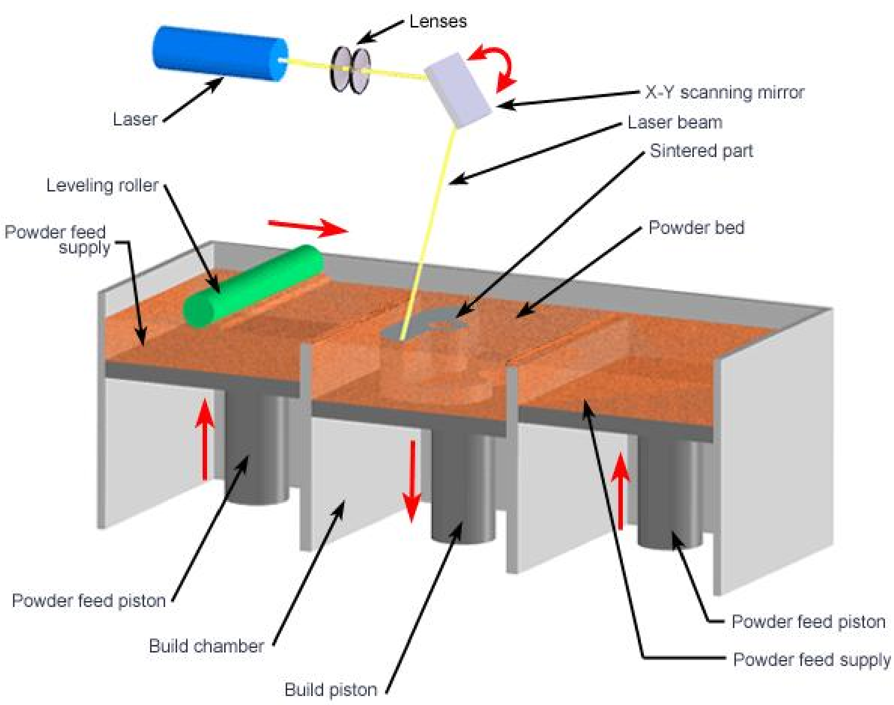

Figure 1.6. *SLS scheme [18]*

1.8. IJP (INKJET PRINTING)

This is a transversal sub-family of additive manufacturing techniques belonging to material jetting family and binder jetting family and it is also known simply as inkjet or more generally as inkjet technology or inkjet printing. It includes for example DOD (Drop On Demand Inkjet Printing), CIJ (Continuous Inkjet Printing) and EIJ (Electrostatic Inkjet Printing). The liquid material (polymer, ceramic, metal) is kept in heated reservoirs and then dispensed by two horizontally-moving inkjet print heads (one is for the build material and the other one is for the support material) on the vertically-moving build platform. The liquid drop solidifies rapidly and when a layer is generated, a plane milling head levels the surface, so that next layer can be deposited.

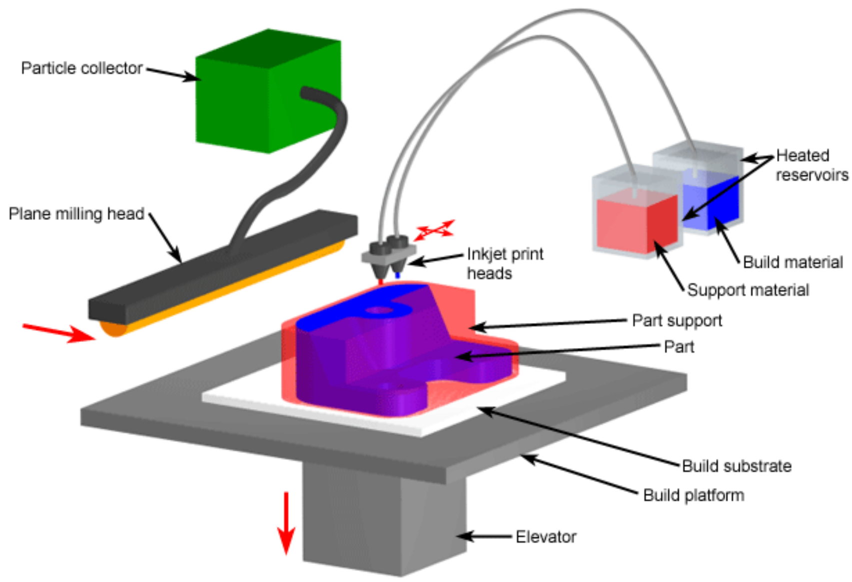

Figure 1.7. *IJP scheme [19]*

SGC (Solid Ground Curing), that can be also evaluated as a vat polymerization technique, is an implementation where a curing UV lamp is needed in order to polymerize the deposited photopolymer ink with the help of a transparent sheet that acts as shield when, for each layer of the part to be produced, a black powder is electrostatically and appropriately adhered to it. Similar to this is PolyJet (the commercial name of Photopolymer Inkjet Printing) that does not use a mask but supports: it jets and cures the material where needed. Implementations from this technologies have brought to MJM (Multi Jet Modeling), also known as MJP (Multi Jet Printing).

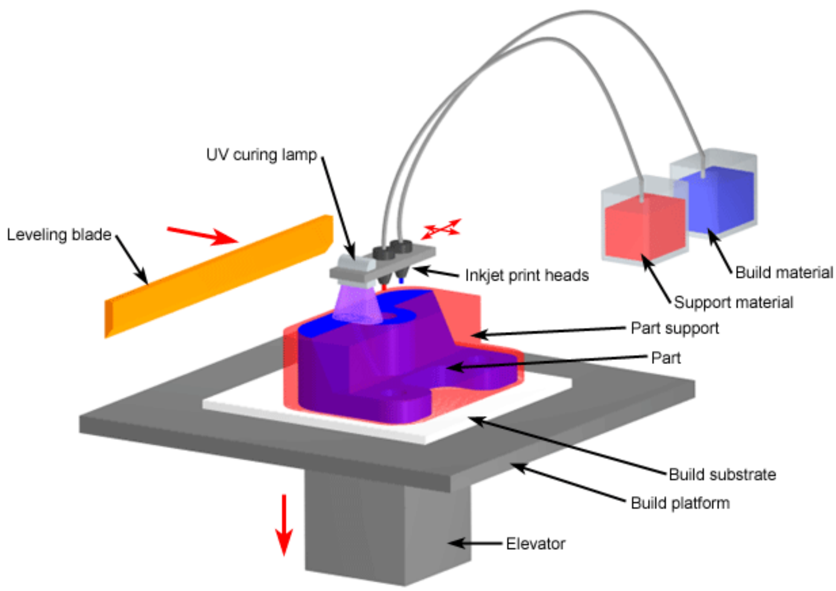

Figure 1.8. *SGC scheme [20]*

2. APPROACH TO THE MICRO SCALE

Before starting with the different types of materials and relative main technologies for micro AM components, an analysis about the approach to the micro scale is performed. Some works are considered and used as examples to explain how parameters of a technology can reach a certain level of accuracy when scale of the final parts is miniaturized.

When dealing with micro features, the first aspect to be considered is the presence of a large supporting test piece where the parts can be printed, in order to avoid the possibility of losing the features [21]. The macro scaled support is required by processes where features can be lost in the resin, such as vat polymerization techniques, where gravity hold in place the voxels (i.e. the smallest printable volumetric elements), such as binder jetting and powder bed fusion, or where voxels must adhere to a supporting surface, such as material extrusion.

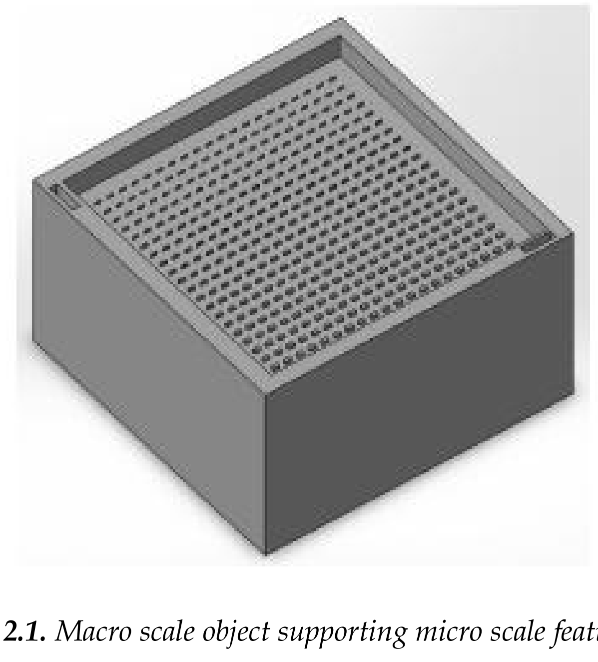

Figure 2.1. *Macro scale object supporting micro scale features [21]*

The minimum possible feature size in micro additive manufacturing is related to the voxel, that can be calculated for many AM technologies. However, analytical models do not take in consideration some important factors. Moreover, hardware used in the machines may are not known, there are some variations quality and workflow from a machine to another one for the same process and there could be vibrations and fluctuations in environmental humidity and temperature. Hence, precision and resolution of a machine can not be revealed without an experimental procedure.

In this work, Thompson and Mischkot (2015) [22] studied cubic features with sides between 5 and 100 μm produced by digital light processing (DLP) 3D printing, whose manufacturer reported 16x16x15 μm^3 as minimum voxel size.

In design, the first step is identifying the stakeholder, whose needs are then converted in requirements. Constraints must be taken into account. Solutions are searched and the best one will be used as a prototype for development. The difficulty consists in understanding the interactions between process variables, design parameters and functional requirements. To solve this problem, design iteration can be useful.

A first test consists in reproducing in the center of the part in figure 2.2 three sets of cubic features with different sizes.

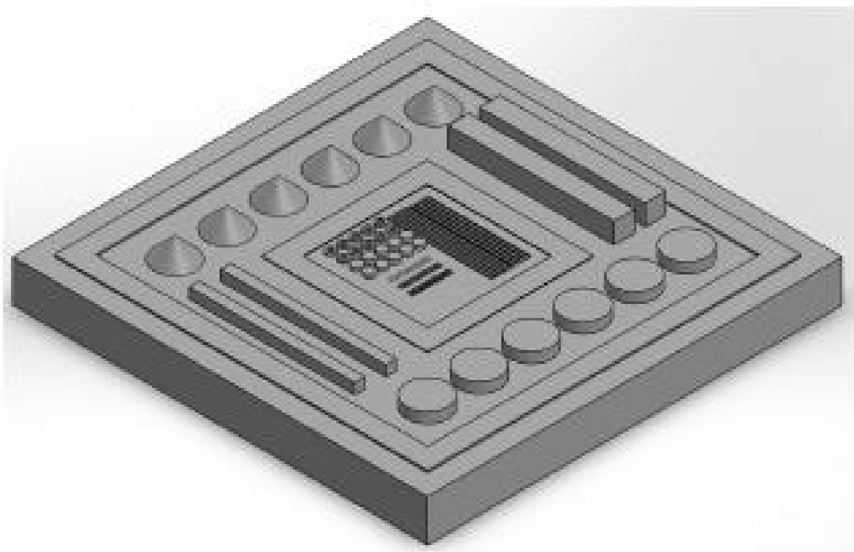

Figure 2.2. *First test part model [22]*

The dimensions of the first set are 16x16x15 μm³ and this wants to represent the single voxel, being the minimum layer thickness of the machine 15 μm and the pixel size 16 μm. The second set represents two voxels features with dimensions of 32x32x30 μm³ and the third set three voxels features of 48x48x45 μm³. The spacing between the features decreases with the size of the features because it is kept constant between the upper left corners of two subsequent features. The spacing are therefore 84, 68 and 52 μm for the three sets. The third set presents a problem, because there was resin entrapped between the features, showing that spacing was too small. The solutions to this problem are the increasing of the spacing, the improving of the post-process or the choose of a less viscous resin. Another problem is related to the first set, that is not printed: voxel size of the machine can not be confirmed experimentally.

In the second iteration, in order to avoid problems as in the first one, the spacing between the features is increased. In the part there are 12 sets of 25 cubes starting from dimensions of 10x10x10 μm³ and incrementing the size of 5 μm every set until the dimensions of 65x65x65 μm³ in the last set.

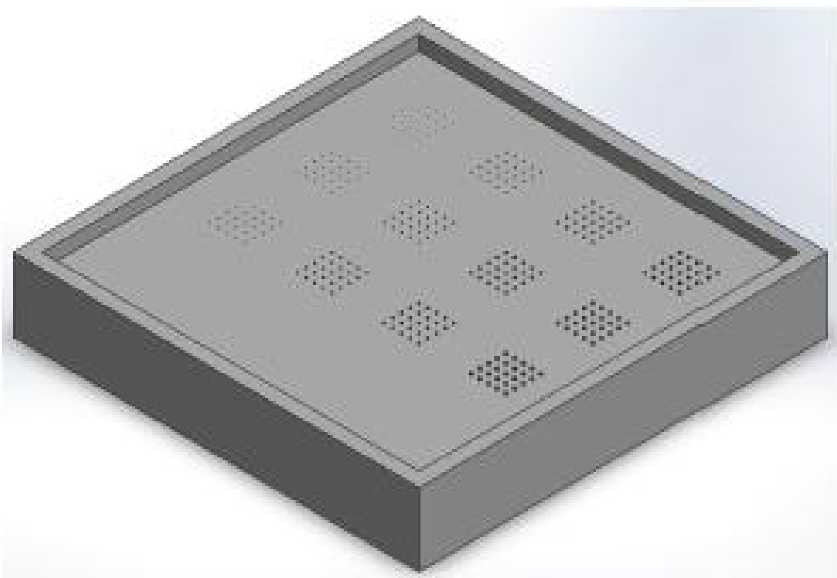

Figure 2.3. *Second test part model [22]*

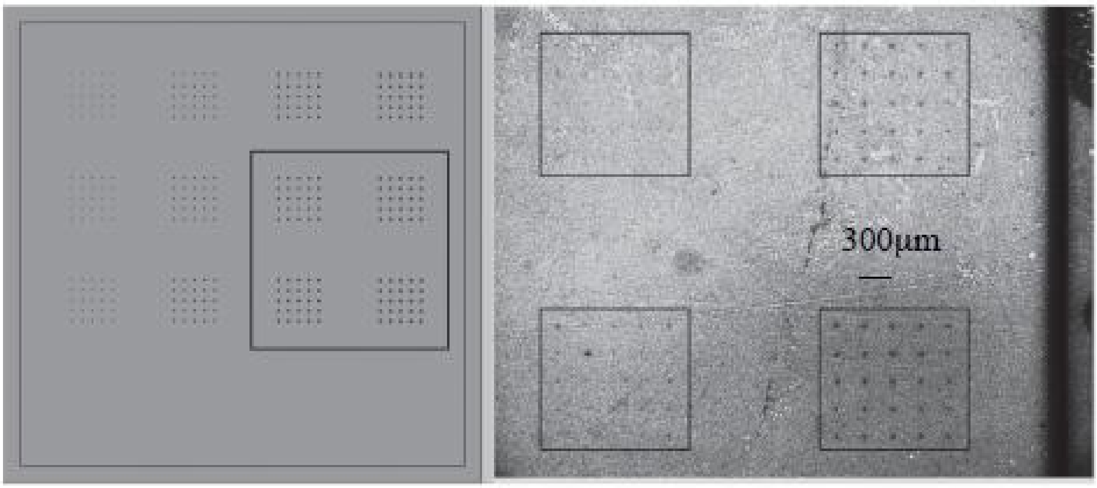

Figure 2.4. *Second design iteration: solid model (left) and magnification of four sets of 25 3D printed features (right) [22]*

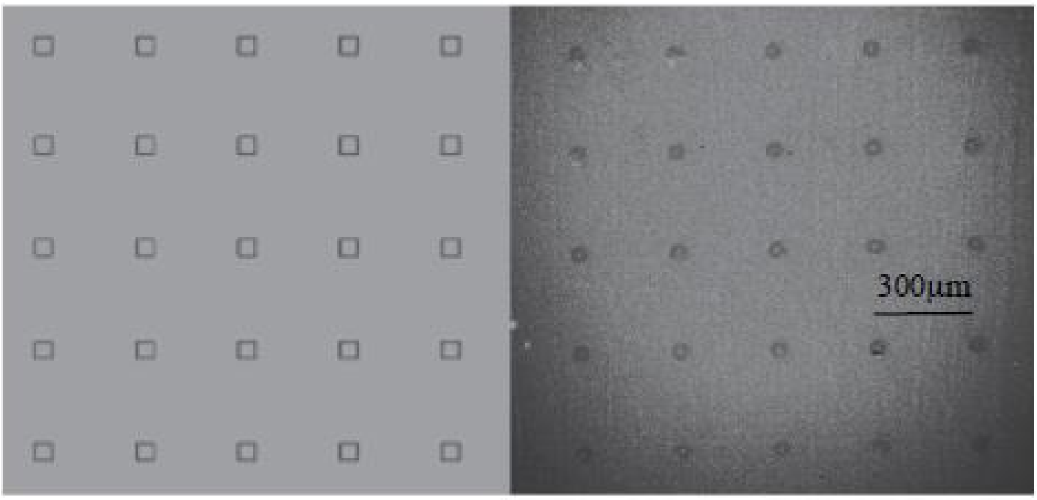

Figure 2.5. *25 features (65 μm cubes) from second design iteration: solid model (left) and 3D printed features (right) [22]*

The minimum effective spacing in this design iteration turns out to be 235 μm (higher than in the first iteration). Many of the smallest features do not print and so also the half of the features with 40 μm^3 size. Moreover, the smallest features show surface damage and debris. In the second iteration it was not possible to identify the minimum voxel size of the machine (EnvisionTEC).

For the third iteration, some changes are adopted to avoid previous problems. The support of the features was designed to facilitate the handling of the part itself and two channels on the border indicate the Cartesian axes. Features are organized in 20 rows with 20 features per row, with a spacing between upper left corners of two subsequent features of 400 μm (minimum effective spacing is 200 μm).

Every feature has the two main dimension fixed and the smallest one variable, in order to avoid coupling between dimensions. Three test samples are performed: x sample features with increment of 5 μm from 5 μm to 100 μm in “X” dimension (Xx200x100 μm^3); y sample features with increment of 5 μm from 5 μm to 100 μm in “Y” dimension (200xYx100 μm^3), z sample features with increment of 1 or 5 μm from 5 to 68 μm in “Z” dimension (200x200xZ μm^3).

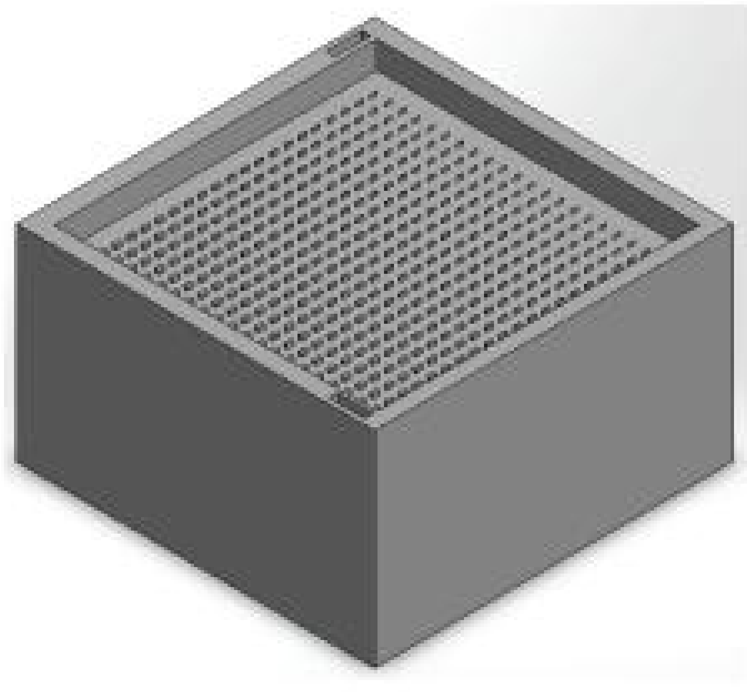

Figure 2.6. *Third test part model [22]*

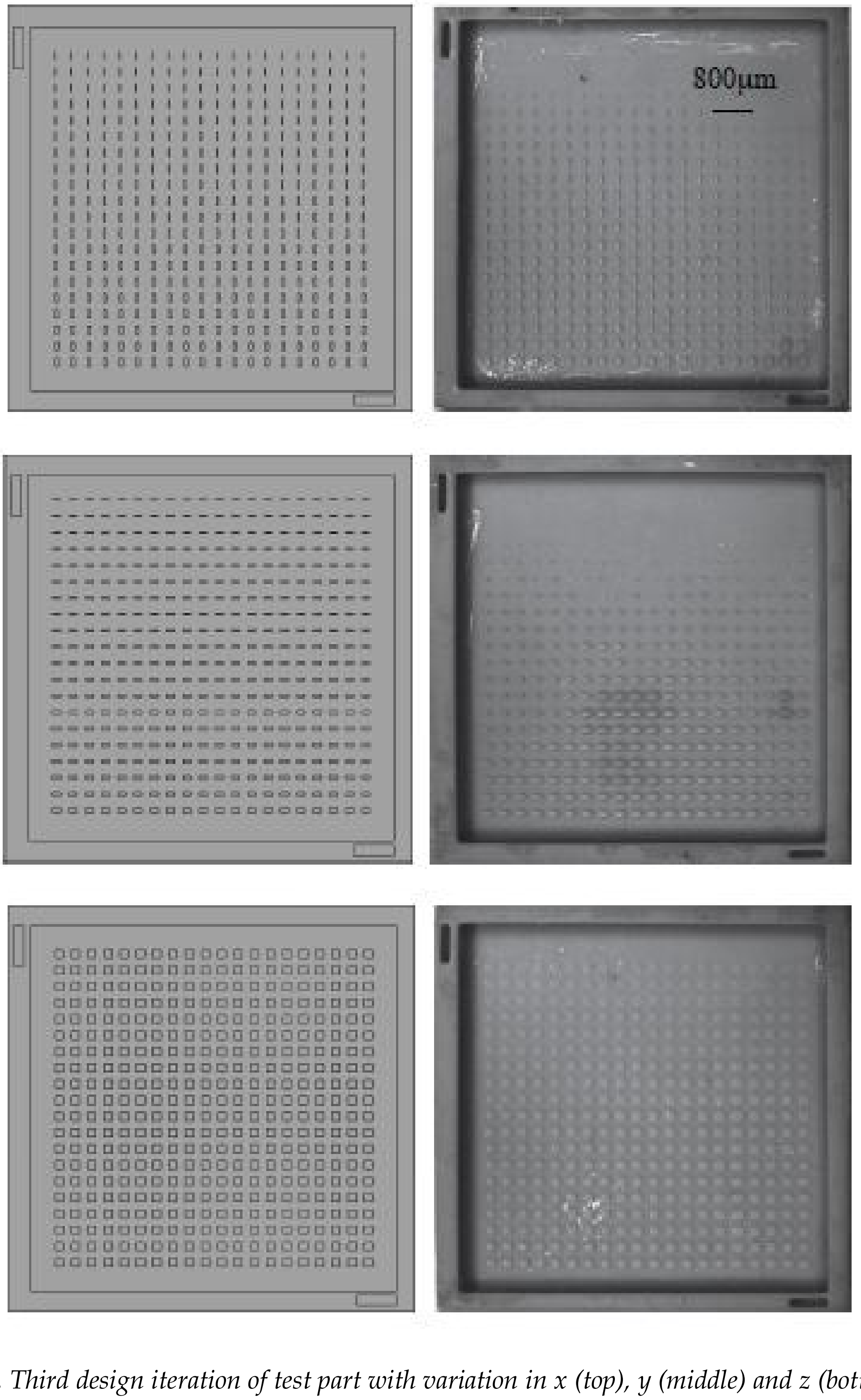

Figure 2.7. *Third design iteration of test part with variation in x (top), y (middle) and z (bottom): solid model (left) and 3D printed samples (right) [22]*

Figure 2.8 shows a horizontal cross section of the support were features are not present: only roughness can be seen.

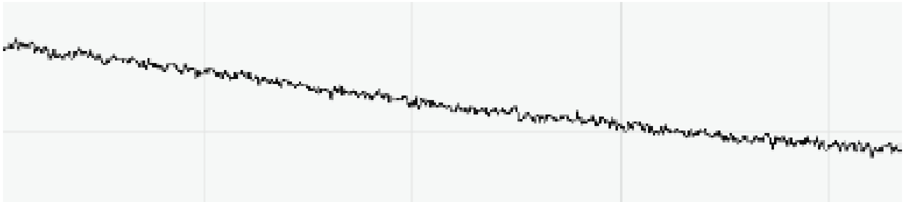

Figure 2.8. *8 mm long horizontal cross section in a featureless region. Slope represents real surface form [22]*

Figure 2.9 is a horizontal cross section with features with similar roughness and form: all features are printed.

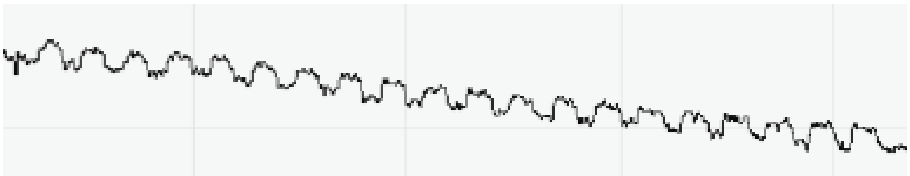

Figure 2.9. *8 mm long horizontal cross section through one row of test features with design dimensions of 200x200x10 μm³. Slope represents real surface form [22]*

Figure 2.10 is a vertical cross section of increasing size features: the smallest feature is not printed.

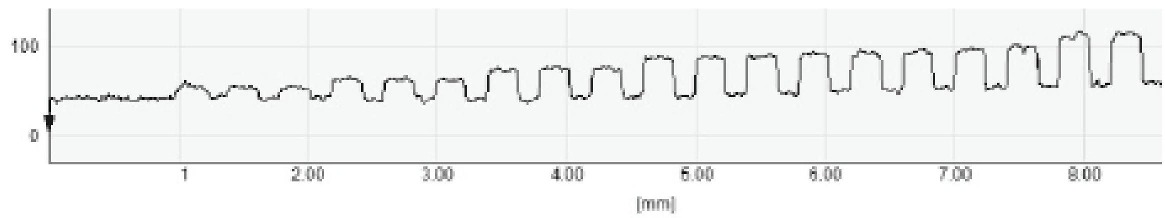

Figure 2.10. *Vertical cross section through one column of test features with dimensions of 200x200xZ μm³ [22]*

The third iteration is easier to measure because the orientation is helped by the axes in the support. Results show that the minimum layer thickness is even smaller than 15 μm, length or width of 10 μm can be printed and the shape is more accurate as the height of the feature increases.

From the first to the third iteration there is a decreasing in the minimum printable size because coupling in the part reduces and this offers the possibility to overcome manufacturer’s data of the machine. Without the removal of coupling, the printing process would be worse than expected.

This approach underlines that machine parameters are to be experimentally evaluated, following criteria that try to separate different factors influencing the performance of the machine. Hence, it is important to prepare the production of the prototype with the correct parameters of the machine, i.e. the ones got experimentally.

3. POLYMERS

3.1. GENERALITIES

Polymers find a wide range of possible production technologies and applications. The most used additive manufacturing technique for polymers is vat polymerization, that is a “scalable method”, meaning it is useful in normal-size and in micro-size manufacturing.

3.2. HPBBJ

Silicone (polysiloxane) is a polymeric material with a large number of applications in biomedical field and it has been widely studied for micro scale applications. Liravi et al. (2018) [23] studied a new technology to produce micro-size silicone parts by additive manufacturing. This method combines material extrusion and powder bed binder jetting, focusing on the critical issue in printing silicone: the viscosity.

High viscosity allows the material to maintain its structure after printing through the interaction with the substrate, not flowing on the surface; additionally, more viscous polymers have longer chains, showing better mechanical properties. However, long polymer chains and thermoset polymers can suffer an irreversible polymerization and this makes them unsuitable for many additive manufacturing techniques. A compromise is needed.

A key concept about viscosity is that the material should have a shear thinning behavior (fig. 3.1) in order to make extrusion and jetting possible and to allow the part to maintain its structure after the printing process.

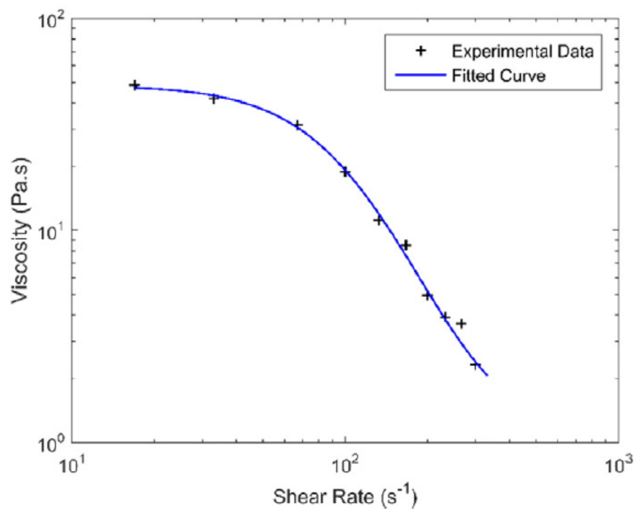

Figure 3.1. *Example of shear-thinning behavior in a logarithmic scale plot [24]*

The main used technologies for silicone are:

- material extrusion, with a resolution of 100 µm;
- stereolithography, with a resolution of 2 mm;
- aerosol jetting, with a resolution of 30 µm.

The work focuses on a new method: hybrid powder bed binder jetting (hybrid PBBJ). It is different from PBBJ because it feeds material through three nozzles able to print at the same time different powder compositions, it provides liquid binders through thermal and piezo printheads, it has got a system to compact the powder and a micro-dispensing head to fill with liquid the porous matrix of the parts.

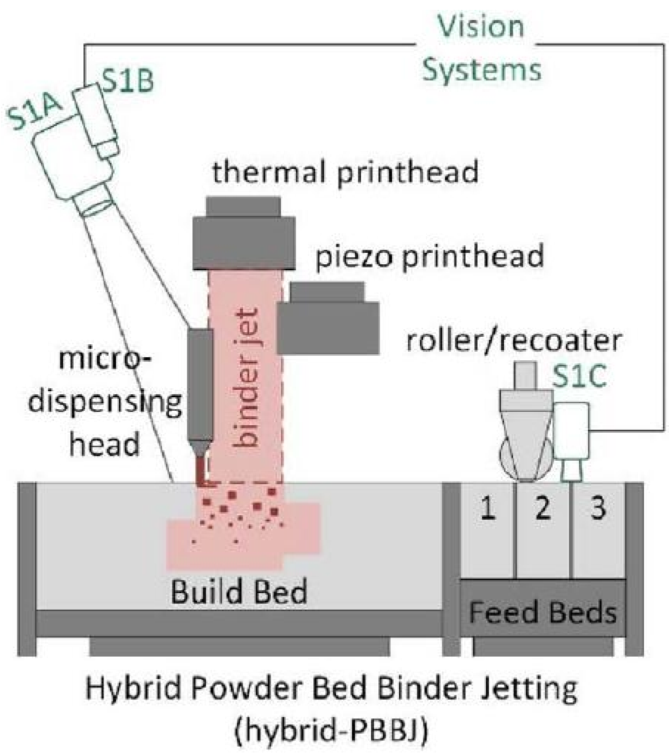

Figure 3.2. *Scheme of the hybrid PBBJ AM system [23]*

It shows some advantages:

- wide plethora of printable materials;
- feasible complex geometries, multi-material, multi-colour and scalable parts;
- high production speed.

PBBJ AM system takes a CAD model and slices it layer by layer programming the execution steps, that are four as shown in figure 3.3:

1. a roller spreads the silicone powder from the field bed to the building bed in order to get a flat layer with constant thickness;
2. the thermal printhead jets the binder (Zb60, an aqueous liquid binder) on the silicone powder substrate in precise locations according to the CAD model in order to get the layer of the part;
3. the nozzle jets the silicone droplet that infiltrates the substrate;
4. polymerization occurs by exposing the silicone binder solution to the thermal lamp for 1 minute at 100-120°C.

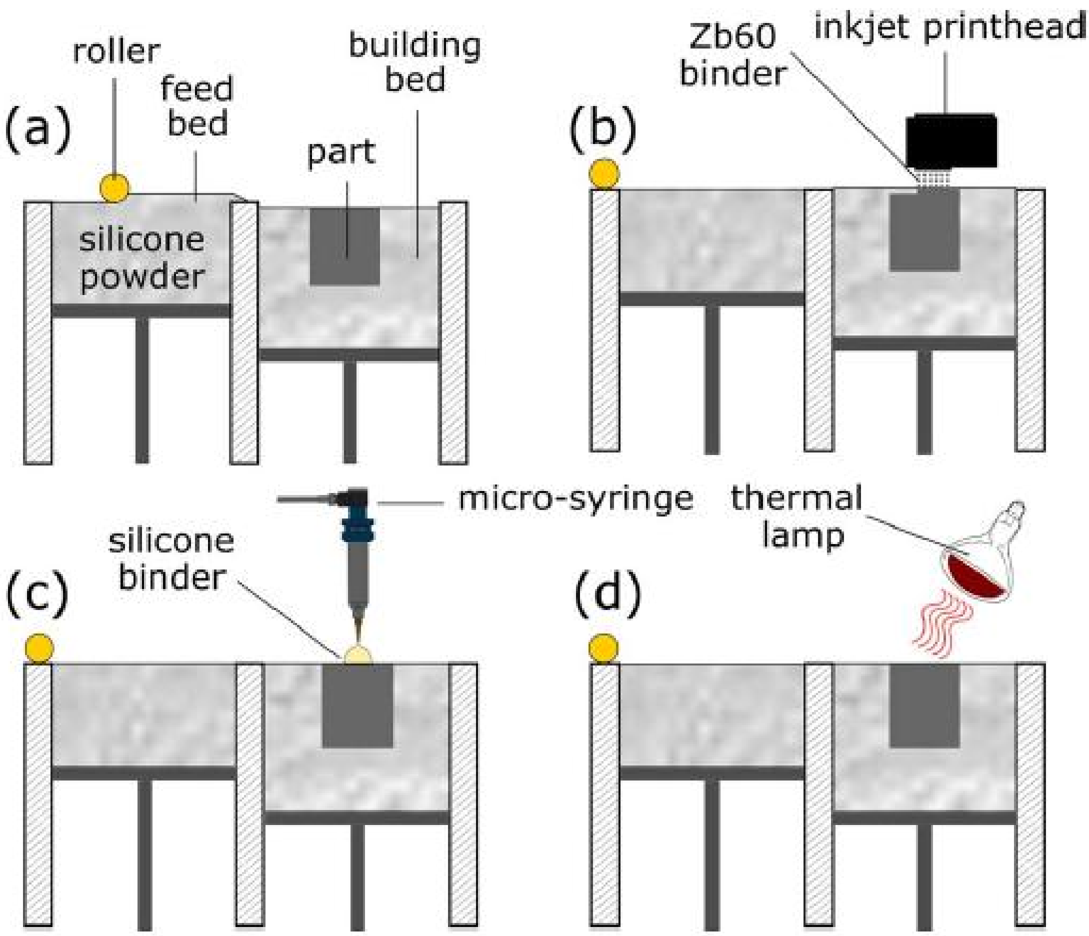

Figure 3.3. *The fabrication steps: (a) spreading the silicone powder; (b) spreading the liquid binder; (c) dispensing a silicone binder droplet to fill the porous media; (d) partial curing. [23]*

The layer thickness of the produced parts can be 25 µm. As figure 3.4 shows, the viscosity of the silicone binder is independent from the shear rate and it follows a Newtonian behavior keeping a constant value of 78 mPas. The measurements are performed at 25 °C increasing (ascendant curve) and decreasing (descendant curve) the shear rate value.

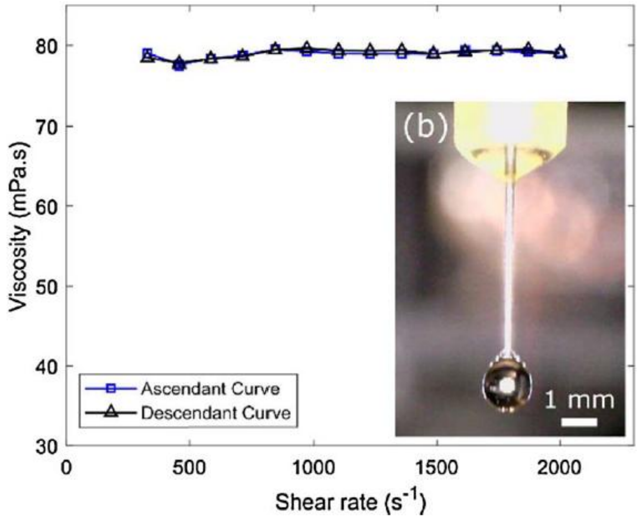

Figure 3.4. *The viscosity of silicone binder showing a Newtonian behaviour at the shear rate range of 200–2000 s^{-1} [23]*

In the experiment two hybrid organopolysiloxane powders for printing micro-structures were used: the first one consists of silicone rubbers and silicone resin (powder A), the second one only of silicone rubbers (powder B). They show high thermal stability, weatherability and biocompatibility.

The SEM images show the spherical morphology of the powders. In nature, powder A has got surface flakes because of the resin coating, while powder B is smooth because it is without the resin coating. The particles of the first powder are segregated with a particle size around 30 μm for powder A and around 13 μm for powder B.

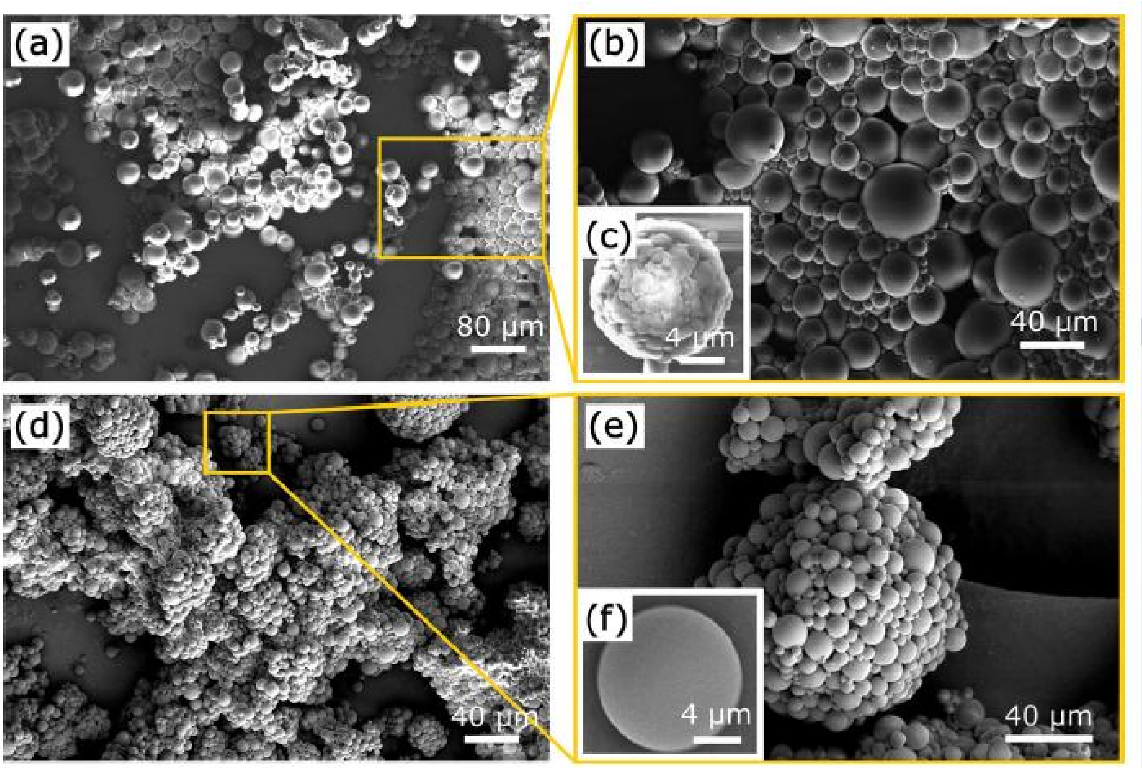

Figure 3.5. *SEM images for powder A (a– c); SEM images for powder B (d– f) [23]*

The energy required to establish a pre-defined flow pattern by the rotational and vertical movement of a blade is shown in figure 3.6.

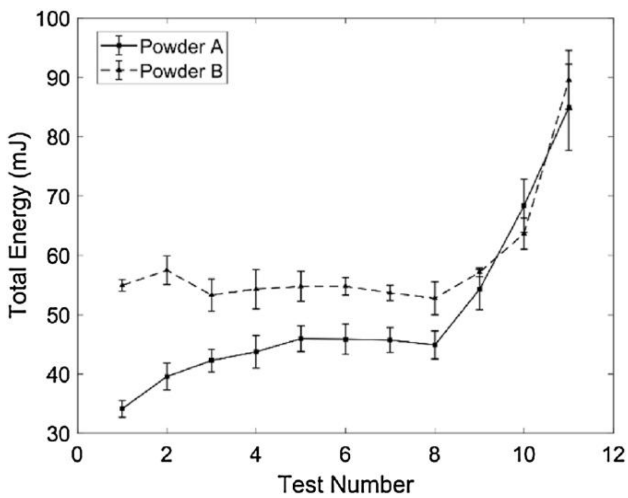

Figure 3.6. *Flow test for powders A and B [23]*

This test is performed to understand the rheological properties of the silicon powders. The first eight tests were performed at constant velocity and from the ninth to the twelfth test the velocity has been gradually decreased. Powder A is non-cohesive with a better flow behaviour requiring lower energy at the fixed velocity region in relation to powder B.

Conditioning the powders with an air flow with various velocities, the energy decreases more drastically for powder A, almost reaching the zero plateau. This confirms the optimal non-cohesive behavior of powder A that reaches a considerable fluidization level.

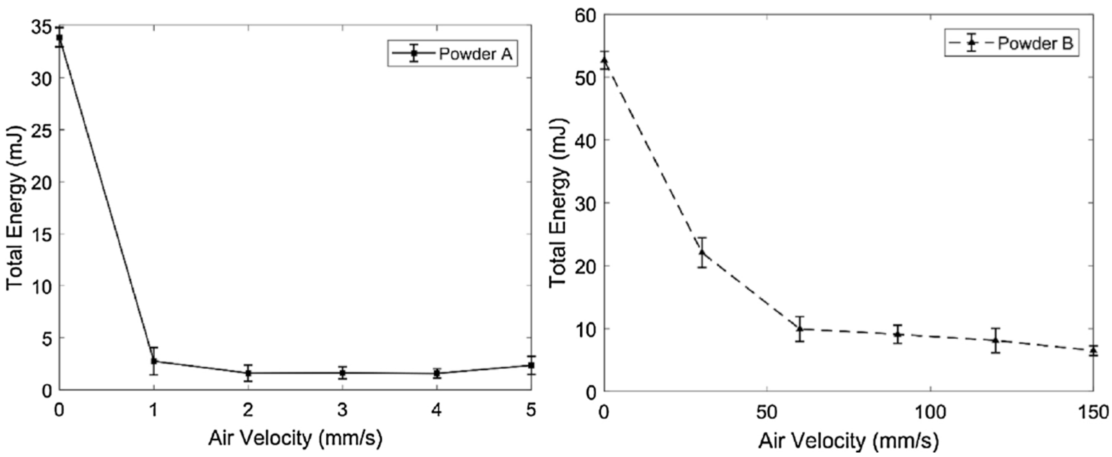

Figure 3.7. *Aeration test for powder A and B [23]*

Another test consists in compressing the sample under precise normal stress values: powder A is from 4 to 6 times less compressible than powder B, because it is non-cohesive and hence it possesses a more efficient packing of particles.

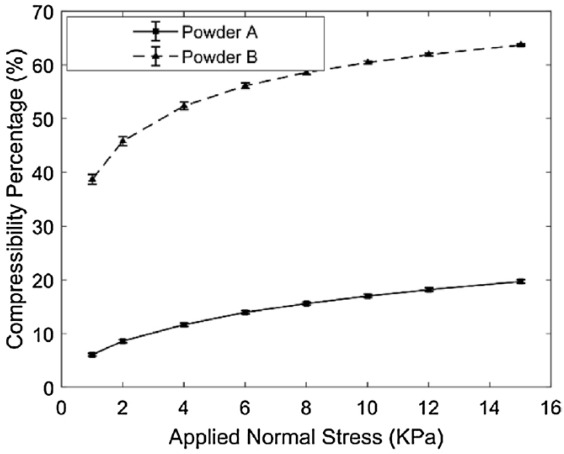

Figure 3.8. *Compressibility results for powders A and B [23]*

The permeability was also investigated. The test measures the pressure drop needed at the two extremities of the sample in order to maintain the air flowing through the sample itself constant as the normal stress increases: powder A requires 10 mbar more because it is more permeable to air.

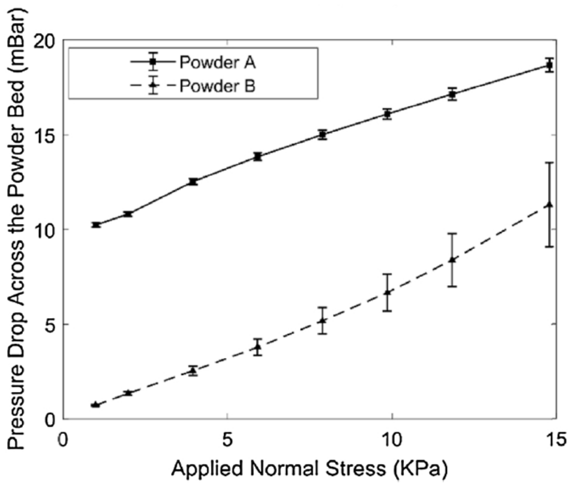

Figure 3.9. *Permeation results for powders A and B [23]*

The shear strength was measured with precise values of normal stress. Powder A shows lower values because of easier flow due to the non-cohesive behavior and more regular shape of particles.

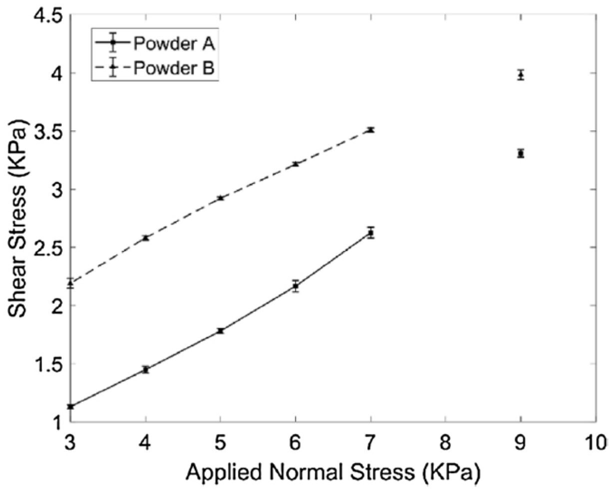

Figure 3.10. *Shearing test for powders A and B [23]*

In conclusion, contrariwise to powder B, powder A was considered suitable for printing complex micro structures with the hybrid PBBJ technology. The works shows useful tests that can be performed on polymers in order to choose the most appropriate powder for the application, when different materials are candidate for the production.

3.3. VP

In order to investigate the feasibility and the accuracy of the vat polymerization method at micro scale, Davoudinejad et al. (2018) [25] designed two test parts: one part for the box geometry and the other part for the cylinder geometry. Experimental parameters are reported in table 3.1.

Table 3.1. *Experimental conditions [25]*

Parameter/unit	**Selected value**
Layer thickness [µm]	25
Light intensity [mW]	1.75
Photopolymer resin	FTD red resin
Printing time [s]	30
Printing resin temperature [°C]	23

After printing process, the part, still covered by the liquid resin, is removed from the build plate and then cleaned with isopropyl alcohol (IPA). Pressurized air dries the product and the curing process of the photopolymer terminates in a light oven with a 300 W/m^2 UV light flux for 80 minutes.

In every test part the characteristic dimension of the features decreases from left to right (from 1.5 mm to 6 µm). The height of the features is kept constant at 500 µm. To investigate the repeatability, each test part is designed with six repetitions of the same feature. To investigate the reproducibility, test parts are printed five different times in five different days, thus getting five baths.

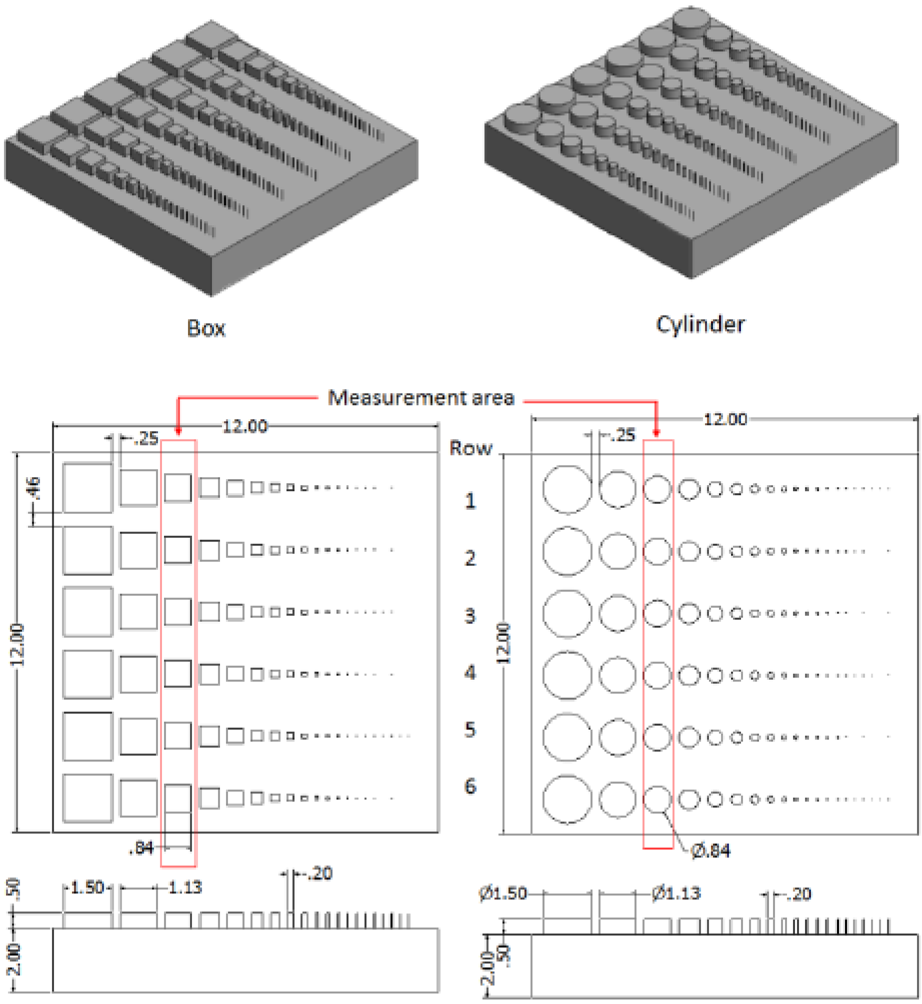

Figure 3.11. *Drawing of the test part box and cylinder [25]*

The aim of the work is to analyze if the features are built with the nominal height. In this way the procedure for the measurement is the same for both test parts. The machine is able to print the features, regardless of the geometry, until the characteristic dimension of 84 µm (11th column of the test parts). However, the box shapes with a characteristic dimension of 266 µm (7th column) or lower, change to a cylindrical shape because of the difficulty in printing the edges at that level of micro scale.

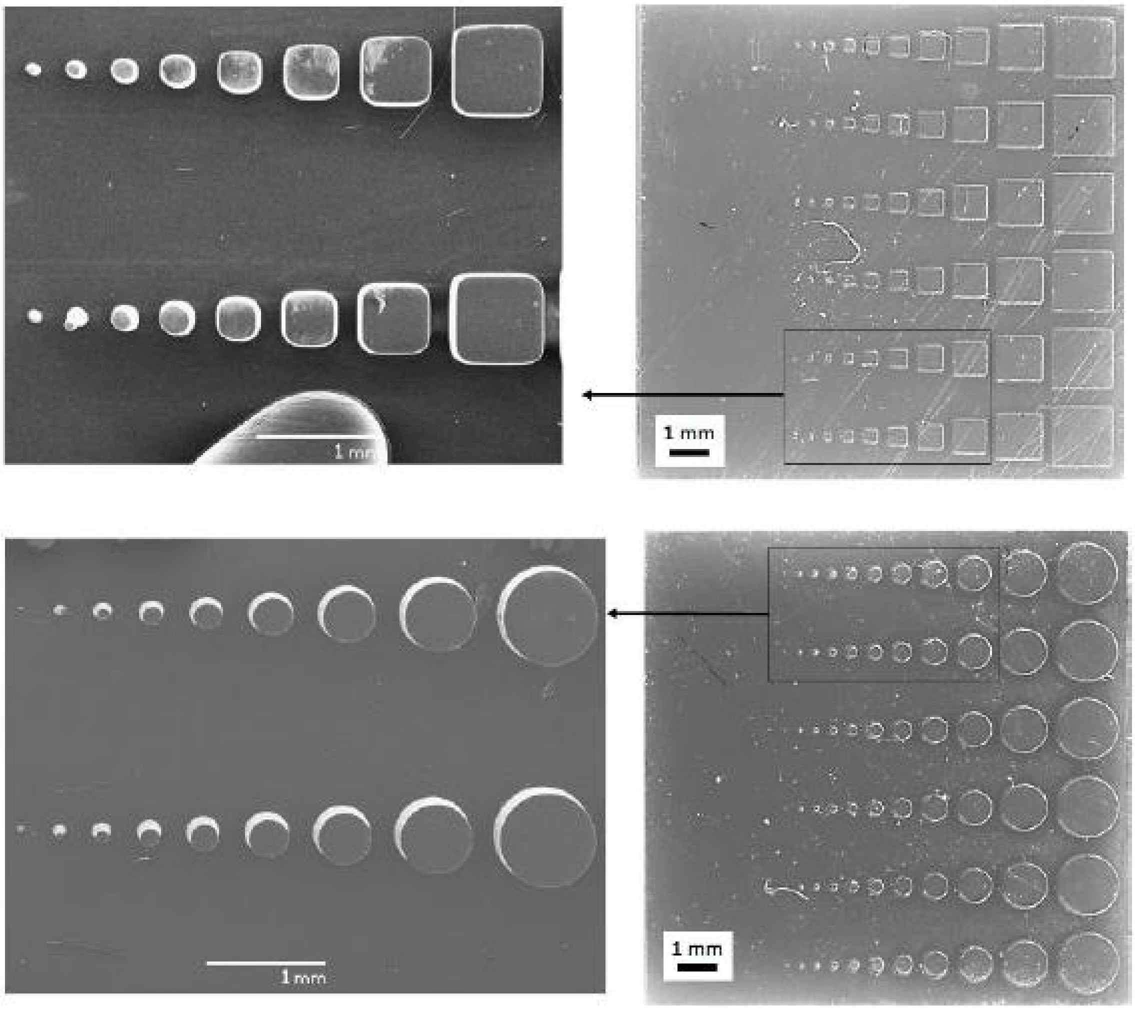

Figure 3.12. *Images of the printed features [25]*

Vat polymerization includes three steps: additive manufacture, cleaning and curing to avoid the possibility uncured resin remains on the part. The optical measurements are performed only to the third columns after the third stage, in order to give real images of the parts.

The average height of the boxes considering all the five baths is 396 μm and the one of the cylinders is 437 μm instead of 500 μm with uncertainty levels of 27 μm and 18 μm respectively.

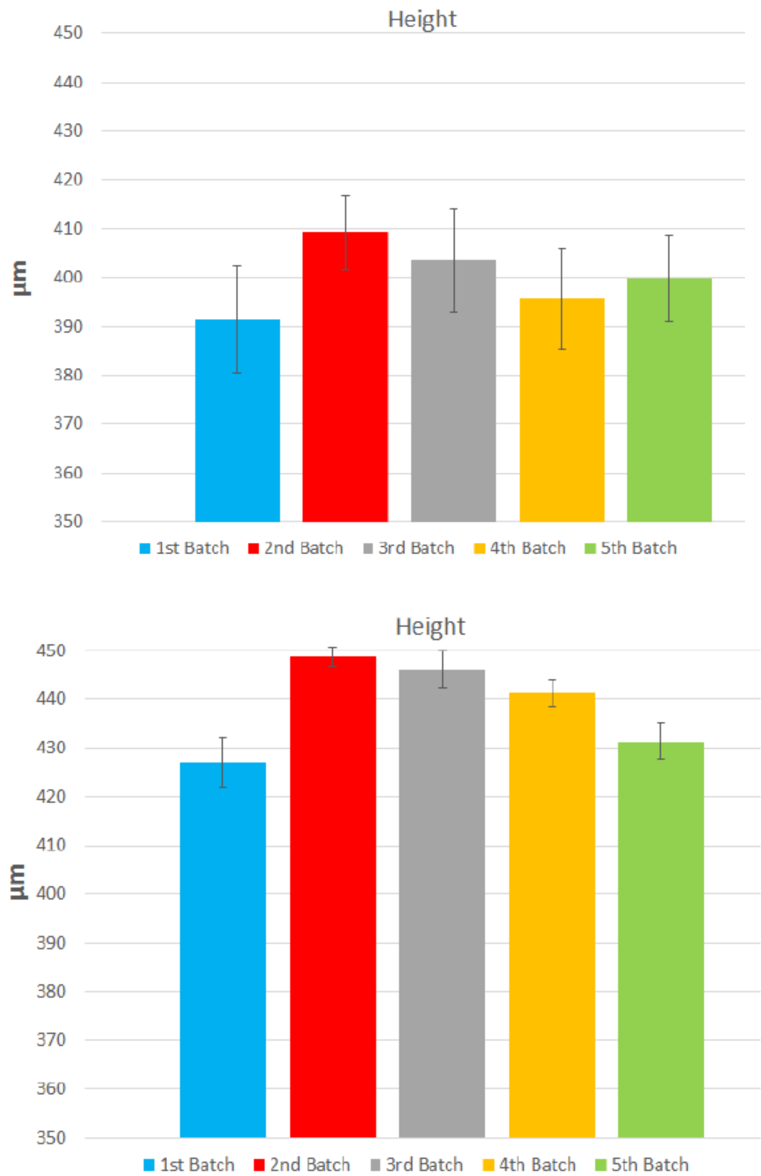

Figure 3.13. *Height measurement [25]*

The printing procedure is responsible for the variation in the height from the nominal value, but it is still considered suitable for some applications in micro field manufacturing where high accuracy is not required. This work underlines that printing accuracy can vary according to the printed geometry.

3.4. SLA

A development in the list of the available materials for polymeric additive manufacturing has been carried out in the last years. Chen et al. (2017) [26] studied a new polymer piezoelectric photocurable resin (V-Ink) containing 35 wt% of polyvinylidene fluoride (PVDF) particle and suitable for biomedical application.

PVDF is appreciated in many application fields because it is a stable material with a high piezoelectric coefficient, high mechanical flexibility, biocompatibility and excellent processability, but the main problem of this material is the difficulty of integrating it in a piezoelectric photocurable ink. In fact, in the stereolithography process, the matrix should allow to print the piezoelectric material, that could not be natively photopolymerizable. Piezoelectricity is also present in piezoceramics, but this type of material is brittle and hence usually not suitable for flexible applications. The solution proposed by Chen seems to be the most interesting in micro stereolithography for applications where deformation of the part can generate voltage or vice versa and it overcomes the problem connected to the printability via stereolithography of PVDF.

Technologies eligible for printing polymers with piezoelectric properties are fusion deposition modeling and ultrasonic additive manufacturing methods, but, in order to study the new resin, Chen chose the projection micro stereolithography (PμSL) that creates each layer in a single exposure via a dynamic mask and a patterned ultraviolet light hits the surface of the resin curing it. With this method, the resolution is 7 μm and layers measuring 20 μm in thickness are printed showing a piezoelectric voltage coefficient comparable with the one of pure PVDF.

V-Ink is composed of PVDF (piezoelectric material), a monomer called HDDA (matrix material) and 22.68 wt% diethyl fumarate (solvent to regulate the viscosity); there are also small percentages of photoinitiator and UV absorber. A heater can be used to decrease the viscosity of the resin allowing a higher weight percentage of PVDF in the material.

The main requirements to make the process optimized are:

- PVDF particles should be uniformly dispersed in the matrix;
- Viscosity should be kept under control and constant;
- Piezoelectric properties should be evaluated experimentally only after V-Ink is declared printable with those particular process parameters and material composition.

PVDF particles need some minutes to reach an acceptable level of dispersion in the V-ink. In the figure, 15 wt% PVDF is taken as an example in order to understand how many minutes could be necessary for the dispersion process. An optimal dispersion occurs within 30 minutes. After the first hour precipitation becomes considerable and until the forty-eighth hour the condition remains stable as it can be seen from the colour difference in respect to the “w/o PVDF” figure, where the HDDA resin is without PVDF.

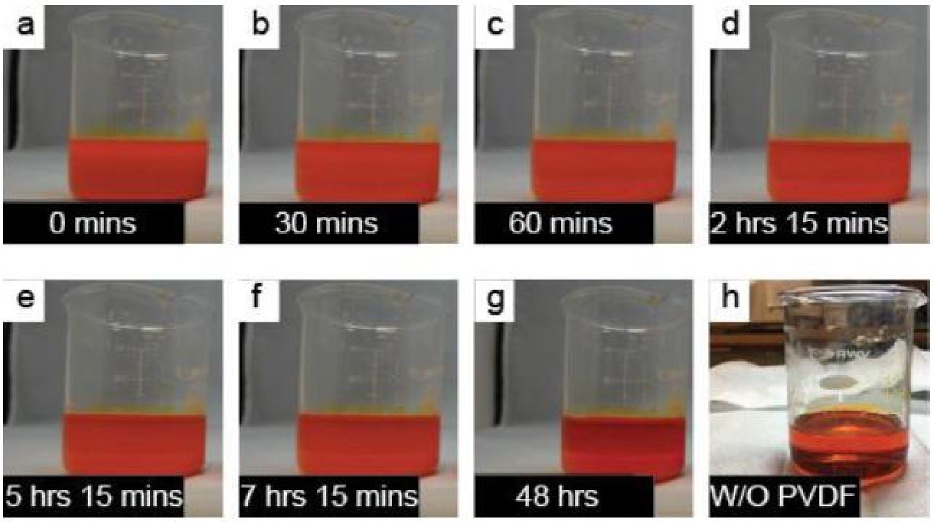

Figure 3.14. *Time-lapse images of PVDF particles dispersed in V-Ink [26]*

The viscosity was measured through a rheometer: the results show that it increases as PVDF concentration increases. 35 wt% PVDF is the maximum limit for a controllable recoating step; in fact, higher values increase more dramatically the viscosity, thus making the dimensional accuracy and the surface quality unacceptable for micro field applications.

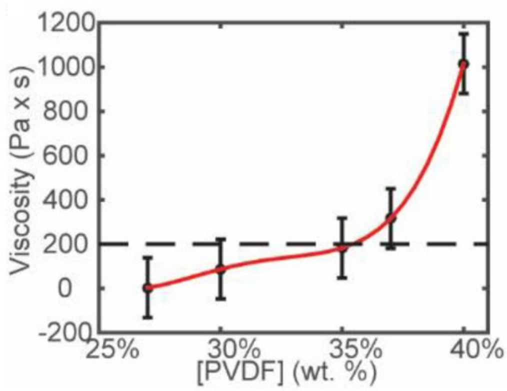

Figure 3.15. *Complex viscosity for V-Ink with various concentration of PVDF [26]*

Some tests are performed to evaluate the influence of PVDF concentration and of the poling electric field in the piezoelectric voltage coefficient for micro field applications. Defining the z-direction as the direction of the moving platform sustaining the part, the piezoelectric voltage coefficient, identified as g_{33}, is equal to the induced electric field in the z-direction per unit stress applied along the same direction:

$$g_{33} = \frac{VA}{Ft} = \frac{V}{pt} \tag{3.1}$$

Where t is the thickness (usually it is 0.5 μm, but it can be reduced) and A stays for the area of the PVDF layer perpendicular to the z-direction.

Increasing PVDF concentration and keeping constant all the other parameters, the piezoelectric properties of the material are enhanced as shown in the graph in figure 3.16.

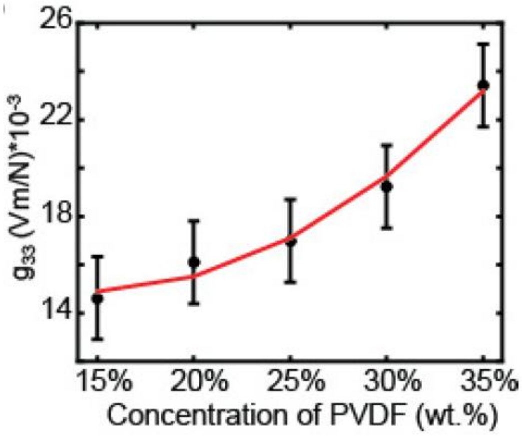

Figure 3.16. *Calculated g33 coefficient for 3D printed PVDF sensors versus concentration of PVDF [26]*

However, it is necessary to remember the limit of 35 wt% PVDF for a suitable value in viscosity. Decreasing the thickness of the layer there is a subsequent increasing in the poling electric field and, if all the other parameters are kept constant, the piezoelectric voltage coefficient increases dramatically, showing that the piezoelectric properties of the material are enhanced if the dimensions of the part are reduced.

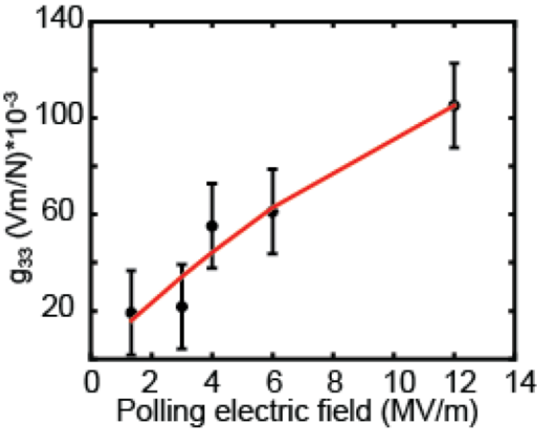

Figure 3.17. *Calculated g33 coefficient for 3D printed PVDF sensors versus poling electric field [26]*

This work underlines the importance of preparing the correct base material in order to get the desired characteristics for the final micro component.

3.5. FDM AND EPAM

Some semi-crystalline polymers, such as odd nylons, PVDF and its copolymers, can be made piezoelectric, as clarified by Tarbutton et al. (2017) [27]. Piezoelectric PVDF transducers are appreciated for vibration, force and acceleration sensors. PVDF has ferroelectric properties (it is locally piezoelectric and pyroelectric). It has got five crystalline phases: $\alpha, \beta, \gamma, \delta$, and ε. If β and δ phases are aligned, the bulk polymer specimen has got a global ferroelectric behaviour. β phase can be easily produced by mechanical stretching, electrospinning, application of high electric field, quenching the melt sample at high pressure or crystallization from solution.

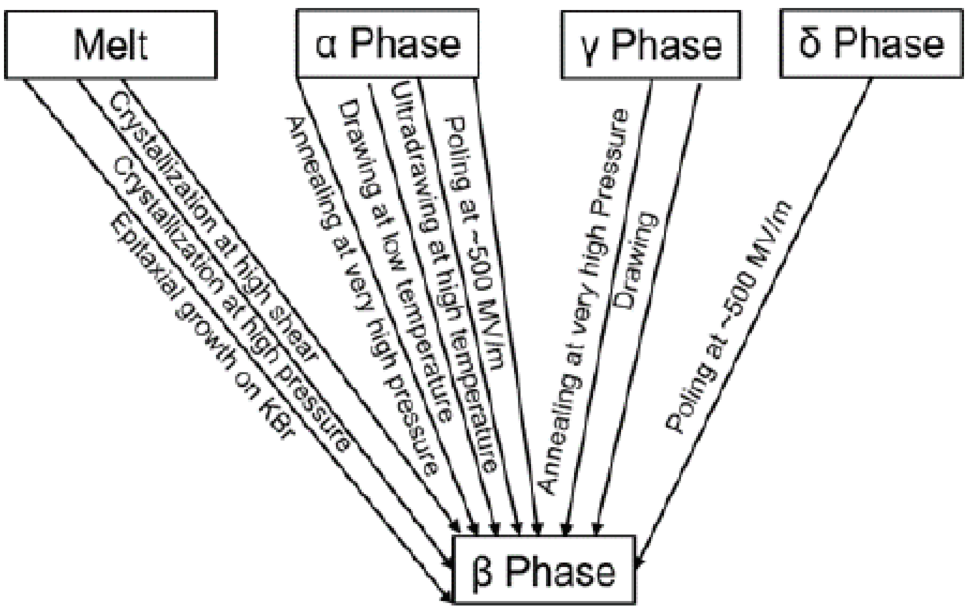

Figure 3.18. *Scheme of reproduction of the piezoelectric β phase in PVDF through different methods [27]*

During FDM several processes align the piezoelectric phases of a filament of PVDF polymer with a predominant α phase. During printing, the α phase of the PVDF is strongly altered, while the dominant electroactive phase in the polymer (β phase) has not got important changes.

The aligning processes are:

- extrusion which applies high shear tension to the filament;
- pressure increasing by the nozzle inside the melted material after its passage through a heater (crystallization from melt under high shear);
- quenching performed by the environmental air, as well as the build plate, because of their lower temperatures (annealing at high pressure);
- motion of the nozzle that polishes the surface of the filament.

The contribution to the phases alignment coming from each of these processes is unknown.

EPAM is just a FDM technology with an added electric field between nozzle and build plate to enhance the alignment of any piezoelectric phase. Using EPAM, micro energy harvesting devices, actuators and sensors can be produced.

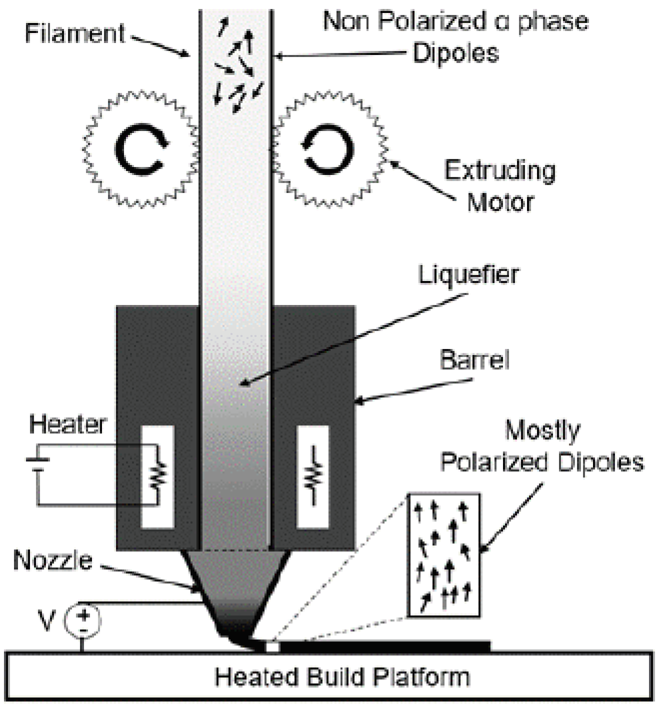

Figure 3.19. *Modified FDM 3D printer aligns β phase with a strong electric field [27]*

To study the effect of the added electric field over the phase transformation, two filaments have been analysed. One is obtained by FDM and the other by EPAM (applying a voltage equal to about 30 MV/m). The results show that electric field can increase the amount of β phase by 35%. The other remaining phases are α and/or δ. By increasing the electric field, it is reasonable to think that a greater amount of α phase could be transformed into β phase.

This work underlines the importance of integrating and developing existing technologies in order to get the desired characteristics of the material, such as a particular microstructure, because production steps influence strongly the properties of the final product.

4. CERAMICS

4.1. GENERALITIES

Ceramics in additive manufacturing find a discrete range of possible technologies, although it remains the type of material less studied in literature, probably because of the more restricted number of possible applications.

4.2. SLM AND SLS

Two of the most studied materials in the ceramic micro additive manufacturing field are Al_2O_3 and the composite Al_2O_3-ZrO_2 [28]. To avoid the creation of cracks after production by SLM, it is necessary a preheating process for the ceramic with a temperature of at least 1600 °C.

For the ceramics, the two most important parameters in SLM and SLS in order to control the flowability are the size and the shape of the particles. Large particles with irregular shape are almost impossible to process with a micro manufacturing technology. The micro size particles are needed in micro field, thus giving to the produced part a better surface quality. However, fine powders have the risk of agglomeration because of van der Waals forces. In literature, it is already known that powders with a diameter smaller than 5 μm tend to agglomerate, while powders with diameters bigger than 5 μm tend to make the process too difficult because of the higher density. It is also important that the powder is homogeneous in dimension of the particles, thus giving the final parts a homogeneous behavior under thermal and mechanical stress.

4.3. VP

Vat polymerization is also used for producing ceramic parts at the micro scale starting from polymers [29]. This method presents the main advantage of eliminating the stress introduced during the additive manufacturing process, that creates the product layer by layer. Ceramic particles with a diameter of 1 μm are dispersed in a photopolymeric resin with a percentage of 50-60% in volume constituting a very viscous slurry. The green part is printed with repetitive steps: irradiating with UV light the slurry to build a layer and then lowering the base platform. A heat post treatment, the so called debinding process, evaporates the polymeric fraction and another heat post treatment, the so called sintering process, creates the monolithic ceramic part. High quality green parts require a dense powder with a homogeneous microstructure.

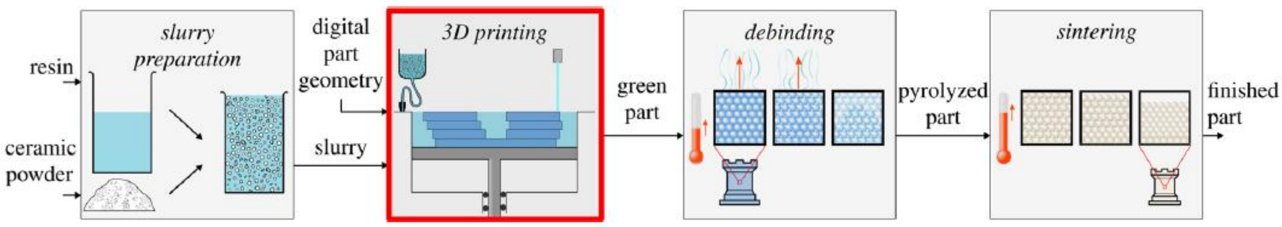

***Figure 4.1**. Overview of the ceramic additive manufacturing process by vat photopolymerization [29]*

Injection molding is another AM method able to convert polymeric material into ceramic material, but this technique has still to be studied in detail for micro scale applications.

4.4. μSLA

A promising technology for ceramic micro components is micro stereolithography (μSLA), that is able to create parts with complex geometries and high precision. The four principal factors influencing the quality of the part produced by μSLA have been studied in literature [30] and they are:

- resin type;
- layer height;
- orientation of the part;
- cleaning operations.

Resolution, around 30 μm, is given by the manufacturer and it is not influenced by the resin, which gives the desired properties to the product. Cleaning operations can include treatment with isopropyl alcohol, compressed air and the post-curing process to enhance the properties of the resin. Orientation of the product must be considered, because accuracy decreases when there is a hole or a protruding part in a surface that has got an inclination bigger than 30° from the horizontal plane and the part could be not printable at the micro scale. This difficulty testifies the inability in printing curved micro-scaled surfaces with this technique. The surface roughness, defined as the average of the absolute values of deviations of the profile from the midline, is lower if the surface is less inclined.

Al2O3 ceramic micro components with 99.5% density and good homogeneous microstructure have already been fabricated via μSLA process and subsequent sintering [32].

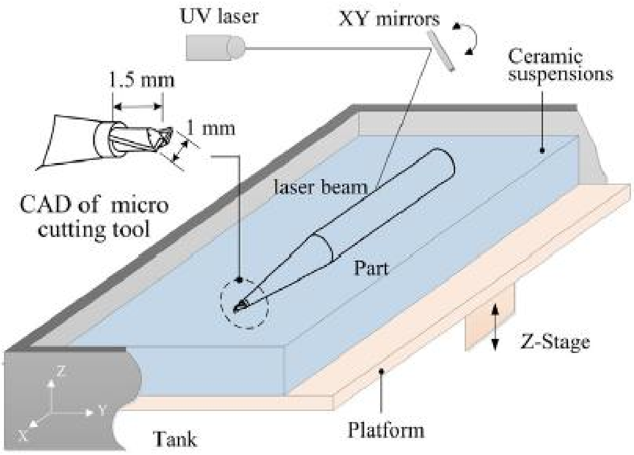

Figure 4.2. *Scheme of μSLA [32]*

Photosensitive resins with Al_2O_3 particles have been deeply studied and they are prepared into UV-curable suspensions. Ceramic suspensions are solidified through the use of a UV-laser and result anchored in the polymer network. Debinding and sintering are the next steps. The viscosity of the suspension should not overcome the value of 5 Pas at 30 s^{-1} shear rate to avoid a deterioration in the layer recoating performance. The ceramic suspension should contain at least 40% in volume fraction of solid loading to avoid problems in debinding and sintering process. The curing depth of ceramic suspension must be higher than the set layer thickness.

While hydroxyl groups on Al_2O_3 are hydrophilic, resin monomers are frequently hydrophobic: it is necessary to convert Al_2O_3 particles to make them hydrophobic modifying their surface properties with the adding of silane coupling agents KH550, KH560 and the stearic acid (SA), because the incompatibility between hydrophilic powders and hydrophobic premixed resins would cause the agglomeration and sediment of particles in the liquid.

4.5. MIP-SL

Chen et al. (2016) [31] demonstrated that a piezoelectric composite slurry with $BaTiO_3$ nanoparticles (100 nm) can be 3D printed using Mask-Image-Projection-based Stereolithography (MIP-SL) technology applied for microscale.

In SLA, viscosity of the material must have a limit in order to preserve a good processability, but this limits the density of the material and hence it drives to poor piezoelectric properties. To solve this problem, a solution could be the use of nanoparticles that increase the solid load of the material, giving birth to the problem of the decreasing in the cure depth, defined by Jacob’s equation as:

$$C_d = D_p ln \frac{E}{E_c} \tag{4.1}$$

Where E is the energy density of incident light, E_c is the critical energy density and D_p is the resin sensitivity defined as:

$$D_p = \frac{2 d_{50} n_0^2}{3 \tilde{Q} \Delta n^2} \tag{4.2}$$

Where d_{50} is the average particle size, Δn is the refractive index difference between the ceramic particle (n_p) and the liquid resin (n_0). When d_{50} decreases to the nanoscale, D_p and C_d decrease, making the process almost impossible because layers need to be over-cured to attach to the previous cured layers.

The X-Y resolution of the machine used for the experiments is 20 μm and the Z resolution is 10 μm. A really common piezoelectric material is PZT. However, it contains lead that is toxic for biomedical applications and hence is not used commonly. Barium titanate ($BaTiO_3$) can be an alternative material and it is studied in this work as base material for an ultrasonic transducer.

The $BaTiO_3$ powder needs a pre-treatment: a planetary mill with stainless steel balls is used for the de-agglomeration of the powder. Then the mixture is dried to allow the evaporation of the solvent.

Ball milling is used to mix 70% of $BaTiO_3$ powder with 30% of photocurable resin.

In order to create dense piezoelectric ceramics, post-treatments are needed: organic binder removal to avoid deformation of the samples and high temperature sintering to make $BaTiO_3$ particles interconnected each other. The first one is performed in a furnace filled with argon, for 3 hours at a temperature of 600 °C; the second one in a furnace with air at 1330 °C for 4-6 hours. Sintering leads to grain size growth, that remains in the nanoscale, porosity reduction and shrinkage.

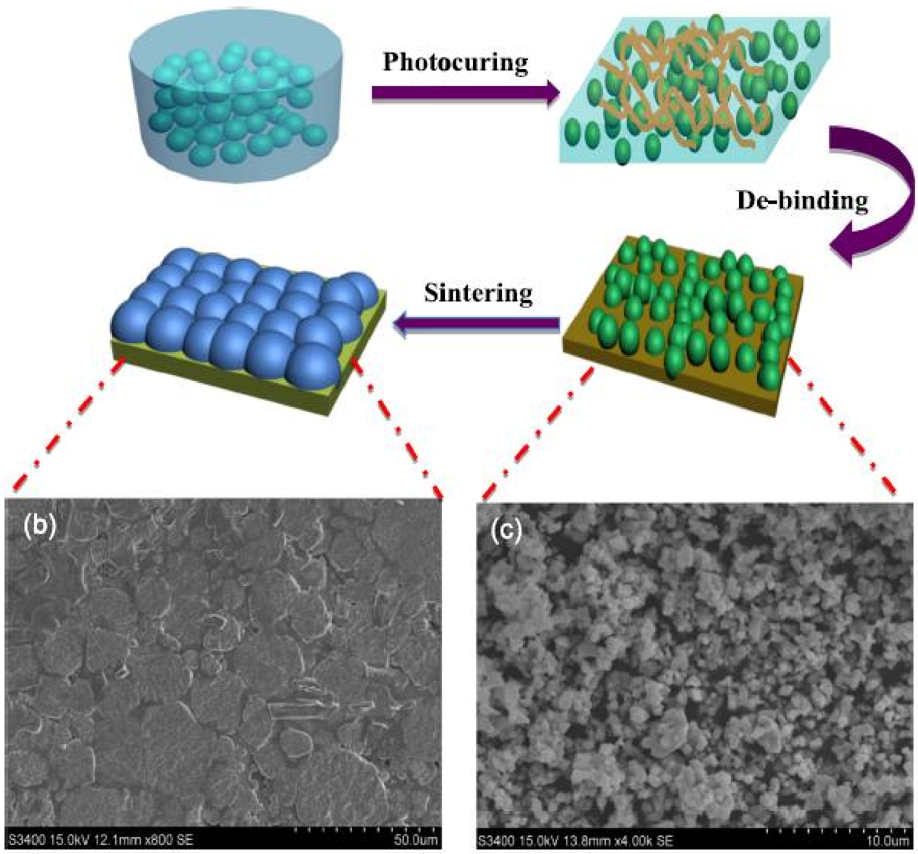

Figure 4.3. *Green part fabrication and post processes scheme with SEM magnification images [31]*

Experiments are performed in order to evaluate the characteristics of the micro-sized components. As the table below shows, there is a deep similarity between the classical fabrication method and MIP-SL. Density is a bit lower than the one of the bulk material and the energy loss is low.

Table 4.1. *Results from different fabrication methods [31]*

Fabrication method	**Density [g/cm³]**	**ε (1 kHz)**	d_{33} **[pC/N]**	**tan δ (1 kHz)**
Typical	6.02	1700	190	<0.1
MIP-SL	5.64	1350	160	0.012
Laser sintering	5.59	-	-	-
Binder jetting	3.93	640	74.1	0.03
Injection molding	5.86	-	-	-

The good symmetric ferro-electric hysteresis loop is shown in figure 4.4.

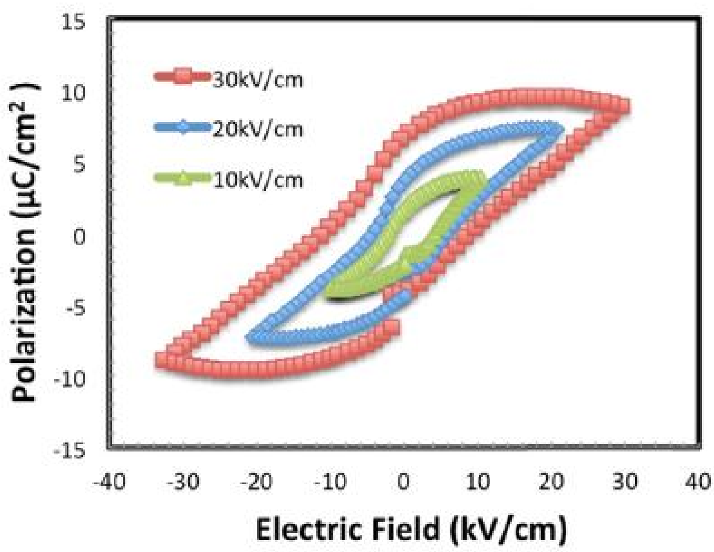

Figure 4.4. *Polarization–electric field hysteresis loops [31]*

After heat-treatment, $BaTiO_3$ keeps perovskite structure and with these parameters it is suitable for piezoelectric applications, because 3D printed piezoelectric preserve the ability to convert electric charge to deformation and vice versa. This work wants to underline the possibility of reaching high performance components with additive manufacturing technologies applied at the micro scale.

4.6. DOD

One of the most used additive manufacturing method at the micro scale for ceramics is inkjet printing. It has got some advantages on the other technologies: low cost, fast production and successful commercialization [33, 34].

In direct inkjet printing, the ceramic powder is ejected as drops suspended in a liquid slurry. When the drops solidify, the ceramic green body is produced. Direct inkjet printing is more versatile than powder bed printing, because it is suitable for the deposition of more materials in parallel. The ink can be a particulate suspension or a solution. The two main limitations of this technique are:

- the printed part may require post-treatment in order to show adequate microstructure and material composition;
- the ink must be printable.

Inkjet printing can be classified into three different groups:

- Continuous inkjet printing (CIJ);
- Drop on demand inkjet printing (DOD);
- Electrostatic inkjet printing (EIJ).

In CIJ, drop diameter is larger than 50 µm, it is a rapid method, but it lacks high accuracy. Its main problems are that the continuous flow brings to ink wastage when a recycling system is not expected and the ink should be inductively chargeable. In DOD, drop diameter can be 1 µm, waste is more controlled being the drops generated only when required, but it is a less fast method in respect to CIJ and it has got a worse surface finish. It can have a thermal or a piezoelectric actuation. In EIJ the working principle is different from the other two groups: the liquid surface is charged and an electrostatic repulsion generates the drops, that have got a smaller diameter and a greater precision and resolution. However, the most used method among these three remains piezoelectric DOD.

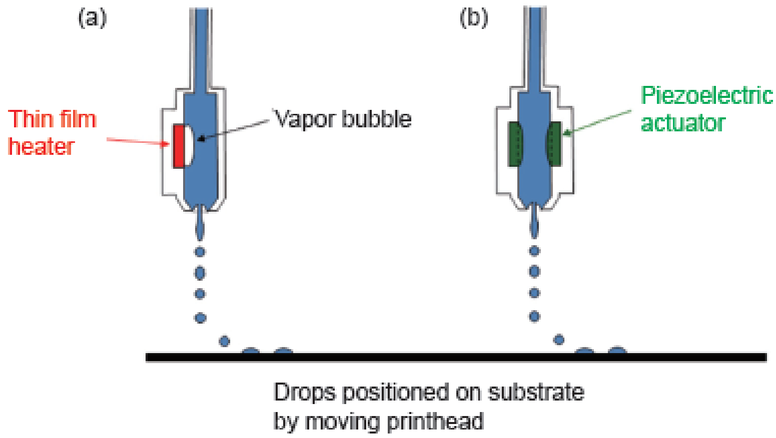

Figure 4.5. *Schematic reproduction of DOD with thermal (a) and piezoelectric (b) actuation [33]*

The ink must be a ceramic suspension showing a low degree of segregation and agglomeration of the particles. Compatibility between ink and substrate or previously deposited layers is needed to allow a perfect solidification by evaporation creating a suitable structure for post-processing. Inkjet drop formation can be optimized studying the parameter Z defined as the reciprocal of the Ohnesorge number:

$$Z = \frac{1}{Oh} = \frac{(\gamma \rho a)^{1/2}}{\eta} = \frac{Re}{\sqrt{We}} \tag{4.3}$$

Where γ is the surface tension of the fluid, ρ is its density, η is its dynamic viscosity and a is a characteristic length (diameter of printing nozzle).

Z is inversely proportional to viscosity. For an optimal drop ejection, a minimum Z is required, while for an optimal drop formation a maximum Z is required, remembering that drop formation is stable only in the range 1<Z<10: a compromise is needed. Drop ejection requires a minimum velocity, that can be expressed according to We number:

$$We_{min} = v_{min}\left(\frac{\rho a}{\gamma}\right)^{1/2} = 4 \tag{4.4}$$

Where v_{min} is the minimum velocity of the ejected drop.

In addition, a too much high drop velocity can cause the phenomenon of splashing when a drop touches a surface. Stow and Hadfield defined this splashing threshold with the formulation:

$$We^{1/2}Re^{1/4} = f(R) \tag{4.5}$$

Where $f(R)$ is a function of surface roughness.

According to all these equations, assuming the behavior of the fluid to be Newtonian, a printable region is highlighted in figure 4.6.

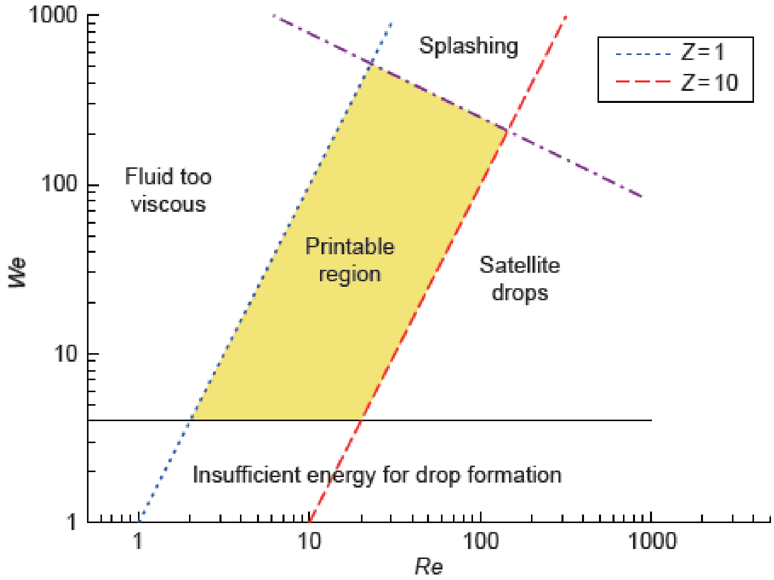

Figure 4.6. *Representation of a parameter space with axes of the Reynolds and Weber numbers, showing the region of fluid properties where inkjet drop formation is optimized [33]*

If the fluid is non-Newtonian, there is a lower probability that the tail of ink behind the main drop falling from the nozzle is destabilized into smaller satellite droplets.

The splashing threshold can be written by the equation:

$$K_c = We^{1/2}Re^{1/4} = \frac{Re^{5/4}}{Z} = 50 \tag{4.6}$$

Following the boundary condition 1<Z<10, for a value Z=10, Re number turns out to be 144. Now the maximum impact velocity can be calculated:

$$v_{max} = \frac{144\eta}{a_d \rho} \tag{4.7}$$

Where a_d is the drop diameter.

The volume deposition rate follows the equation:

$$\dot{V}_{max} = \frac{1.2\pi a_d \eta}{\rho} \tag{4.8}$$

The equivalent mass deposition rate is:

$$\dot{m}_{max} = 1.2\pi a_d \eta \tag{4.9}$$

Viscosity is a key factor in printability. Its maximum acceptable value in the ink depends on the inkjet printhead design and it cannot overcome 30 mPas. Every ink drop is composed by solvent and ceramic solute: with the solidification of the drop, the solvent is totally evaporated and only the ceramic solute remains in order to form the component. The viscosity of particles increases rapidly with suspension concentration, hence in the ink the concentration of ceramic particles must be lower than 30% in volume in order not to overcome the threshold of 30 mPas. In this way, every drop is composed for at least its 70% in volume by a solvent that will not solidify, but it will evaporate. If the solvent solidifies, it must be removed through a post-treatment.

Unfortunately, usually the deposition is inhomogeneous and the first ink part to solidify leaves a ring deposit, the so called "coffee stain" or "coffee ring" defect. This is an issue for all inkjet printing techniques, especially for DOD. The coffee ring is on the border of each drop and it is a collection of solute particles, that migrate from the center to the border of the drop. This happens because above the border of the drop, when the drop touches the substrate, there is a smaller column height of ink and this leads to a faster evaporation of the solvent. In this way, the center of the drop results as pinned by the border and flow occurs toward the drying zone (i.e. the border of the drop), carrying solute nanoparticles that get deposited and accumulated. The solution is the adoption of particular solvents able to promote the Marangoni flow, that is a phenomenon driven by the gradient in surface tension between drop center and edge and it is opposite to the effect that drives the coffee ring defect. The Marangoni flow, in fact, occurs from the border of the drop to the center and it is parameterized by the Marangoni number:

$$Ma = \frac{\Delta\gamma r}{\eta D} \tag{4.10}$$

Where $\Delta\gamma$ is the surface tension gradient, r is the radius of the drop, η is the fluid dynamic viscosity and D is the diffusion coefficient. The Marangoni flow dominates, if $Ma > 100$. Ma can be increased heating the substrate in an appropriate way, because the temperature difference between drop and substrate enhances the surface tension. Additionally, the smaller the pore size of the substrate is, the more the coffee ring defect is reduced, because there is less infiltration of nanoparticles in the pores.

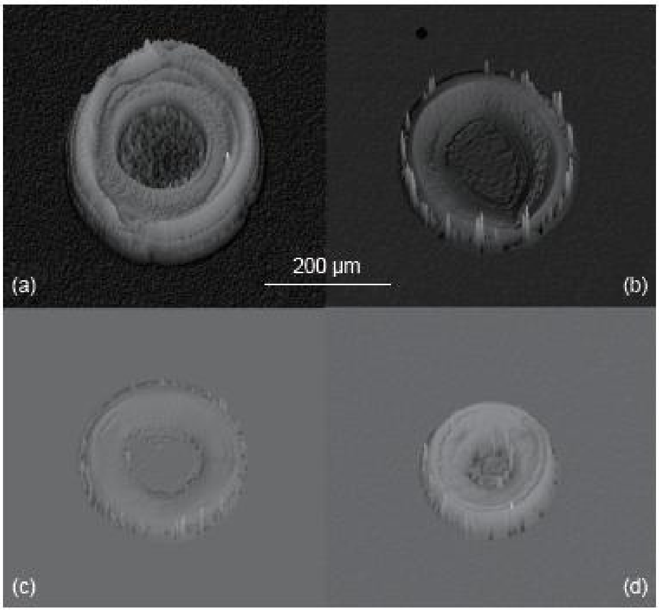

Figure 4.7. *Coffee stain in ZrO_2 inkjet printed drops on a glass support heated at 25 °C (a), 35 °C (b), 50 °C (c) and 100 °C (d) [33]*

Among the piezoelectric materials, PZT is the one with the strongest mechanical to electrical coupling and in general drop-on-demand (DOD) printing is a flexible and inexpensive method for creating thin films in PZT with complex and miniaturized geometries [35]. Ink jet printing can be studied in order to manufacture a piezoelectric micromachined transducer in PZT for promising future MEMS applications.

First of all, it is necessary to think about the correct composition of the ink: a PZT sol-gel based DOD ink with a properly studied viscosity and surface tension has been chosen, together with ink solvents that must not interfere with the hydrolysis reaction needed in order to create the gel film. To study the influence of the solvent in the balance of viscosity and surface tension, the inverse of the Ohnesorge number, commonly referred to as Z, is considered:

$$Z = \sqrt{\frac{\rho\gamma L}{\eta}} \tag{4.11}$$

Where ρ is the fluid density, γ is the fluid surface tension, L is the characteristic length scale (radius of the printer nozzle) and η is the fluid viscosity.

For the experiments, a high pressure thermal ink jet printer is used. Taking into account the size of the nozzle and the molecular weight of the solute, that is low, the maximum concentration of the ink is chosen in order to avoid a non-Newtonian behavior of the fluid, because this could avoid drop formation.

Z should be between 1 and 10 in order to remain in the jettable range and the best drop control is given by $Z = 6$. From experiments it is evident that also a high amount of solvent do not influence the sol-gel chemistry.

Drying plays a key role in the final morphology of the film. When the film evaporates, there is the birth of internal fluid flows that drive the solutes within the film determining the distribution of solute material and there is the issue of the coffee ring defect. Substrate temperature is the design parameter that is used to balance the outward and inward capillary flows to form uniform drops, lines and films. As shown by figure 4.8, best uniformity is reachable with a heating of the substrate up to 55 °C.

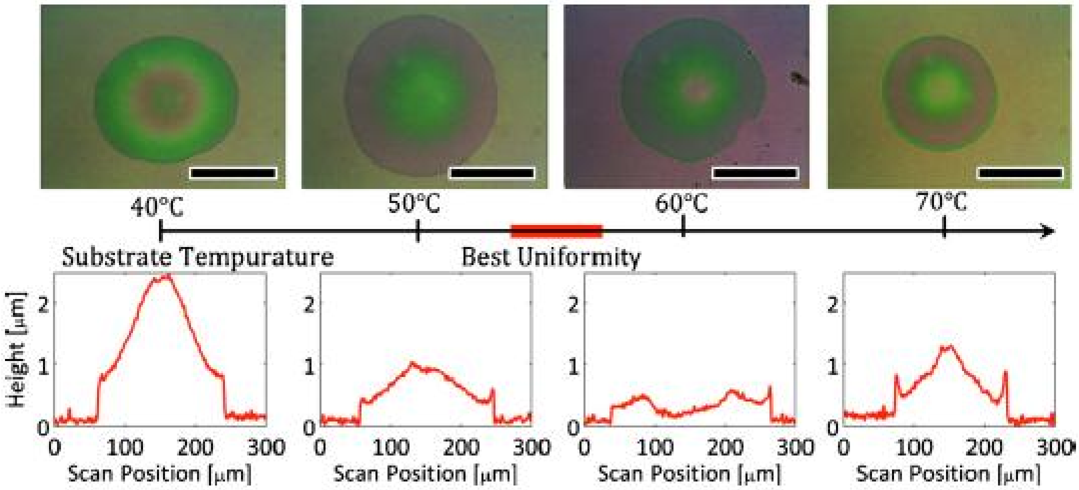

Figure 4.8. *PZT sol-gel drops printed on a PZT substrate a different temperatures. Scale bars: 100 μm [35]*

Coalescence is a key factor for creating smooth lines and films. It depends on the substrate temperature and a measurement of the shape of the profile of the dried solute is performed in order to understand the optimal temperature. The best uniformity occurs when drop deposition and drying times are similar.

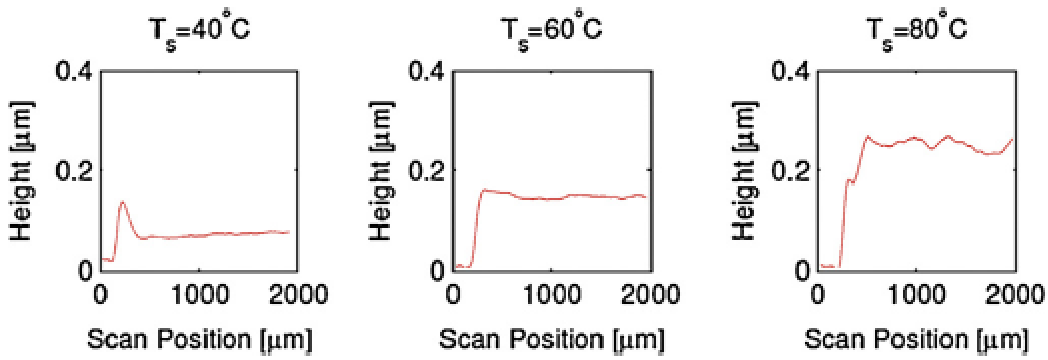

Figure 4.9. *Profile of deposited material with different support temperatures [35]*

Hence, the substrate temperature has got influence both in uniformity of the single drop and of the lines and films.

The application studied is a transducer with electrode and PZT films able to deform when an electrical field is applied. Tests show that parameters of the application are suitable for MEMS application and comparable to the ones of the other transducer manufactured with traditional technologies such as spin coating, underlining the importance in developing this technology in production for these devices.

5. METALS

5.1. GENERALITIES

Additive manufacturing for metals is widely studied because it presents many advantages as shown in figure 5.1.

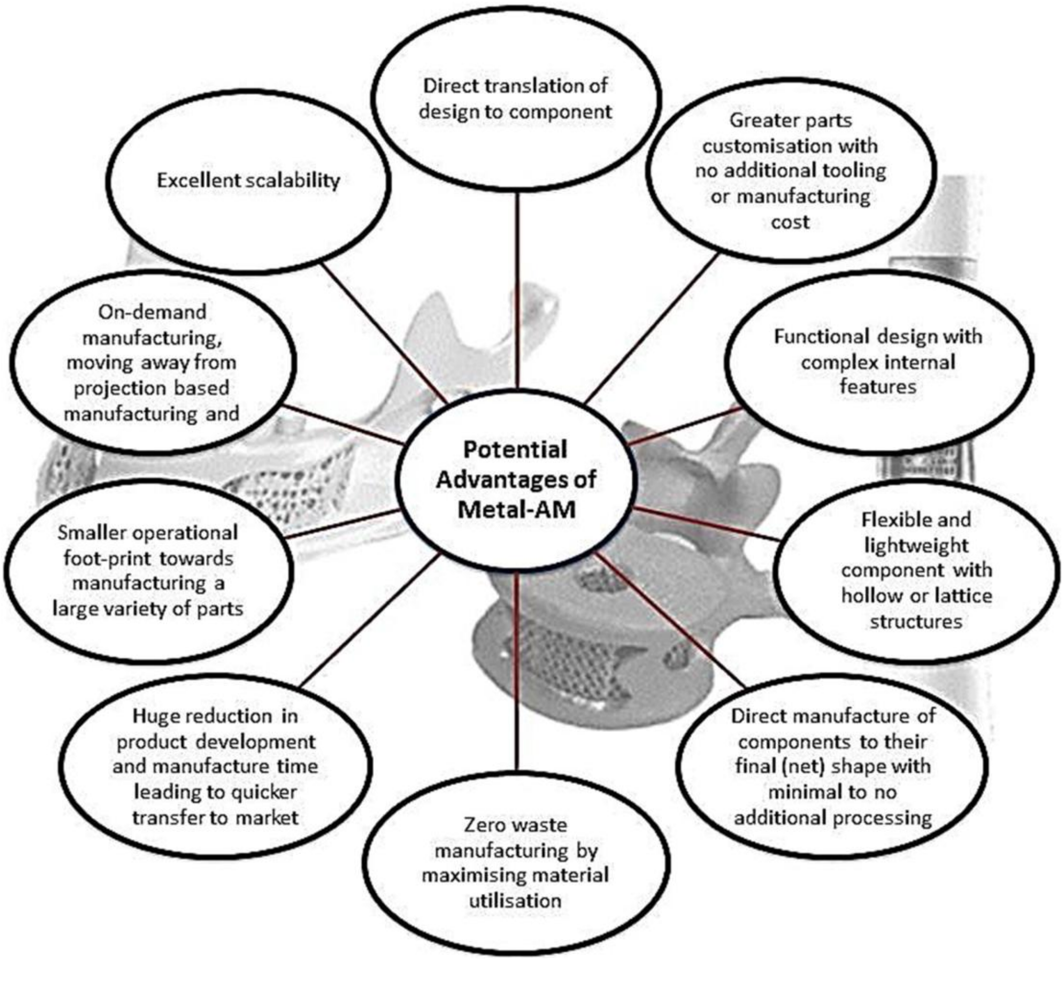

Figure 5.1. *Advantages of metal AM [2]*

Every alloy has got its preferred technology [36]. In literature, it is possible to read the main techniques adopted for each metallic material.

Al-Si, Al-Si-Mg and Al-Mg-Zr are the classical SLM alloys, but for aluminum alloys wire based AM is emerging, in fact, electron beam AM is used for Al-3Ti-Sc and Al-Cu-Mn-Mg-Ag.

Among titanium alloys, the most studied is Ti-6Al-4V because of its possible adoption in many biomedical applications. For this material two powder bed AM techniques are commonly used: the laser beam (SLM) and the electron beam (EBM) based technologies. Other laser powder- and wire-based technologies are also adopted. The powder preparation is an important step in order to create a homogenous micro structure. The cytocompatibility, that means antibacterial resistance, is an important property of this alloy and it can be improved by Cu addition, being careful of not overcoming the recommended limit for the human health.

Stainless steels usually adopt SLM technologies; Fe-Si and the other magnetic alloys prefer powder bed fusion technologies because these lead to highly textured materials and this is needed to have an optimal axis of magnetization; maraging steels have been processed through wire arc AM.

Pure copper is usually processed by EBM; Inconel 718 by EBM, SLM and LPBF [37]. TiC reinforced NiTi based composites and Ti-Al based composites have been created by SLM.

Fe-Cu-Ni alloy has been manufactured by a combination of SLM and etching for a sub-micron porous honeycomb structure.

Pure titanium is preferentially processed by SLM.

In binder jetting it is important to underline that the choice of the powder and of the binder is crucial for the quality of the final product [9]. In particular, powder shape and size must be studied as important factors. Size has effects on flowability, density and surface roughness: finer powder decreases flowability and surface roughness and it increases density in the part. Shape is important because a spherical is almost ever preferred because it enhances flowability and it reduces friction during the process. Binders can be organic, that binds the powder through curing process, or inorganic, that binds through colloid gel formation.

When there are problem with corrosion for the metallic parts, the first thing to do is increasing the hardness of the material, being corrosion rate inversely proportional to hardness. With AM, enhancing of hardness can be achieved in different ways. Metal/ceramic composites can be chosen as materials. Demonstrations in literature are reported for cobalt based alloys and titanium based materials reinforced with tantalum, tungsten carbide, titanium oxide and silicon carbide. Corrosion resistance can be improved also by ceramic coatings on metallic implants or the use of solid lubricants, such as calcium phosphate added in CoCrMo alloy. Laser melt injection, LENS, EBM, SLS and SLM seem to be the more studied technology in biomedical field for the creation of structures resistant against corrosion in harsh environment as the human body is.

5.2. SLM

Gharbi et al. (2018) [38] studied a particular Al-alloy (AM2024, Al-Cu-Mg) produced by SLM in micro components with 25 µm thick samples. SLM allows a refined particle size because of the local melting and subsequent solidification intrinsic to the productive method. In respect to the wrought counterpart samples (AA2024-T3), whose second phase is Al_2CuMg (S-phase), the microstructure lacks constituent micro particles and it shows as prevalent second phase Al_2Cu (theta-phase) precipitated over the S-phase. This difference is due to the presence of Si that affects the precipitation mechanism. Other phases, such as Si-, Mg-, Si-Mg- and Fe-Mn-Si- rich particles, are rarely clustered with theta-phase particles. Their presence is related to complex constituent type particles, whose evolution is still unclear.

This work is an initial study that wants to stress the importance of these still non-understand mechanisms related to SLM applied for Al-alloys that need deeper investigations.

5.3. EBM AND DMLS

Fiaz et al. (2016) [39] worked on a multidimensional nanopositioning flexure made in Ti-6Al-4V, processed by EBM, also known as EBAM, for microelectromechanical systems (MEMS).

High strength and low Young's modulus make Ti alloys difficult to process and the tools used for the machining suffer fast wear. EBM solves these problems for dynamical micromechanical applications allowing the production of complex framed structures. In fact, tests have shown that Young's modulus does not vary significantly in respect to the wrought material (110 GPa) and the damping factor is approximately zero, thus the reduction of the resonant frequency of the system to the damped frequency can be neglected.

Rotella et al. (2018) [40] studied the differences in microstructure among EBM (Electron Beam Melting), DMLS (Direct Metal Laser Sintering) and wrought grade 5 titanium alloy (Ti-6Al-4V) micro samples. For EBM the samples have a layer thickness of 100 µm, while for DMLS 50 µm. In EBM, before melting, the powder is kept at 600 °C to stabilize the martensitic microstructure that is then modified in $\alpha + \beta$ microstructure. β phase has got a preferred orientation, contrariwise to the other two samples. In DMLS, microstructure is martensitic with acicular hexagonal closed-packing phase. After HIP (Hot Isostatic Pressing), that reduces residual stress and porosity without improving surface roughness, mechanical properties can decrease because of the grain growth due to the transition from martensitic to α lamellar microstructure (Windmanstaetten microstructure). Wrought samples have got equiaxed primary α grains with intergranular β grains.

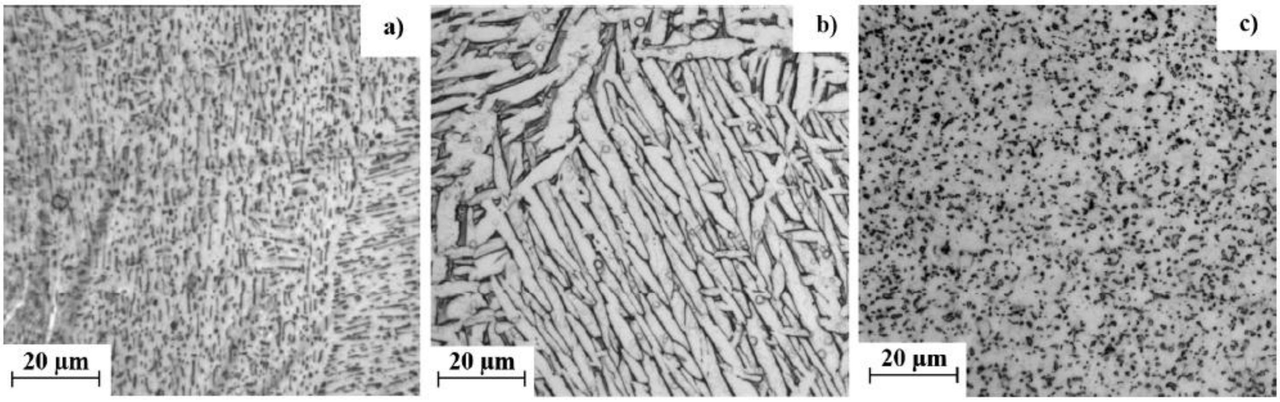

Figure 5.2. *Optical micrographs of (a) EBM; (b) DMLS and (c) wrought Ti-6Al-4V microstructure (a phase in white, β phase in black) [40]*

To allow optical microscopy analysis, the samples are grinded, polished and chemically etched. The characteristic dimensions are:

- 4.29 µm of diameter in equiaxed grains for wrought samples;
- 1.68 µm thick α lamellae for EBM samples;
- 3.46 µm thick α lamellae for DMLS samples.

Nanohardness tests reveal no evident differences among the AM samples, while the wrought samples are softer. In table 5.1, the results with a load of 20 mN are listed.

Table 5.1. *Nanohardness test results [40]*

Method	**Hardness [GPa]**
wrought	3.54 ± 0.14
EBM	4.29 ± 0.27
DMLS	4.46 ± 0.31

DMLS samples result to be 26% harder than wrought samples, while EBM samples 21% harder. This is due to the fact that the cutting process generates a plastic deformation beneath the surface more evident in AM samples, helping them in the resistance against fretting fatigue, for example. DMLS samples got slightly higher values than EBM samples, because, although their coarser structure, their thermal history caused the transformation from martensite to α phase enhancing the hardness.

After the post treatment, as shown in figure 5.3, surface quality increases as the cutting speed increases. Wrought samples reach better results than AM techniques, because they have higher ductility and the parameters adopted in the cutting process are suggested for the wrought material and not for the AM samples. Between EBM and DMLS, the first one has got lower roughness values.

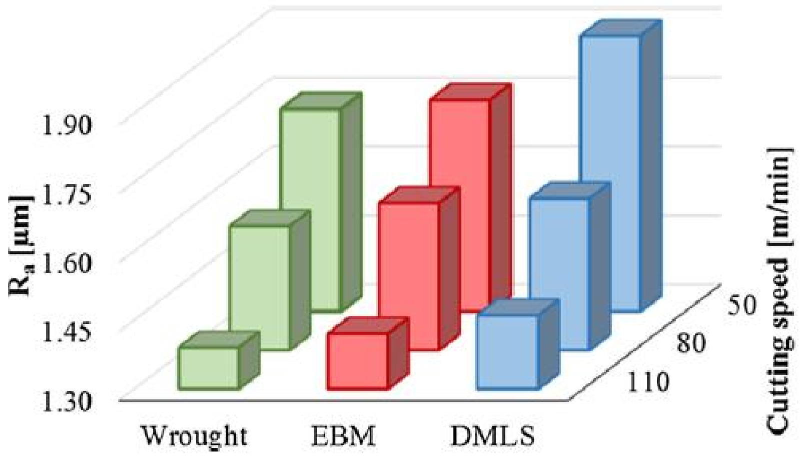

Figure 5.3. *Surface mean roughness results (f =0.2 mm/rev, a_p=0.2 mm) [40]*

Generally, SLM and EBM lead to finer microstructures in respect of the other technologies for Ti-6Al-4V. Moreover, SLM creates less elongated β grains. In terms of fatigue, SLM and EBM do not have significant differences: machining and polishing improve fatigue resistance more than the specific technology. In the micro-field post-processing is difficult to perform, the post-treatment are usually chemical etching and HIP, that deletes porosity enhancing tensile properties, but it decreases yield strength because of the coarsening of α phase lamellae.

5.4. LENS

Ti-6Al-4V alloy produced by Laser Engineered Net Shaping (LENS) is used to study post-processing of the material comparing its properties with the ones of the wrought alloy [41].
AM technologies do not allow to have low surface roughness and hence usually post processes such as grinding and milling are required. Milling is usually chosen because it can offer the best quality to the final part. The problems of titanium alloys are high hardness, chemical reactivity and low thermal conductivity which enhance tool wear. At the micro scale, these problems can get worse. It is already demonstrated that AM samples are more difficult to machine in respect to wrought samples and also the cutting forces turn out to be higher. Using a machine with 1 μm positioning accuracy and 0.02 μm resolution, the samples were printed and then sliced in 3 mm thin layers with a silicon carbide cutting blade at a low cutting speed at 200 μm/min.
The LENS samples show a fine martensitic structure, while the wrought samples have got alfa phase grains and beta phase along the border of the grains. Alfa phase is elongated in the rolling direction. An increase in the laser power causes an increase in the hardness of the AM samples. Burr formation (accumulation of material on the edges of the product) can occur during micro-milling and it is therefore the main problem caused by post-processing. The results of the experiments show how the AM samples have unexpectedly a better surface quality than wrought samples. In theory, AM samples, having higher hardness values, should involve higher cutting force and tool wear. But this does not happen because of the microstructure of the material: alpha and beta phases together in the wrought samples oppose more resistance to the cutting force in respect to the fine martensitic structure. Anyway, AM samples suffer more the problem of burr formation. This is related to the hardness of the samples or the use of increased laser power during production. However, a high laser power

makes the porosity lower, preserving the integrity of the product. Hence, a compromise in the laser power value is needed.

This work underlines that not always in additive manufacturing the post processing is more critical than in subtractive manufacturing, because the particular technology adopted for the production can imply the presence of enhanced properties that are instead absent in conventional techniques.

5.5. μLMWD

The micro laser metal wire deposition (μLMWD) process was studied by Demir (2018) [42] for manufacturing thin walled structures with high aspect ratio (up to 20) and thickness between 700 and 800 μm.

Figure 5.4. *μWLMD system: (a) overview; (b) wire feeder implemented inside the welding station; (c) process obtained through the viewing system; (d) deposition of a thin-walled structure [42]*

μLMWD is a directed energy deposition (DED) process and the system consists of a flash-pumped laser source operating with ms-long pulses and an in-house wire feeding system. More precisely, the feeding material is the metallic wire that is melted by a heat source (plasma, arc, electron beam or laser). Electron beam and laser bring higher precision. Geometrical resolution of the final product can be comparable to the one of PBAM parts. The metallic wire is preferred as feedstock in respect to the powder, because it is easier to stock and to produce. Additionally, wire-based metal AM processes have got high deposition rates and efficient use of feedstock (the loss of material are mainly due to fumes, dross and sparks), with a material use efficiency approaching 100%.

Material use efficiency is defined as:

$$\eta = \frac{V_d}{V_w} \tag{5.1}$$

Where V_d is the deposited volume and V_w is the delivered wire volume that depends on the parameters of the machine. V_w can be calculated for a thin-walled structure as:

$$V_w = \frac{\pi}{4} \cdot d_m^2 \cdot WFR \cdot t \cdot N = \frac{\pi}{4} \cdot d_m^2 \cdot WFR \cdot \frac{l}{v} \cdot N \tag{5.2}$$

Where d_m is the wire diameter, WFR is the wire feed rate, t is the duration for a single layer, N is the number of layers, v is the constant transverse speed and l is the constant length of deposition.

Hence:

$$\eta = \frac{A_d}{\frac{\pi}{4} \cdot d_m^2 \cdot WFR \cdot \frac{l}{v} \cdot N} \tag{5.3}$$

Where A_d is the constant deposited section area.

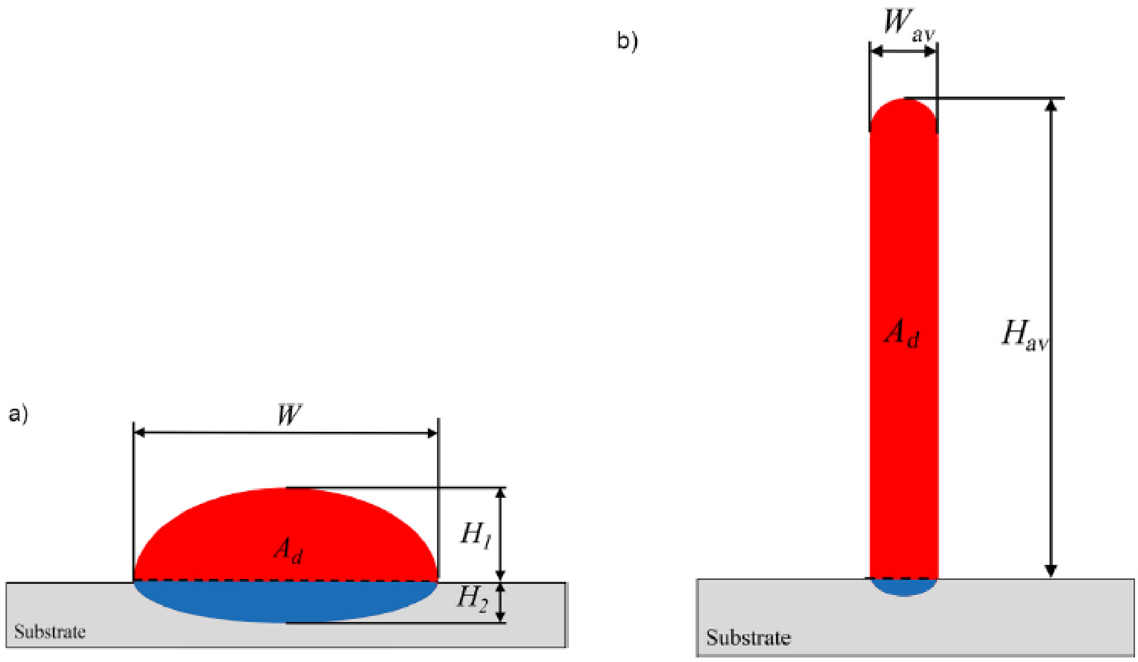

Figure 5.5. *Measurements for single (a) and multi-layer (b) deposition [42]*

In powder bed processes such as SLM and EBM there is the filling of the whole process volume by the powder, which is then selectively melted. This makes the efficient use of feedstock lower. Moreover, reactive powders such as Ti and Al alloys can be oxidized during the process or the recycling lowering the quality.

On the other hand, powder bed processes get benefits in micro scale from the small powder size (15–40 µm), small layer thicknesses (20–50 µm) and small laser beam sizes (30–100 µm). To reduce the geometrical size of a wire feed DED system product, thin wires are essential. Commonly in literature, it can be read that wire diameter is 1 mm and the deposit width is equal to 5 mm, but a micro plasma transferred arc (µPTA) wire deposition process has been already studied and it can produce layer height of 0.5 mm and 2 mm wall width.

In the work of Demir, a µLMWD is developed showing all its advantages in fabricating micro scale components. For example, it can avoid high intensities in the laser because the wire is thin and laser beam diameter can be similar at the wire size, thus it is possible to position correctly the heat source over the deposited wire. The characteristics of the prototype machine are listed in the table below.

Table 5.2. *Characteristics of the prototype machine [42]*

Parameter	Value
Laser system	Trumpf PowerWeld HL 124P
Laser type	Flash pumped Nd:YAG
Emission wavelength	1064 nm
Maximum average power	120 W
Maximum peak power	5 kW
Maximum pulse energy	50 J
Pulse duration	0.3–20 ms
Pulse repetition rate	1–300 Hz
Beam parameter product	16 mm · mrad
Minimum beam diameter	300 µm
Maximum wire feed rate	900 mm/min
Wire diameter	0.3–0.5 mm

Wires of AISI 301 austenitic stainless steel with a diameter of 300 µm and substrates of AISI 316 austenitic stainless steel are investigated as test materials for this technology. Workability, formability and weldability of the steels are good.

The experiments give the following conclusions:

- pulsed wave laser emission at 1 µm wavelength and ms range pulse durations are the optimal parameters for the wire melting;
- high pulse energy and pulse duration cause wider and shorter layer height and more dilution, the processing conditions may create layer width larger than twice the wire diameter, which should be regulated to remain in the micro scale. Contrariwise, an excessively high or low transverse speed may reduce the amount of deposited material, whereas intermediate values are recommended to stabilize the process;

- in multi-layer deposition, irregular deposition must be kept under control;
- thin-walled structures with layer widths between 700 and 800 μm and layer height between 300–375 μm can be realized;
- the process generates homogenous material properties;
- material use efficiency is high, but it can be reduced by high fluence levels due to vapour and spark generation;
- different shapes are possible to be manufactured;
- the μWLMD process among the wire based additive manufacturing processes provides the smallest dimensions.

A limitation is the mono-directional deposition capability due to the optical arrangement and wire feed direction.

5.6. LAM

Micro fuel cells (MFCs), a good alternative to batteries because of their faster recharging and higher energy densities, can be additively manufactured and the first devices following this technique were realized by Scotti et al. (2016) [43] with laser additive manufacturing (LAM). Ultrafast prototyping is guaranteed by this technology and takes advantage from the miniaturized size of the products. The material that is chosen is stainless steel alloy (medical grade 316L) because it is hard, tough, durable, robust, resistant to corrosion and stable from a chemical and thermal point of view. Two configurations are also compared: one with traditional open grooves and the other one, showing higher performance, with enclosed channels. Maximum current density reached is 1.515 A/cm^2 and maximum power density is 363 mW/cm^2 with a constant potential of 0.6 V and these are remarkable values for many possible applications.

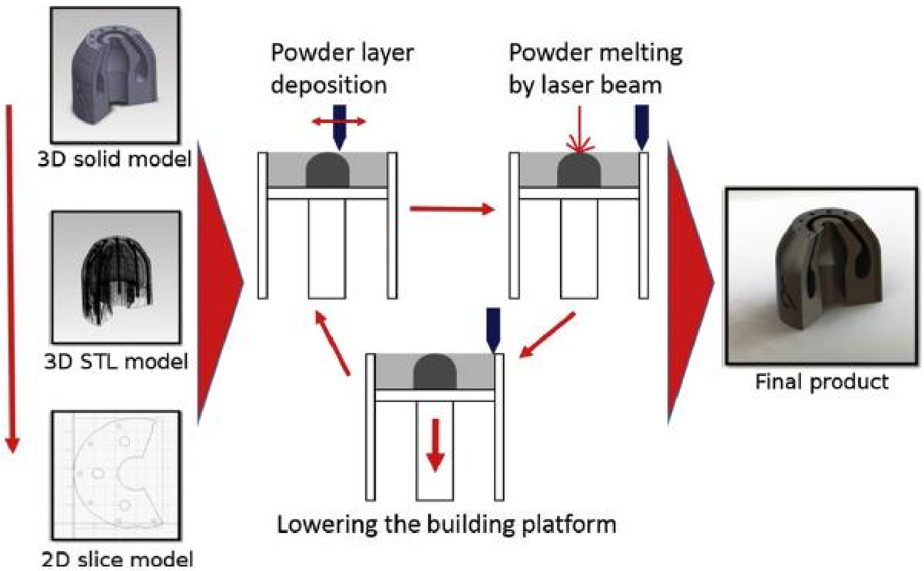

Figure 5.6. Scheme of LAM [43]

LAM is a layer-by-layer AM technology family that uses as heat source a selective laser beam and as primary material a powder. With LAM, single step manufacturing is possible and the design of enclosed cavities makes this technology promising for the production of micro fuel cells because enclosed channels configuration offers a better performance. It is, in fact, proven that with this particular design there is an increase of the contact area between flowfield and GDL (gas diffusion layer) due to the fact that the channels are inside the flowfield plate, while in the traditional design the channel has not electrical contact with GDL. In enclosed channels design, the reactant gases are distributed through apertures connecting the channels and the GDL.

Figure 5.7 shows the structure of the MFC. The flowfield plates have either grooves or enclosed channels and a basin to allocated the carbon cloth GDL. Reactant gases circulate into the flowfield plates entering through two holes each plate.

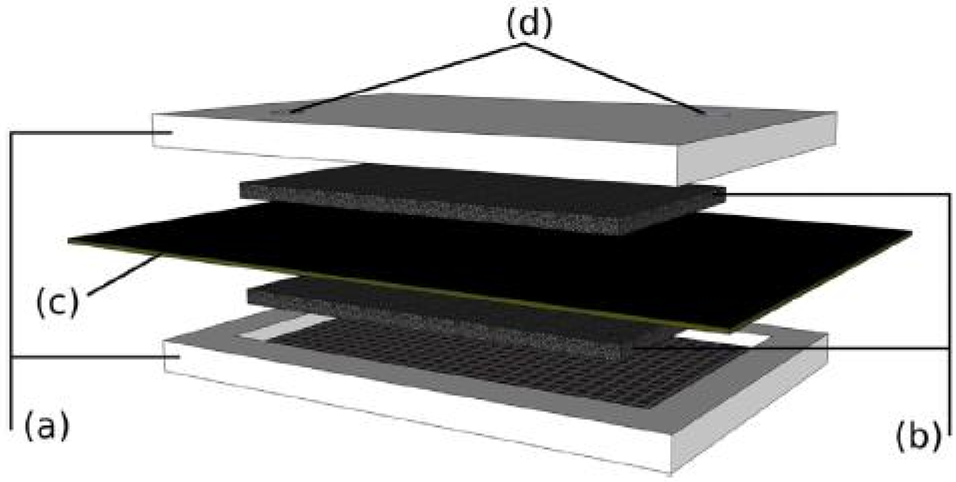

Figure 5.7. *Scheme of the MFCs with flowfields (a), basin (b), GDL (c) and gas inlet holes (d) [43]*

Figure 5.8 shows the flowfield plate: (a) is with grooves (type G), (b) (type E1) and (c) (type E2) with enclosed channels and (c) has got more channels than (b).

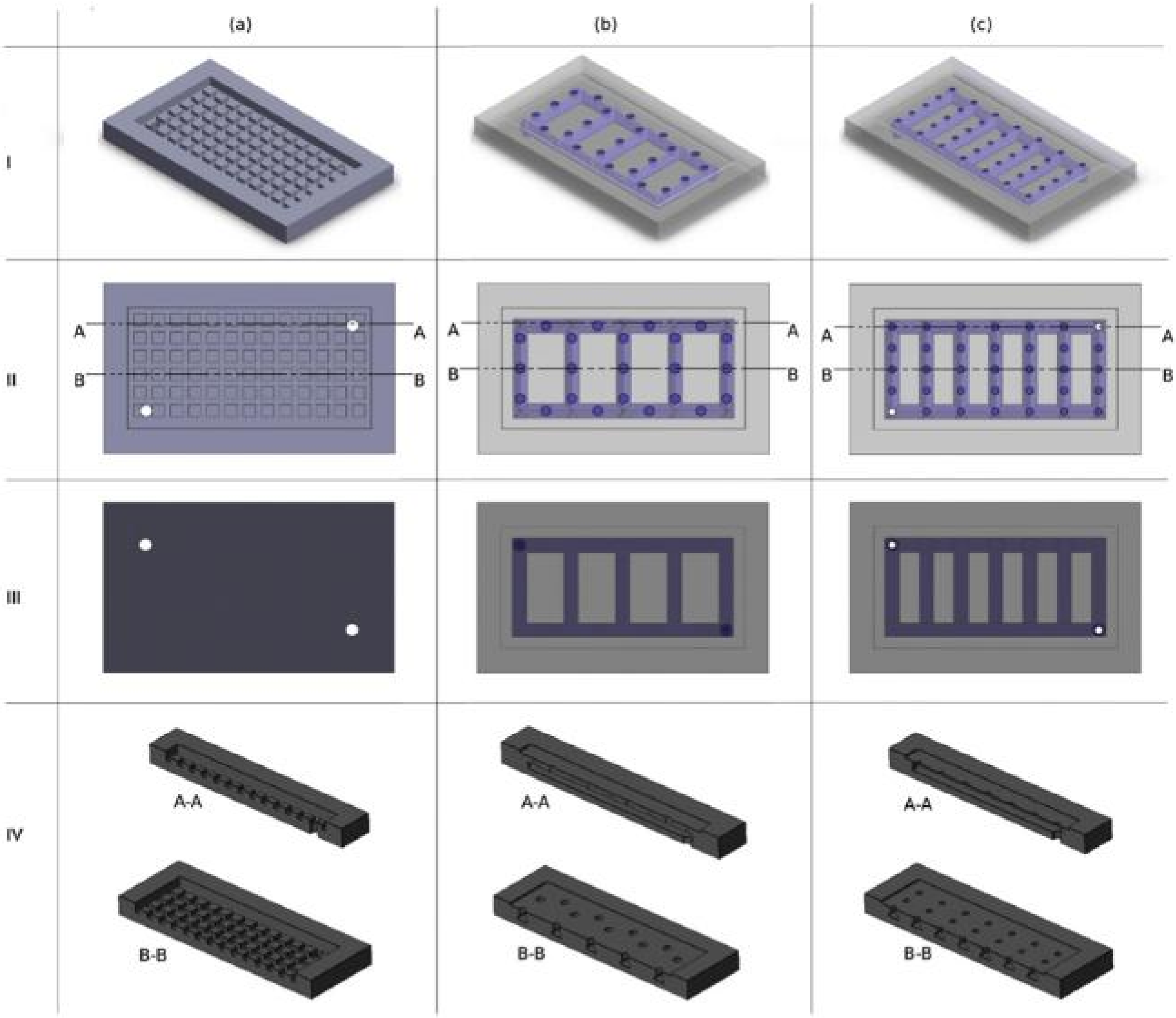

Figure 5.8. *Isometric views (I), top views (II), bottom views (III) and isometric cut views (IV) of type G (a), type E1 (b) and type E2 (c) [43]*

It is important to underline that with enclosed channels, orifices are essential in the part in order to remove the powder not melted by the laser beam and to leave the cavity empty from powder. Another important criterion of design is the angle when overhanging structures are printed: the angle φ must be at least 45° in order to avoid the collapse.

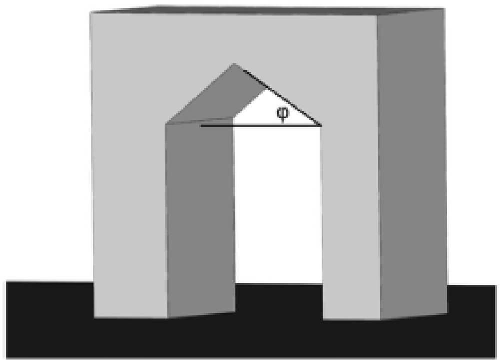

Figure 5.9. *Minimum overhang angle φ [43]*

As shown from the graphs in figure 5.10, type E1 is generally the most performing, slightly more than type E2, essentially because enclosed design presents lower area specific resistance (ASR) due to the higher contact between GDL and flowfield plates.

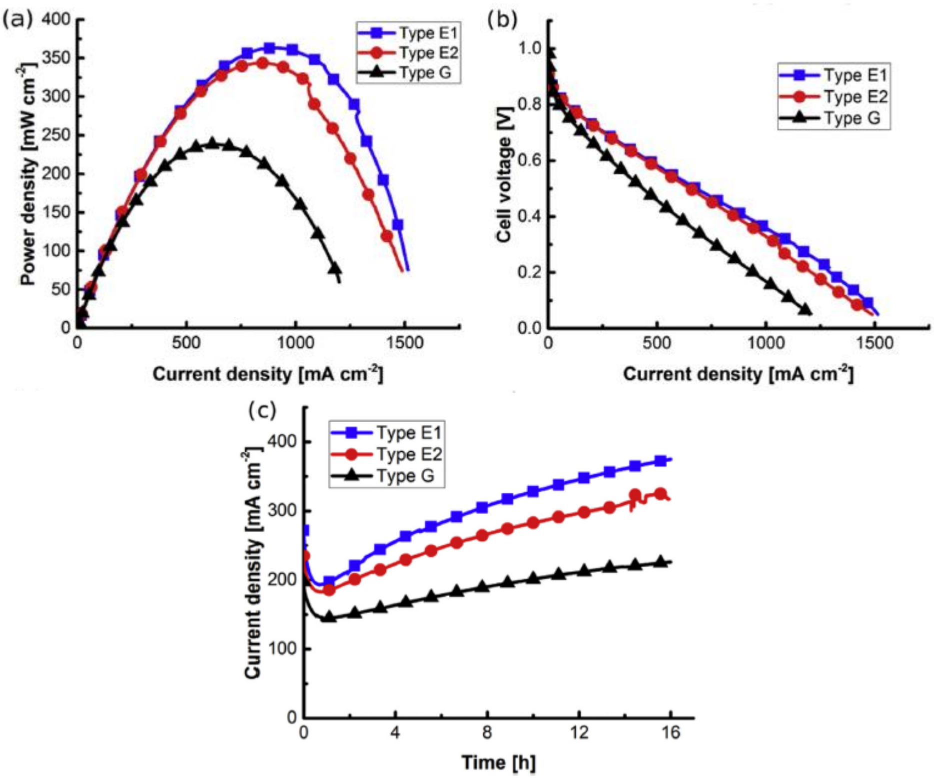

Figure 5.10. *Power density (a) and cell voltage (b) in function of current density and chronoamperometric measurements with 0.6 V across the cells (c) [43]*

The devices turn out to be mechanical and corrosion resistant, because of the stainless steel material chosen. This work underlines the possibility to enlarge the number of possible applications with additive manufacturing technologies if some important design parameters are taken into account.

6. COMPOSITES

6.1. GENERALITIES

Composites are multiphase materials consisting of a reinforcement phase dispersed in a weaker phase, the matrix. Nanocomposites have at least one of their phases with one or more dimensions at the nanometer scale. Nanocomposites are suitable for micro components and in literature some works about their fabrication with additive manufacturing can be found. High performance also in harsh environment is required for more and more applications, especially in the medical field. Polymers can improve their properties and add new characteristic when mixed with nanofillers, such as carbon nanotube, graphene, nanocellulose and nanoclay. For example, high strength to weight ratios and high loads can be reached with these materials converting simple 3D printing techniques to make them suitable for the micro scale [11].

High performance polymers (HPP) are suitable for applications in harsh environment and they are the most studied to be integrated in additively manufactured nanocomposites. The material is stronger in corrosive environment if the bond strength of the material, that is quantified by the bond dissociation energy, is high. The polymer should not have aromatic content because this would makes it excessively stiff and difficult to process. A solution to this problem is adding nitrogen, oxygen or sulfur in the aromatic units. However, the bond strength decreases and hence the thermal stability and the chemical resistance decrease. In order to increase again the bond strength, the polymer should be designed to have got secondary forces (hydrogen bonding, polar interactions and van der Waals forces).

One or more of these factors must be satisfied by HPP:

- Retaining of mechanical, electrical and chemical characteristics after exposure to 177 °C for 10000 hours;

- 5% maximum weight loss at 450 °C;
- Minimal weight loss rate at elevated temperatures;
- When 10% deflection under 1.52 MPa load occurs, temperature should be at least 177 °C;
- High glass transition temperatures;
- Outstanding mechanical properties.

Examples of amorphous HPP are polysulfone (PSU) and polyetherimide (PEI). Examples of semi-cristalline HPP are polyphenylene sulfide (PPS) and polyetheretherketone (PEEK). Examples of liquid crystalline HPP are Kevlar and Vectran.

The most used nanofillers in AM processes are: graphene, carbon nanotube, nanocellulose (nanocrystalline cellulose, also known as whiskers) and nanoclay.

Epoxy-based resin filled with MWCNTs is an example of HPP nanocomposite. MWCNTs are obtained by chemical vapor deposition (CVD) and subsequent acid etching in order to purify them. The nanocomposite can be printed with stereolithography, after the MWCNTs are dispersed homogeneously in the polymeric matrix with ultrasounds and mechanical mixing in order to prevent agglomeration. With 0.10 wt% of MWCNTs, the tensile strength turns out to be increased by 7.5% and the fracture stress by 33%.

Carbon black-filled nylon-12 is a nanocomposite printable by a selective laser sintering 3D printing system that enhances the electrical conductivity of the semi-crystalline thermoplastic polymer nylon-12 without affecting crystallinity.

Nanosilica/nylon-12 nanocomposite requires a surface pre-treatment of the nanosilica before proceeding with the manufacturing process. Nanosilica is then mixed by agitation and ultrasonic oscillations, PA12 pellets are added, N2 gas is added to avoid oxidation, temperature is increased to dissolve PA12, temperature is decreased to precipitate PA12. This nanocomposite is used to increase thermal stability, the tensile strength, the tensile modulus and the impact strength; however, elongation at break decreases by 4% in respect to nylon-12 manufactured by SLS.

Nylon 6/clay-reinforced nanocomposites have got 5 wt% clay nanoparticles (NC) and this material is used for SLS 3D printing. It shows a lower melt flow index and a higher crystallinity index in respect to the unfilled polymer.

Polyamide 12/graphene nanoplatelets nanocomposite enhances the tensile modulus of the unfilled material and it is mainly used by SLS process.

Polyamide 12/CNT nanocomposite is suitable essentially for SLS 3D printing and it is one of the most common AM nanocomposites. Increasing the filler weight percentage, the elastic modulus is improved significantly below the transition temperature and viscosity increases.

Challenges in additively manufactured nanocomposites are: processing, compatibility, dispersion and exfoliation between matrix and filler, cost, consistency, reliability and high lead time. With the proceeding in studies and research, these issues can be overcome, but currently additively manufactured fiber reinforced polymers can face different technical problems [44]:

- Void formation during printing
- Low adhesion between fibers and matrix
- Blockage and wear, because of fillers and resins, in the printer
- Increased curing time.

In macro scale applications different mechanical modeling techniques exist to describe tensile properties. The short fiber composite theory that seems more reasonably adaptable for the micro scale is the modified rule of mixture (MROM), that assumes the interface between fibers and matrix perfectly bonded. The ultimate strength of the composite is:

$$\sigma_{Cu} = \chi_1 \chi_2 V_f \sigma_{Fu} + V_m \sigma_m \tag{6.1}$$

Where χ_1 is the fiber orientation factor, χ_2 is the fiber length factor (their product is the fiber efficiency factor), V_f is the volume fraction of the fiber, σ_{Fu} is the ultimate strength of the fiber, V_m is the volume fraction of the matrix and σ_m is the matrix stress when composite failure occurs.

If the fiber is uniform and equal to L:

$$\chi_1 = 1$$

$$\begin{cases} \chi_2 = 1 - \dfrac{L}{2L_c} \text{ for } L \geq L_c \\ \chi_2 = \dfrac{L}{2L_c} \text{ for } L < L_c \end{cases} \tag{6.2}$$

Where L_c is the critical fiber length and it is defined as:

$$L_c = \frac{r_F \sigma_{Cu}}{\tau_i} \tag{6.3}$$

Where r_F is the fiber radius and τ_i is the interfacial shear stress between fibers and matrix.

Modified Kelly and Tyson model finds empirically χ_1 and studies χ_2 as:

$$\chi_2 = \sum_{L_i = L_{min}}^{L_c} \frac{V_i \sigma_{Fu} L_i}{2L_c} + \sum_{L_i = L_c}^{L_{max}} V_i \sigma_{Fu} \left(1 - \frac{L_c}{2L_i}\right) \tag{6.4}$$

Halpin and Tsai developed a theory in order to predict the longitudinal and transverse Young’s moduli:

$$E_C = E_M \frac{1 + \varsigma \eta V_f}{1 - \eta V_f} \tag{6.5}$$

Where the subscript “C” stays for composite, the subscript “M” stays for matrix, ς is a shape parameter that depends on the direction of the applied load and on the geometry of the fiber and η is the ratio:

$$\eta = \frac{\frac{E_F}{E_M} - 1}{\frac{E_F}{E_M} - \varsigma} \tag{6.6}$$

Where the subscript F stays for fiber.

Voids cause these models to be not precise, but in general, the aforementioned equations can be used in FDM, SLS and extrusion AM techniques in order to investigate the tensile properties of the final products.

Ceramics and ceramic reinforced metal matrix composites (MMCs) have high wear resistance, chemical inertness and stability at high temperatures [45]. Table 6.1 shows the AM processes able to print ceramics and MMCs.

Table 6.1. *Main AM processes for ceramics and MMCs [45]*

Process	**Starting material**	**Technique**	**Ceramic**	**MMC**
FDM	Filament	Extrusion	✓	✓
SLA	Resin, powder	Photo curing	✓	
DIP (direct IJP)	Powder	Inkjet printing (IJP)	✓	
LSD (layer-wise SD)	Slurry	Slurry deposition (SD)	✓	✓
LOM	Sheet	Laser cutting	✓	✓
SLS	Powder	Laser partial melting	✓	✓
SLM	Powder	Laser melting	✓	✓
LDAM	Powder	Laser deposition	✓	✓

Contrariwise to indirect processes, direct processes do not use binder materials and hence a post-sintering process is not needed: they combine forming and densification processes in order to get the final parts, thus giving them higher purity, higher density, better mechanical properties and higher velocity and less energy required in the production. Moreover, direct processes have got as heat source a laser: high energy intensity and high directionality are guaranteed so that a wide plethora of materials can be processed and a micro-scale focal region can be hit by the laser.

SLM is a technology that allows to create near full-dense-parts with better mechanical properties than SLS. Moreover, it is easily scalable. SLS can only partially melt the powder giving thus to the products low density, poor mechanical properties and a limited number of applications.

6.2. SLM

The laser 3D printing is able to produce fine microstructures in the laser cladded layer because the solidification rate is high [28]. Moreover, in situ reaction during the laser cladding process, addition of refractory particles and of rare earth elements into the raw materials make finer microstructures. In literature many examples about these factors can be read. The mixed titanium and SiC powder particles can be used as raw material for SLM and there is the in situ formation of TiC/Ti_5Si_3 composites. Furthermore, the low energy in the SLM process causes the formation of TiC particles with the size of 500 nm enhancing in this way the mechanical performance of the part.

Rare earths can reduce the risk of formation of pores, cracks and inclusions and they enhance tribo-mechanical properties.

A method to enhance the wettability of the ceramic material is to preheat it, for example through an electromagnetic field (induction heating) or vibrations incorporated into laser cladding process. In fact, this procedure causes the so-called agitation effect of the molten material, realizing a finer microstructure because of the increased diffusion, physical and chemical reactions. Additionally, vibrations break growing dendrites homogenizing the powder.

In this way, it is possible to additively manufacture "nano reinforced composites", such as Inconel 625 with micro-sized TiC reinforcing particles (more promising in respect of Al_2O_3 and SiC). During the process the ceramic constituents are completely dissolved and during the cooling process they re-precipitate at a smaller scale. This enhances the strength of the material, reducing crack formation because of the Orowan mechanism.

6.3. SLS

Copper nanoparticles (Cu NPs) are interesting because they can be used in microelectronics applications [46].

Numerous methods can synthesize Cu NPs in powder or ink forms: chemical synthesis methods (for example chemical reduction and micro-emulsion assisted techniques), physical synthesis methods (for example laser ablation synthesis and electric explosion of wire) and biological synthesis methods. Chemical synthesis methods produce more uniform NPs because they control size and morphology of the particles in a better way.

In the chemical reduction techniques, a copper salt is reduced by a reducing agent in the presence of a stabilizing agent, such as the glucose. In laser ablation synthesis an important factor is the type of laser, number of pulses, pulsing time, and type of solvent used in the ablation process.

In electric explosion of wire, high-voltage and powerful impulse flows through the wire until its explosion into NPs, that can have different sizes, from the nanoscale to the microscale.

A technology that is suggested to create materials with Cu NP is microscale selective laser sintering (μ-SLS). If powder size is on the order of tens of microns, properties are similar to the ones of the bulk material, but when it is less than a micron, differences can be significant.

M-SLS system is able to reach 1 μm feature sizes. The primary application is microelectronics packaging, hence Cu gets relevancy for its application as interconnection in integrated circuits with good electrical conductivity and lower cost in respect to silver and gold.

To get feature sizes of 1 μm, NPs are required. The main problems of NPs are agglomeration, due to their high surface energy, oxidation, due to their high area-to-volume ratio and the fact that van der Waals forces dominate over gravitational forces at the nanoscale, thus producing differences between microscale and nanoscale particles.

NPs should have some properties to fit for a μ-SLS production:

- average particle size of less than 100 nm;
- low agglomeration tendencies;
- low levels of impurities;
- low oxidation;
- spherical morphology to reduce the energy required by the sintering process.

Agglomerates in the bed negatively affect the flow behavior, increase porosity and thus lower part density. If the shape of the particle is irregular there will be higher interparticle friction, that decreases the flow behavior and density. The morphological properties, the microstructure and phase evolution of particles are strictly connected to the synthesis process.

40 nm Cu NP samples produced by electric explosion of wire without any surface coating have got the narrowest particle size distribution. Surface coatings in fact can produce long fibrous chains instead of spheres.

The higher Cu content is, the more the properties are similar to the ones of the bulk material. The inks start to sinter at temperatures higher than nanopowders because before the organic layers and residual solvents have to be decomposed. The optimal sintering temperature for the inks must be high enough to decompose the polymer surface coatings but below the melting temperature of the NPs.

This work underlines the possibility of producing composites in AM techniques, such as μ-SLS, and it offers an idea of the reachable features that can be printed when nanoparticle powders are chosen as feeding material.

6.4. LDAM

Laser deposition additive manufacturing (LDAM) shows low labor intensity and high fabrication efficiency in respect to SLS and SLM [45]. However, poor bonding, cracks and low toughness can still be seen in LDAM products. LDAM mainly includes laser engineered net shaping (LENS) and direct metal deposition (DMD). These materials are hard and have got high melting points (up to 3000 °C), hence they are difficult to process by conventional manufacturing technologies.

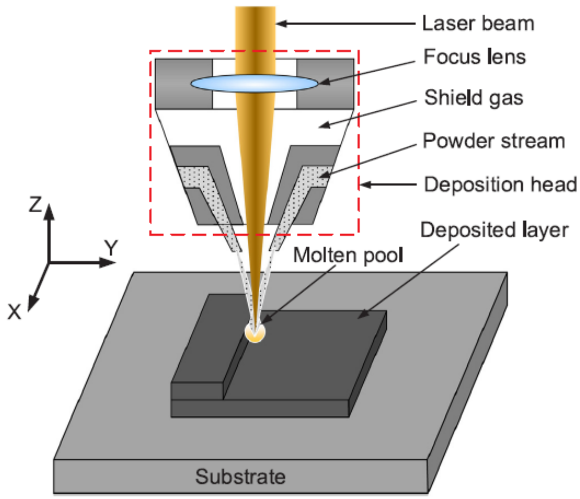

Figure 6.1. *LDAM scheme [45]*

In laser deposition additive manufacturing process (LDAM), a laser melts selectively the substrate casing the formation a molten pool where the added powder is melted. The quality of the products will depend on the energy input. The molten pool solidifies when the laser beams moves away following the designed trajectory until the first layer is built. Each layer has got the function of the substrate for the next layer when the deposition head moves up. In order to get a uniform layer thickness, to get the expected height of the part, to stabilize and to make efficient the laser energy input during the whole fabrication process, it is important to set the vertical increment of the deposition head equal to the layer thickness of the part.

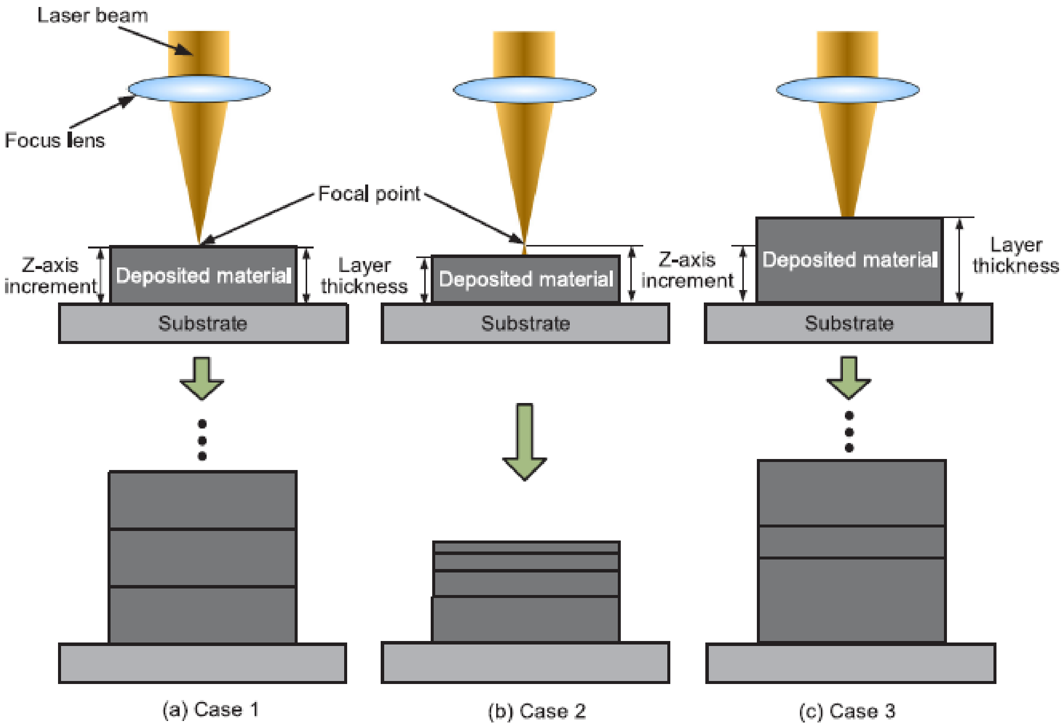

Figure 6.2. *Z-axis increment and layer thickness relations [45]*

Among the possible scanning patterns, offset form outside to inside causes smaller deformation and thermal gradient and better quality.

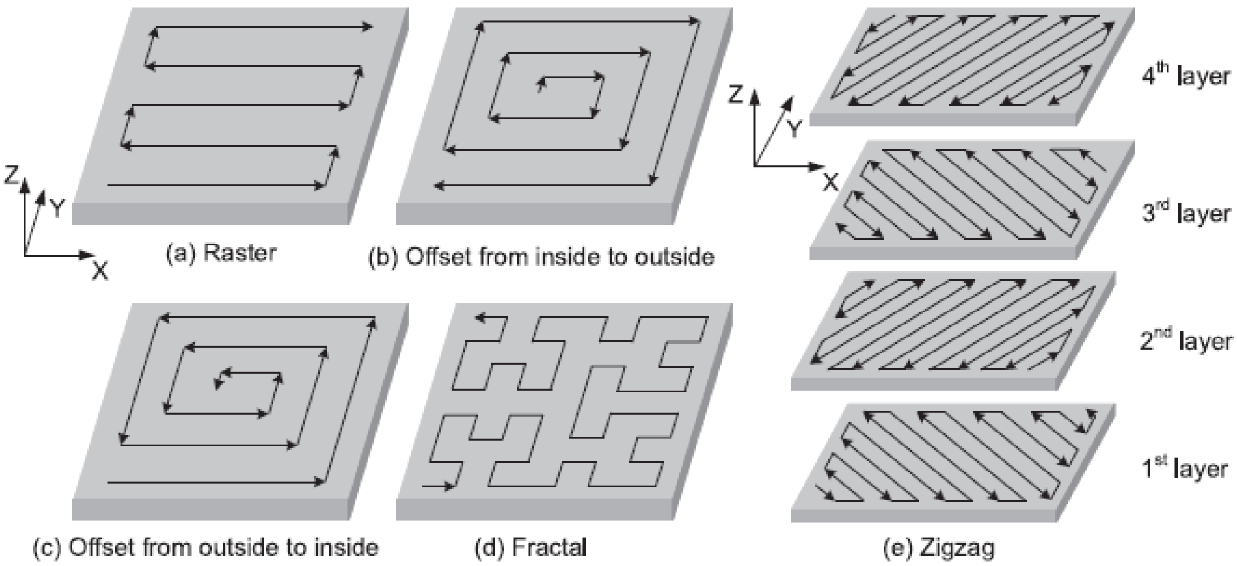

Figure 6.3. *(a) Raster, (b) offset from inside to outside, (c) offset from outside to inside and (d) fractal canning patterns within one layer and (e) zigzag scanning pattern for multiple layers [45]*

In order to increase the mechanical properties in the surface maintaining constant the bulk properties of the material, the laser cladding (LDAM of thin layers) with its high energy density is used as an efficient method.

Ceramic reinforced MMCs have rigid ceramic phases, thus toughness and ductility are penalized. LDAM ZrO_2-Al_2O_3 shows a network microstructure (figure 6.4): ZrO_2 agglomerates on the boundaries of Al_2O_3, that has the function of a matrix, creating a network, that turns out to be beneficial in toughness because of crack bridging, crack deflecting and crack branching (figure 6.5).

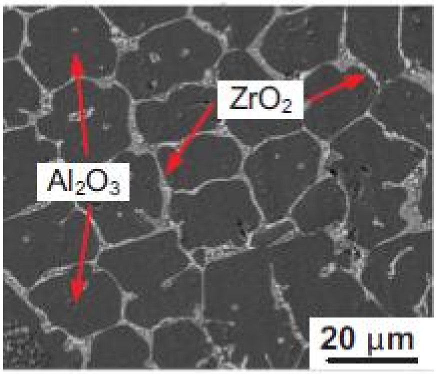

Figure 6.4. *Network microstructure of ZrO_2-Al_2O_3 [45]*

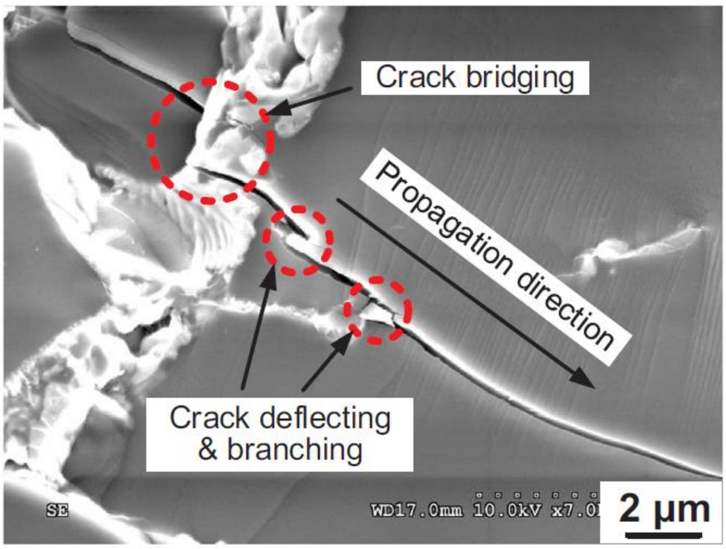

Figure 6.5. *Toughening mechanisms and crack propagation [45]*

When a crack meets ZrO_2 phase is blocked and a new crack generates on the other side of ZrO_2 (crack bridging); the new crack can be deflected when it meets again ZrO_2 (crack deflecting) and then branched into two cracks (crack branching). All these steps require higher energy for the propagation of the crack and hence this mechanism enhances the toughness.

Another method to increase the toughness is the introduction of ultrasonic vibrations, which can enhance the ultimate compressive strength of 60% and the ductility of 15% (fig. 6.6). Additionally, the area under the curve in the graph results to be bigger. The reasons are traceable to three main actions of the ultrasonic vibrations:

- They reduce thermal stress and crack propagation,
- They homogenize the material elongating the crack upon fracture;
- They increase grain refinement making crack bridging, crack deflecting and crack branching reinforced.

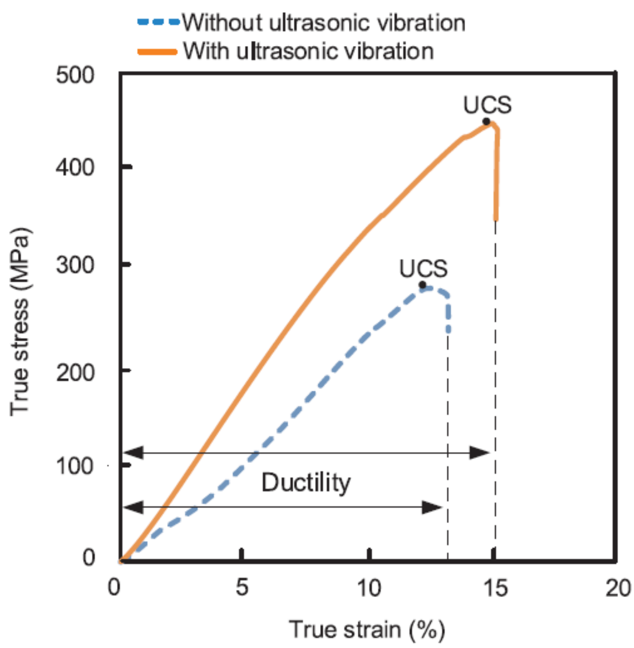

Figure 6.6. *Effects of ultrasonic vibration on compressive properties [45]*

This work is aimed at demonstrating the reasons of reduced toughness and ductility in micro additively manufactured products studying the microstructure of the part, giving important hints for the analysis of the material properties and improvement in the fabrication technique.

6.5. μSLA

Thanks to μSLA, it is possible to build a piezoelectric array with good surface roughness and geometrical accuracy starting from a photocurable resin. This is due to the low power of the laser beam, which limits the defects deriving from the excessive internal stresses.

The solution used to produce this kind of arrays includes soft PZT powder and a photosensitive resin. Inside this last one, there are photo-initiators (catalysers for the polymerization), oligomers (they influence the performance of the product), monomers (they decrease the viscosity) and dispersants (they make the ceramic suspension more stable and homogeneous because they break the aggregates in the powder).

Resin is removed by the green component with thermal treatments. Densities, microstructure, shrinkage and piezoelectric properties of ceramic arrays with different PZT weight content (from 78% to 89%) have been analyzed, comparing the results also to traditional technologies (dry pressing disk) [47].

The PZT weight content is proportional to the density of the component. However, densities obtained by 3D printing techniques are always lower than those obtained through traditional technologies, because of the pores caused by de-binding to eliminate the resins in the green body. Increasing the PZT content, also the grain size increases and grain distribution is more homogeneous.

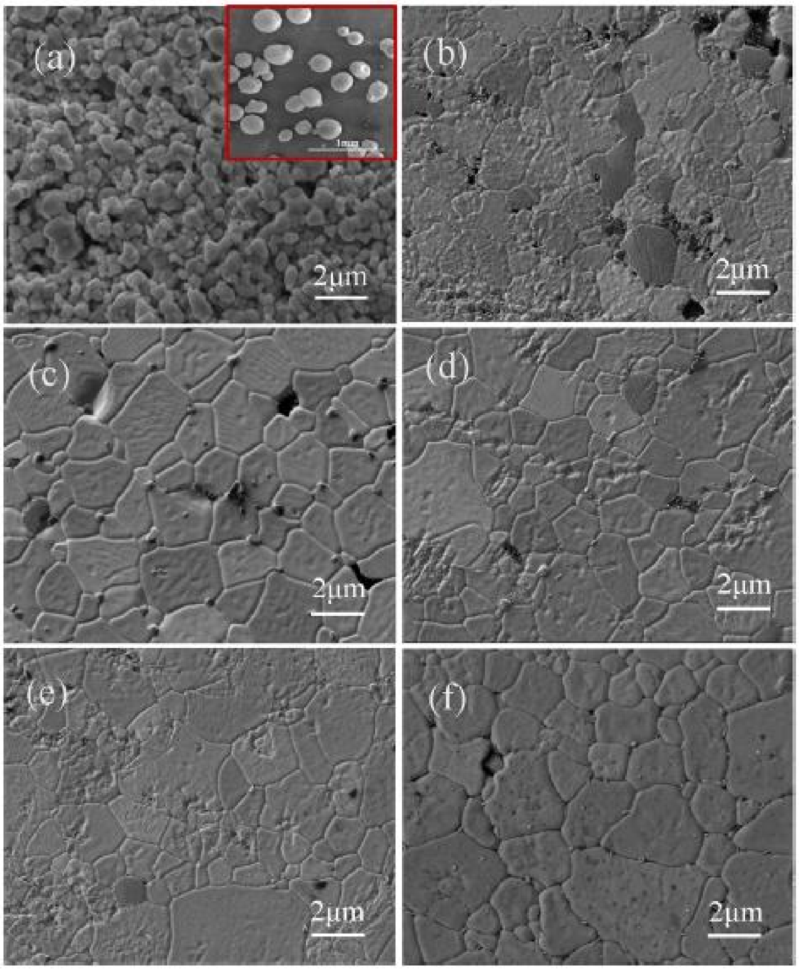

Figure 6.7. *SEM images of the PZT powder (a), 3D printed ceramics with 78 wt% PZT (b), 80 wt% PZT (c), 81.8 wt% PZT (d), 89 wt% PZT (e), pressing PZT disk (f) [47]*

Another issue is relative to shrinkage after the fabrication steps. It is inversely proportional to the PZT content and higher if 3D printing is used. Moreover, in μSLA it is not uniform in the three spatial directions, being lower along the production one.

The piezoelectric constant, which is always lower for 3D printed components, has got a peak for the arrays produced with around 80% of PZT powder content. This composition allows to get high quality and performing components, as shown in table 6.2.

Table 6.2. *Results for different PZT content weight percentages [47]*

PZT content (wt%)	**78**	**80**	**81.8**	**89**	**Pressing**
d_{33} **[pC/N]**	212	334	345	283	410
ε_r	760	1390	1040	765	1900
$\tan\delta$	0.021	0.020	0.020	0.020	0.014
k_t	0.31	0.53	0.53	0.50	0.55

This study is aimed at testifying the high quality product reached by additive manufacturing for micro components for high performance need applications.

6.6. TPL

A lithography-based process is able to print complex metal nanocomponents with a resolution of 100 nm, while today the resolution of many commercial AM machines is 20-50 µm [8]. After synthesizing hybrid materials with Ni clusters, a two-photon lithography (TPL) prints the scaffold and pyrolyzes them in order to volatilize the organics. The strength of the structures is comparable to the one of the architectures printed at the macro scale with other AM techniques. 10 µm octet unit cells with 2 µm diameter beams using TPL with 150 nm layer thickness is feasible.

As the figure 6.8 shows, the beams are fully dense and uniform in dimension. The shape is studied in order to make shrinkage during pyrolysis isotropic.

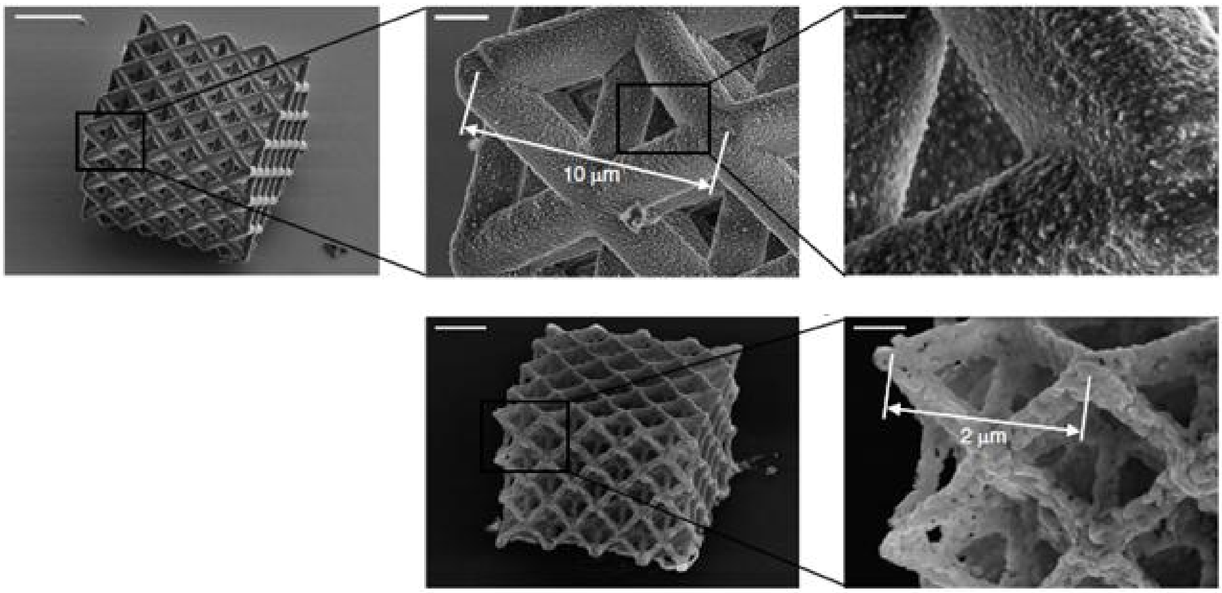

Fig 6.8. *SEM images of the octet lattice made with Nickel-containing polymer. Second line is after pyrolysis. Scale bars are: 15 µm (top left), 2 µm (central column) and 500 nm (right column) [8]*

The chemical composition of the studied samples is: 91.8 wt% Ni, 5.0 wt% O and 3.2 wt% C. There is also a small quantity of Si. The distribution is homogeneous without agglomerations.

There is carbon precipitated at Ni surface because it is highly soluble in Ni during the cooling down from the high temperature of pyrolysis to room temperature. There are also 5 nm sized Ni_3C precipitates within the beams of the structure. Oxygen is due to oxidation of Ni nanoparticles on the surface.

In figure 6.9, engineering stresses are obtained dividing the load by the cross section area of the samples and engineering strains by dividing the displacements by the initial height of the samples.

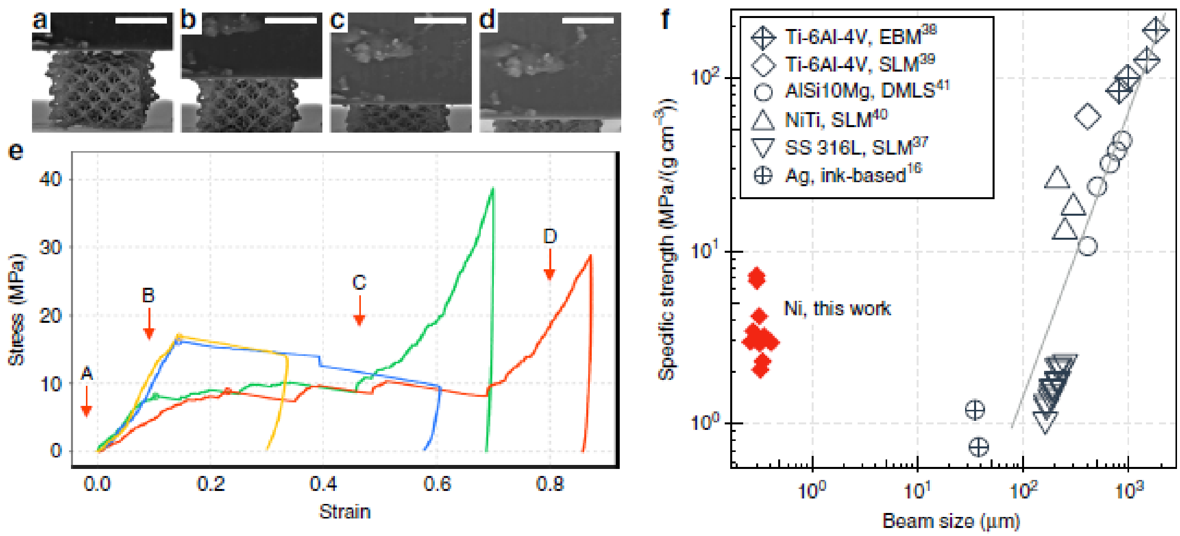

Fig 6.9. *Uniaxial compression of 3D printed nickel octet nanolattices with scale bars of 5 μm: before full contact (a), in the elastic regime (b), during layer-by-layer collapse (c) and during densification (d). These steps appear also in the stress-strain graph (e). Specific strength-beam size plot of nickel nanolattices and other metal lattices fabricated using SLM, DMLS, EBM and ink-based methods (f) [8]*

The in-situ instrument used to get loads and displacements is a nanomechanical indenter, that creates the deformation and collects data for a uniaxial compression experiment of Ni octet nanolattices with beam sizes of 300-400 nm. The results show a typical behavior of compressed cellular solids, with elastic loading, plateau and densification steps, with good values for many possible applications. In figure 6.9 (e) region A stays for the initial contact, region B for the elastic deformation, region C for the layer-by-layer collapse and region D for the densification.

The stiffness of the nanostructures is between 47 and 174 MPa and these values are obtained studying the slope of the region of the elastic deformation. The strength of the structure is the maximum stress reached before buckling (open circles in the graph) and has got values between 6.9 and 18.2 MPa. The two samples which received a compression up to 70-85% strains reached densification, the other two were unloaded at 30% and 60% strain. After deformation there was not recovery for the samples.

Figure 6.9 (f) plots specific strengths in relation to the beam size of Ni nanolattices and other AM metallic lattices. Although calculations were made with the assumption of monolithic beams, the high specific strength is preserved for Ni nanostructures with an order of magnitude lower in dimension in respect to the other techniques and materials. The monolithic beams assumption underestimate the values because in reality the structure has 10-30% porosity that decreases its density and creates many sites of stress concentration.

The speed of fabrication of the sample using hybrid organic-inorganic photoresist is high, ranging from 4 to 6 mm/s. The nanoscale metal AM technique studied in this work is not only for nickel, but also for organometallics from which it is possible to get UV-curable metal-based photoresists.

The level of miniaturization reached by this technology is the most detailed among the works studied in this thesis and it is promising for a large number of applications in different fields.

6.7. FDM

Gnanasekaran et al. (2017) [48] investigated two non-conventional polymer nanocomposites printed via FDM in order to create micro components. PBT/CNT (polybutylene terephthalate/carbon nanotube) products show better mechanical and conductive properties than PBT/graphene ones. Printing multimaterials with abrasive conductive fillers is a challenge, because there could be the problem of the nozzle jam. In fact, agglomeration of the nanofillers can reduce printability, especially at micro scale, and increase surface roughness. To avoid this problem, it is necessary to control size and size distribution of the filler and the process parameters, such as temperature, speed and residence time. The composite material must have high flexibility and must bring to the desired mechanical and chemical properties. If temperature or residence time is excessive, degradation of the polymer matrix can occur decreasing electrical conductivity. The printing temperature of the material is conventionally slightly above the melting temperature of the polymer and this temperature should be adapt to the regime temperature of the 3D printer. Surface modification of the CNTs or the graphene brings a better dispersibility but makes electrical conductivity lower, hence non-modified materials are suggested.

Graphene-based composites result more brittle and rough compared to the CNT-based ones, because high temperature of the process causes evaporation of moisture deposited on the graphite platelets and this causes subsequent voids on the surface.

To make the filaments conductive, at least 0.49 wt% for CNT and of 5.2 wt% for graphene is required. The percentage is higher for graphene because air entrapped between two graphite platelets enhances resistance.

As it is shown by figure 6.10, no large agglomeration is found both for graphene and CNTs. Light regions are the crystalline fraction of the matrix and are similar in quantity for the two materials. White dots represent the gold markers used for tracking. CNTs are mostly located in the crystalline region because PBT tends to crystallize on CNT walls.

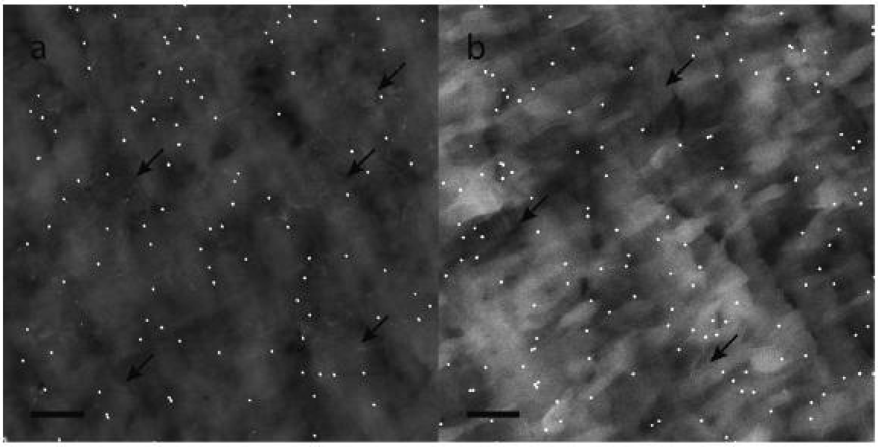

Figure 6.10. *STEM images of PBT/CNT and PBT/G composites with a scale bar of 500 nm [48]*

The degree of crystallization presents a maximum (fig. 6.11). At a certain point, increasing the filler content, the degree decreases because with more filler agglomeration can increase and the polymer matrix chains get immobilized and the formation of crystalline lamellae is limited.

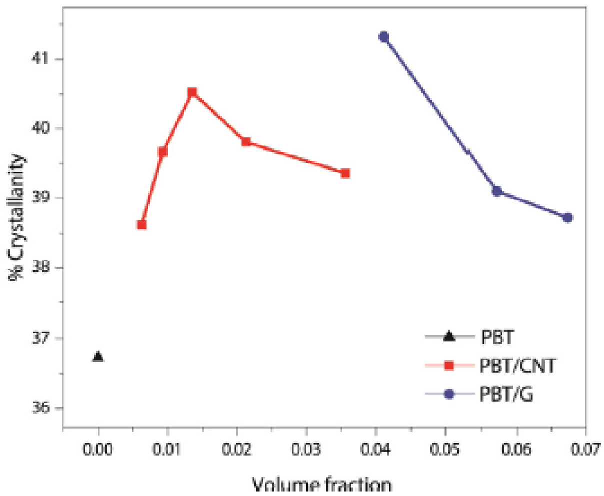

Figure 6.11. *Crystallinity percentage in function of the volume fraction [48]*

Degradation of the material has been studied because it is an important factor of production. It is split in two subsequent steps, as it can be seen in figure 6.12. The first step is in the range of 300-333 °C for the three materials, the last step at 450 °C and it causes total decomposition. With more filler content, the degradation is postponed because it helps the heat conduction during the combustion. PBT/CNT composite is more thermo-oxidative stable than PBT/G composite because at 550 °C there is 6% of mass left for PBT/CNT and only 0.5% for PBT/G.

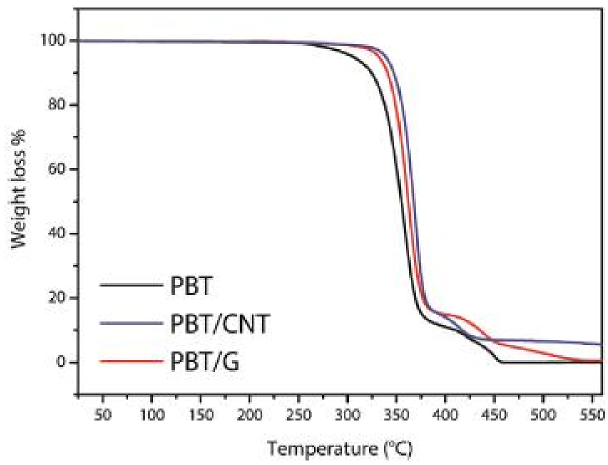

Figure 6.12. *Degradation as weight loss percentage in function of temperature [48]*

Nozzle wear is an issue because CNTs and graphene have a high Young’s modulus. As figure 6.13 shows, with time the nozzle is abraded and the subsequent printed material results to be very rough. A solution is the adoption of a silicon carbide made nozzle, thus preserving its shape and functionality.

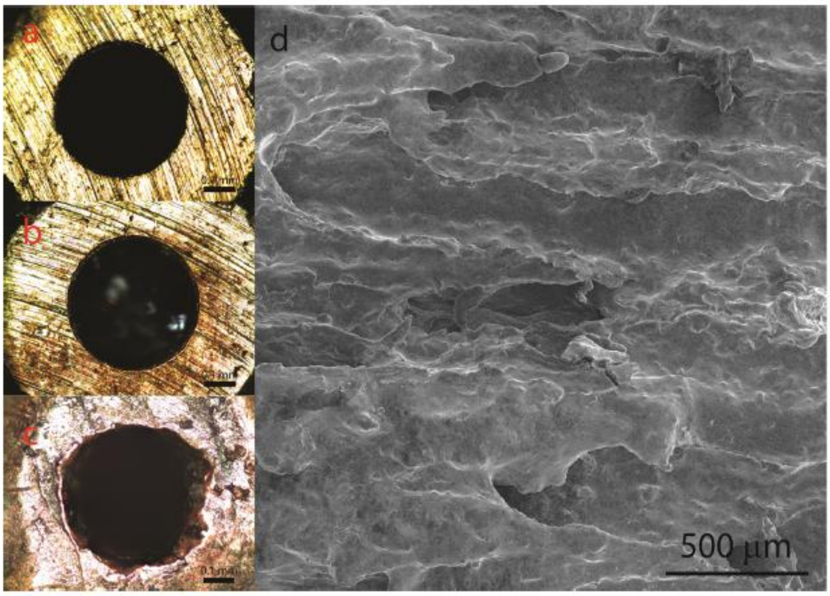

Figure 6.13. *Unused nozzle (a), after extrusion for PBT/G nozzle (b) and for PBT/CNT nozzle (c) and PBT/G composite printed with an abraded nozzle (d) [48]*

6.8. LDM

Liquid deposition modeling (LDM) is analogous to FDM, but it has got the advantage of depositing wet and not solid filaments [49]. Nanocomposite-based conductive microstructures can be printed by LDM, where there is the multilayer deposition of polymeric nanocomposite liquid dispersions based on polylactic acid (PLA) and multi-walled carbon nanotubes (MWCNTs) thanks to a commercial 3D printer equipped with a micro-syringe dispenser. A high volatility solvent (i.e. DCM) is required too, in order to make the evaporation of the wet deposited filament faster, thus creating solid microstructures.

Conductive features with sizes of 100 μm can be printed with this technique and materials, but it is important to underline that LDM is suitable for a great variety of nanofillers.

The desired amount of MWCNTs (from 0.5 wt% to 10 wt% in PLA) was dispersed in the PLA/DCM solution during the preparation of the standard samples. The homogeneity of the dispersion of the MWCNTs in the PLA matrix is a key factor to guarantee an optimal printability avoiding the clogging of the nozzle and good conductive properties of the final product avoiding agglomeration of the filler. With 10 wt% or less in MWCNTs, the agglomeration does not occur. Adding more MWCNTs, electrical conductivity of the samples increase.

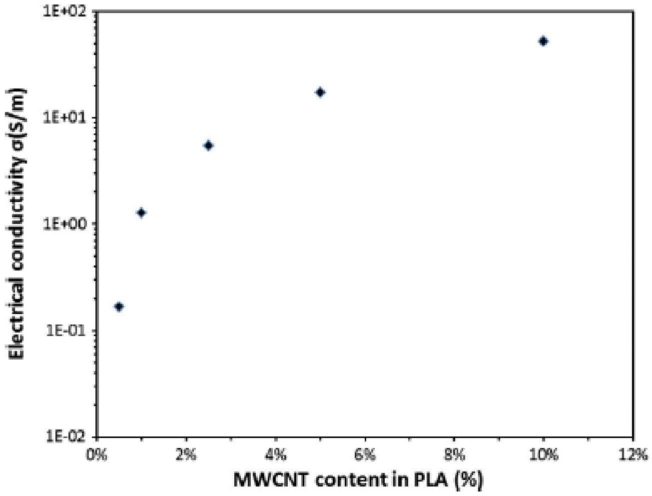

Figure 6.14. *Electrical conductivity as a function of MWCNT percentage content in PLA [49]*

All nanocomposite dispersions show decreasing viscosity with increasing shear rate as shown in figure 6.15.

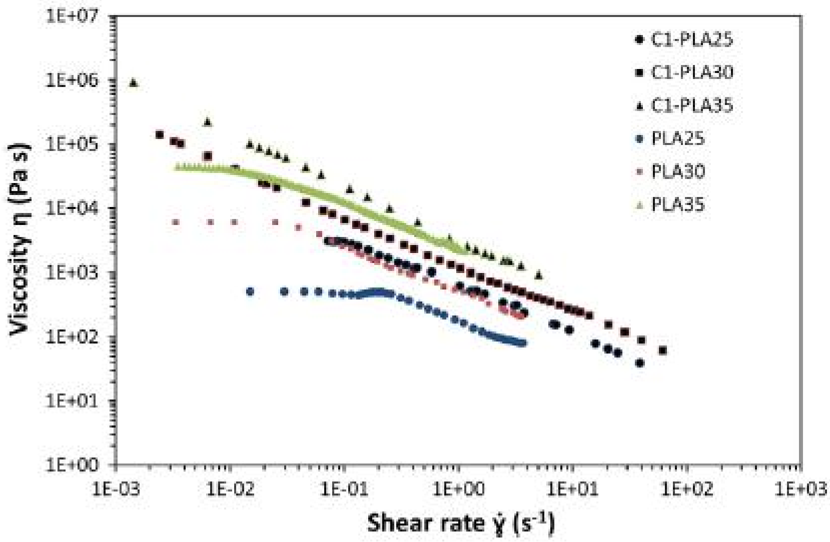

Figure 6.15. *Viscosity as a function of the shear rate for different PLA concentrations in DCM [49]*

Additionally, increasing MWCNT content, there is an increase in viscosity. This behavior is appreciated by LDM technology, because it makes the material processable through the nozzle under high shear rate in the extrusion process.

Analyzing the importance of PLA content in DCM keeping fixed the weight percentage of MWCNTs at the value of 1 wt%, tests show that 35 wt% PLA is not suitable for LDM technology, because the minimum applied shear-stress τ (minimum extruding pressure) is higher than the maximum allowable shear-stress τ_{max} (maximum pressure of the machine).

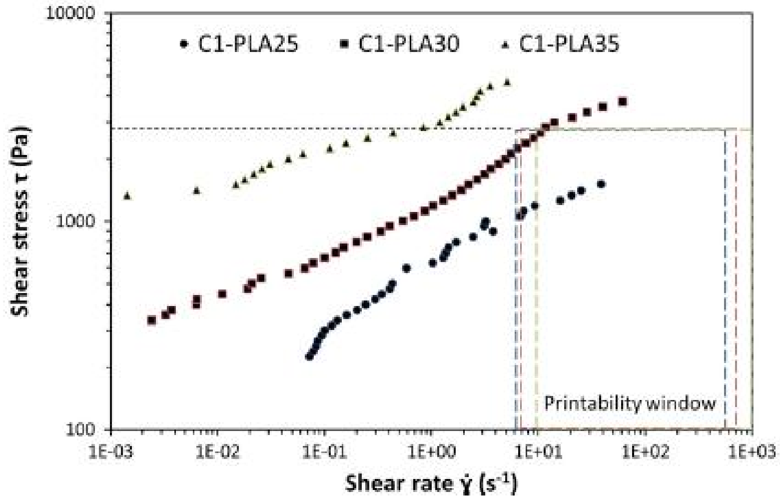

Figure 6.16. Shear stress as a function of the shear rate for different PLA concentrations in DCM [49]

30 wt% PLA has got a very small operating window, 25 wt% PLA has got a broader one: this is due to the different rheological responses of the two materials as shown in fig 6.15. Best resolution is obtained with low printing speeds with 30 wt% PLA, probably because with this composition there is less solvent content.

This work is aimed at stressing the importance of the correct choice of material knowing the limits of the printing machine.

6.9. 3DP

Carbon nanotubes, nanowires, nanoparticles are biocompatible and find many applications in the medical field. Angjellari et al. (2017) [50] built a new hybrid printer machine for AM that can produce composite micro components. As test material, polyvinyl alcohol (PVA) is chosen, because it is an important biomaterial showing biocompatibility, water solubility, abrasion resistance and chemical inertness. It is used in nanocomposites in combination with materials such as detonation nanodiamond (DND) for biomedical and microelectronic applications.

The extruder of the machine is external. A micro syringe acts also as reservoir for the material and communicates with a nozzle with a diameter of 0.25 mm. A piston pushes the material in the syringe and extrusion starts. When a layer is deposited, the syringe rises up of a distance of 50 μm, that is the layer thickness, but this distance can be reduced according to the specific requirements of the parts. A heated metallic platform is used as support. PVA-DND dispersion must be processed after a maximum of 5 days from its preparation to avoid degradation. Factors influencing the part quality are:

- motor rotation;
- printing speed;
- flow rate;
- type of nozzle;
- bubbles in the syringe.

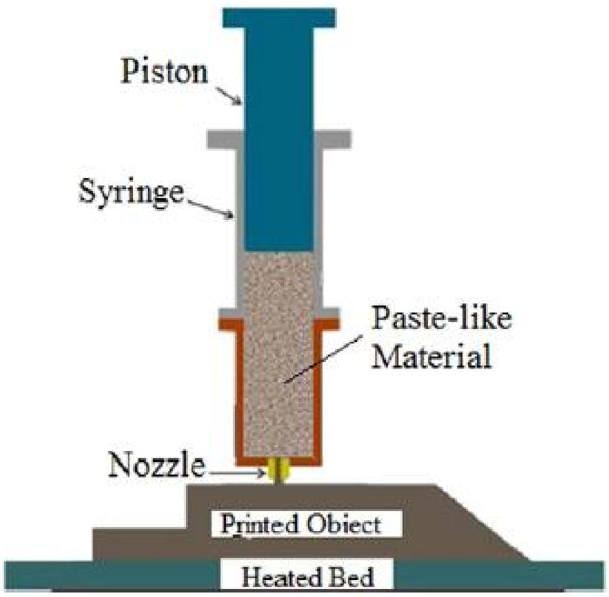

Figure 6.17. *Scheme of the 3D printer used by Angjellari et al. [50]*

Tests reveal that mechanical properties of the material is preserved with the printing process and they can be enhanced accurately by choosing the right composition. Nanoindentation tests show that PVA samples have got an indentation modulus of 180 MPa. This value increases linearly with increasing DND content as described by figure 6.18. The notable value of 550 MPa is reached with 5 wt% DND. This is due to the creation of inter-chain bonding between the components of the nanocomposite that limit the relative sliding of the chains.

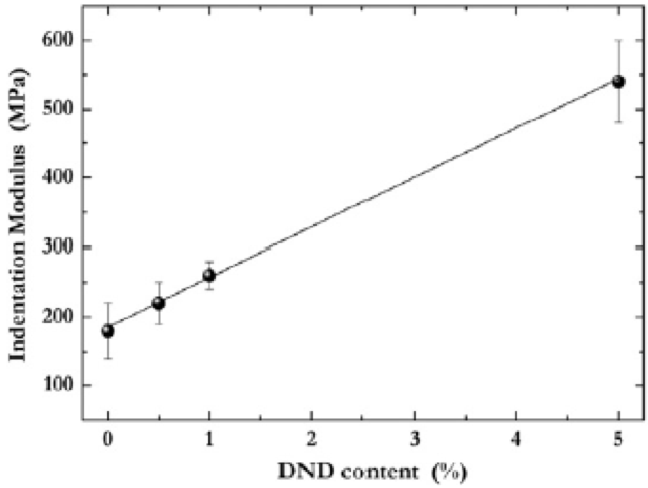

Figure 6.18. *Indentation modulus as a function of DND content percentage [50]*

DND presence produces also an enhancement of the thermal properties with an increase of the melting temperature and of the degree of crystallinity (fig. 6.19).

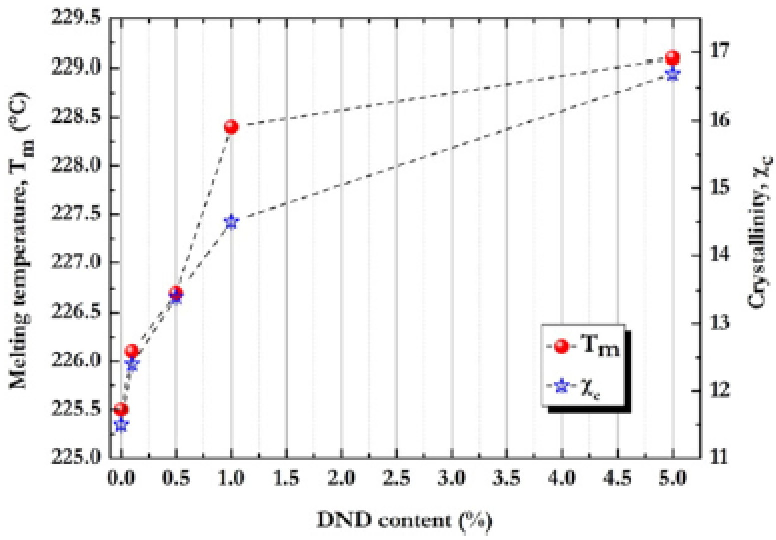

Figure 6.19. *Melting temperature and degree of crystallinity as functions of DND content percentage [50]*

The increment in the melting temperature allows to extend the number of possible applications because the material preserves its mechanical properties in a larger range of temperatures. This is a key point of this study, because it can provide an alternative and more beneficial fabrication technique for many applications.

6.10. DW-3DP

Nanoclays are nanoscale layered silicates used as fillers as a viscosifying agent and in order to improve properties of polymer resins, such as stiffness, toughness, strength, because of their high surface-to-volume ratio and platelet morphology [51]. However, they increase viscosity, thus creating challenges during processes in traditional methods, such as infiltration and casting. In additive manufacturing, the enhancement in viscosity can be used to give better rheological properties to the material.

In 3D printing, epoxy resin can be reinforced with fumed silica particles, that are viscosifyer with weak anisotropy (they will not have a preferred orientation during the printing process), and nanoclays.

Some specimens are created to study a comparison between the two fillers with a direct writing 3DP (DW-3DP) printing machine that can be converted in order to obtain micro scale components. Parameters of the machine are kept constant. With this technology, extrusion is not anticipated by melting, it is done at room temperature (this avoids thermal distortion) and it does not need a immediately subsequent curing process. The material must have a shear thinning behavior in order to be extrudable, it must be highly viscous and have an elastic behavior in order to keep the part shape.

Rheological properties are revealed by a rheometer. Shear thinning behavior is highlighted by the plot apparent viscosity versus shear rate. Apparent viscosity is given by:

$$\eta = K\dot{\gamma}^{n-1} \tag{6.7}$$

Where K is the consistency index, $\dot{\gamma}$ is the shear rate and n is the flow index, that is equal to 1 if the fluid is Newtonian, lower than 1 if the fluid has got a shear thinning behavior and higher than 1 if it has got a shear thickening behavior. The samples turn out to have got a shear thinning behavior and if nanoclay content is at least 2.5 %wt this behavior is remarked.

Figure 6.20 shows that the viscosity of pure epoxy does not depend on the shear rate, but increasing the nanoclay content, viscosity is improved, more significantly for low shear rates. The shear rate experienced during the deposition is similar to 50 s^{-1} and hence the apparent viscosity has a range between 10 and 100 Pas.

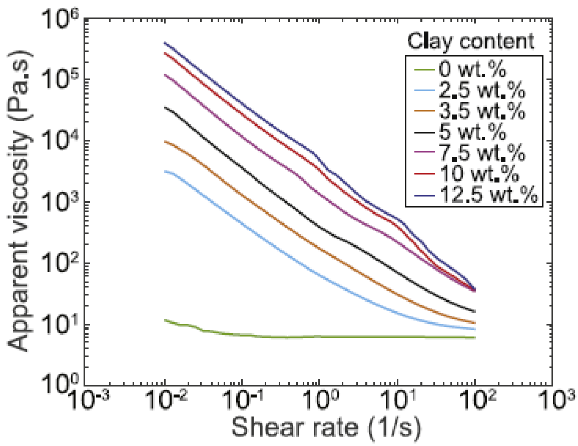

Figure 6.20. *Apparent viscosity in function of the shear rate [51]*

With an increase in nanoclay content, there is an increase of the shear yield stress and of the flexural modulus values. Additionally, thermal degradation is slightly accelerated.

Tests have shown that inks with 5 wt% or less are not solid enough to guarantee the printability of multiple layers. Higher values in clay content make the inks “extrudable” through the deposition nozzle. The nozzle impart an orientation to the nanoclay particles that have a platelet morphology, resulting in a higher anisotropy in respect to fumed silica and hence in better mechanical properties for the final part.

Also this work is an important guideline to study the properties of the components and their variability in relationship to the choice of the material.

7. EXAMPLE OF TOTALLY ADDITIVELY MANUFACTURED DEVICE

In the past, micromachining technologies were the most used to create microfluidic devices with an integrated microelectronic system, but nowadays additive manufacturing provides more advantages and hence it is preferred. In fact, historically, micromachining technologies met difficulties in working with materials such as glass and silicon and soft lithography was invented to overcome this challenge. The first device created in this field with soft lithography was an enclosed channel in PDMS for the transportation of fluids. Soft lithography can be implemented to create multilayer devices, with the advantages of having layers with structures and rigidity different from other layers.

AM approaches try to overcome some challenges that were met with the other methods. For example, they increase automation of the process deleting manual assembly of the devices and they create in a single step the monolithic and multilayer structure.

In microelectronics field the most promising methods of AM are: extrusion-based 3D printing (FDM and DIW), SLA and MJM (or PolyJet).

3D printing techniques, such as SLA, can be used to create a microscale mold in order to give a shape to elastomeric polymers, such as PDMS. The creation of the mold gives possibilities in choosing the optimal geometry, but it is not a versatile technique, because if a new geometry is needed, a demolding process should be started.

An advantage offered by polymer filament-based FDM is the ability to use multiple extrusion heads. DIW method utilizes fugitive ink, that means a sacrificial material that is then casted and removed in order to create hollow structures.

SLA can fabricate microchannels with 18 μm thick features, but the products must be self-supporting [10]. If they are not, then it is necessary to provide a support that could give serious problems in its removal considering the microscale of the final products.

MJM is a fast AM technique and it allows the most complicated geometries because of its ability to print sacrificial supports; additionally, multimaterial printing is possible. A challenge is the choice of the material because not many materials can be processed by this technology. For example, biocompatibility is rarely acceptable among the materials suitable for MJM, but with some procedures it can be increased.

The elimination of the 3D printed support material is a challenge in microfluidic and microelectronics devices. It can be performed with the immersion of the part in heated oil, with the manual inputting of heated oil or pressurized air through a syringe into the microchannels. It is important a proper design, with input and output ports for the post-processing. Instead of producing a wax-based support, it is possible to adopt a water soluble support that dissolves over time (some days are needed).

In microelectronics, more efforts are employed in reaching the desired electric performance more than the desired geometry and size. The most used technology is extrusion-based 3D printing, but recently also SLA has been studied because of its higher scalability.

A combination of more techniques can be adopted, for example the general structure is 3D printed using a well consolidated technology; the electronic interconnects are 3D printed by DIW; commercial electronic components are physically placed during the 3D printing process.

It must be underlined that printing piezoelectric material in the nanoscale presents two major challenges:

- usually these materials are nanoparticles mixed with solvents and polymers and during removal of exceeding material the part can get degradation;

- voids and grain boundaries can generate and become sources of weak points in the structure.

Additive manufacturing is able to create all the parts of a triboelectric nanogenerator (TENG): the electrode layer (EL), the triboelectric layer (TL) and the case package needed in order to make EL and TL aligned. General wire electronic systems can be powered by a grating disk type TENG projected by Seol et al. (2018) [52] and able to provide 231 V, 18.9 µA and 2.13 mW.

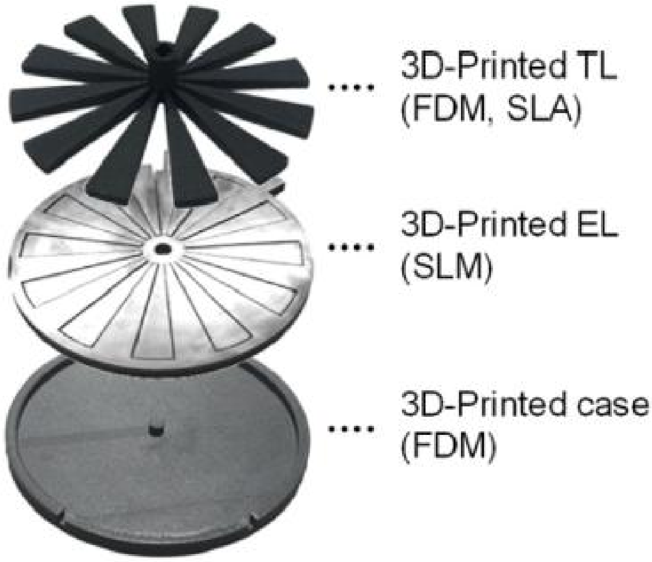

Figure 7.1. *Structure of the 3D printed TENG [52]*

The advantages of fusing together the concepts of TENG and of 3D printing are:

- low energy consumption;
- low quantity of waste;
- rapid prototyping for a continuously developing device as TENG.

Table 7.1. *Materials and printing methods for TENG components [52]*

Component	Material	Printing method
Case	Nylon	FDM
Electrode layer	Al	SLM
	Ti	
Triboelectric layer	ABS	FDM
	PLA	FDM
	MMA	SLA
	Nylon	FDM
	PTFE	Not printed

The material used for the metal blade structures (electrode parts) is titanium grade 23 powder (Ti-6Al-4V ELI). The machine is a 3D metal printer with laser power of 245 W and speed of 1250 mm/s able to print layers with thickness of 60 µm. Samples are thermal treated after printing for reducing internal stress. After this, milling is required to create smooth surfaces.

The cover case is printed with a layer thickness of 25 µm in nylon. For the triboelectric parts four different materials are printed in order to find out the best choice: ABS, PLA, UV photo resin made of MMA and nylon. PTFE is used as reference material, as it offers the state of the art performance.

In the grating disk type adopted for this study, the two electrodes are not placed in the stator and in the rotor, but together in the stator. This penalizes the areal efficiency but simplifies the analysis because electrodes do not move during operation.

The TL (rotor) rotates on the EL (stator). The higher the relative difference of the order of electrification between EL and TL is, the higher the output power is.

When the two layers touch each others, the TL gains static (triboelectric) charges on the contact surface. These charges bring mobile charges with the opposite polarity by Coulombic attraction. Most of the mobile charges are accumulated on the electrode (the inner one or the outer one) when the TL is overlapped with it. Therefore, as rotation of the rotor proceeds, the charge distribution profile of the two electrodes changes generating current between them. The frequency of the charge flow depends on the number of gratings and on the rotational speed. The number of charge transfer cycles is equal to the number of the gratings on the disk multiplied by the rotations made by the rotor.

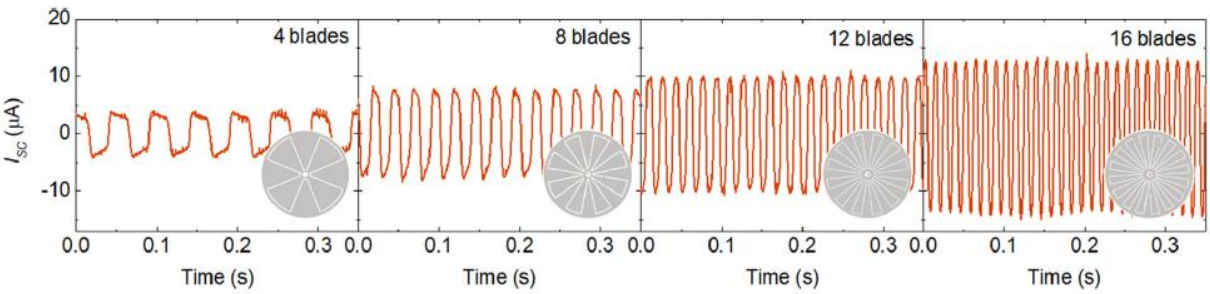

Figure 7.2. *Short-circuit current over time with different numbers of blades [52]*

Tests underline the influence of the number of gratings monitoring the current under constant rotational speed: the higher the number of grating is, the higher the magnitude and the frequency of the current are. This happens because with more gratings, the distance between them decreases and the frequency of the charge transfer cycle increases. Moreover, the magnitude of the current increases because in finer gratings the charge transfer is faster. The magnitude of the current is calculated as:

$$I_M = m_T n_G f_r (A_{EL} - A_L) \tag{7.1}$$

Where m_T is a material parameter linearly proportional to the triboelectric charge density, n_G is the number of gratings, f_r is the rotation frequency, A_{EL} is the area of the EL, and A_L is the areal loss factor due to inter-grating space. A high performance is therefore obtained by higher triboelectric charge density, large size, faster rotation, more gratings and lower areal loss factor.

Figure 7.3 shows rotational speed as a function of root-mean-square current (IRMS), that is the effective amount of generated electricity It has got a linear behavior, that is suitable for sensor applications. For example, the velocity of a flow can be obtained starting from the magnitude or frequency of the signal from the sensor. The higher the number of gratings is, the higher the slope is. Faster rotation implies faster charge transfer, which enhances both charge transfer frequency and magnitude.

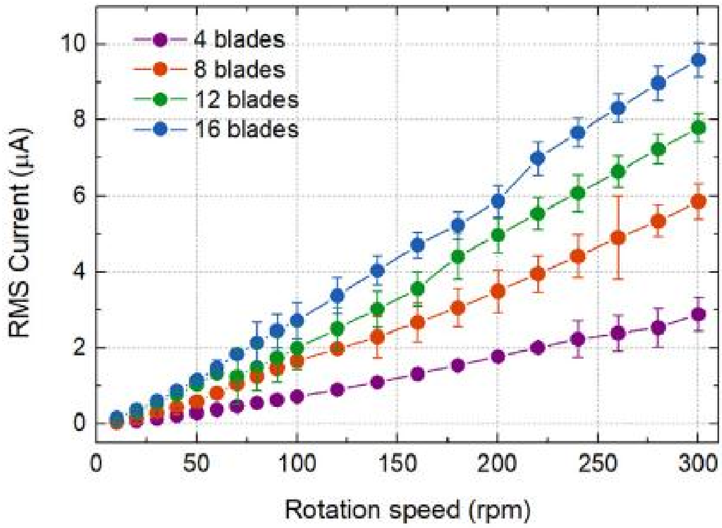

Figure 7.3. Root mean square current over rotational speed with different numbers of blades [52]

Al and Ti are chosen as EL materials for the tests, while ABS, PLA, MMA, Nylon and PTFE as TL materials. As shown in figure 7.4, during the initial contacts, the triboelectric charge density increases (transient phase) until a maximum, reached after sufficient contacts. Later, the saturation occurs for all the materials and this is visible by a plateau in the graph.

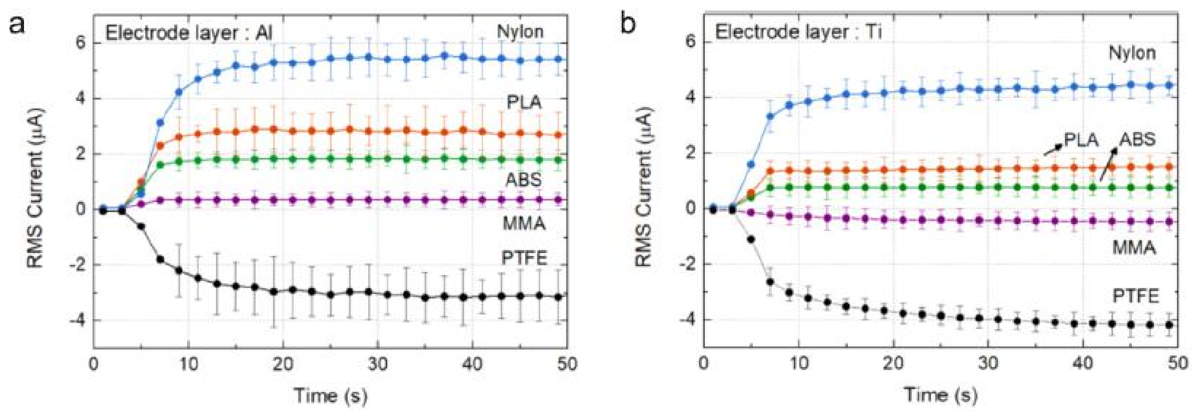

Figure 7.4. *RMS current over time for various TL materials when El material is Al (a) and Ti (b) [52]*

The polarity of the charges depends on the position of the order of electrification.

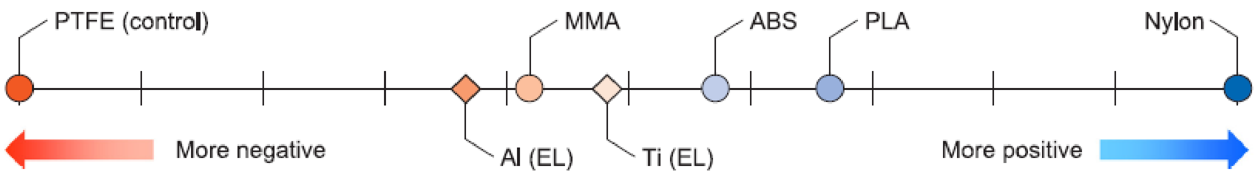

Figure 7.5. *Relative positions of the order of electrifications [52]*

The triboelectric charge density after saturation can be calculated. EL material turns out to be not very influent in the charge density. For the TL material, the highest value is reached by Nylon when EL material is aluminum. In this case the triboelectric charge density is 31.2 $\mu C/m^2$.

This work underlines the possibility of creating an entire device by additive manufacturing without losing in performance.

8. PROJECT

8.1. INTRODUCTION TO BIOMEDICAL APPLICATIONS

In medical field, an advantage provided by AM is the ability to create structures that are able to mimic the natural and real porous structures of the human body such as bones and the vascular system. Additionally, it is a rapid procedure to create ad personam medical devices taking into account the real needs of every patient. Table 8.1 summarizes the main AM technologies used in biomedical field and their minimum reachable layer thicknesses [5].

Table 8.1. *Main AM technologies and characteristics used in biomedical field [5]*

Technology	Source material	Layer thickness [µm]	Temperature stability [°C]
µSLA	Liquid photopolymers	-	-
	Ceramics	50	80
PolyJet	Acryl-photopolymers	16	50
MJM	Acryl-photopolymers	16	50
3DP	Chalky powder	-	-
	Ceramics	150	115
	Composites	-	-
FDM	Plastic filament	100	80
	Composites	-	-
FFM	Plastic filament	100	260
EBM	Metal powder	50	500
SLS	Plastic powder	100	80
	Ceramic powder	20	300
	Composites	-	-
SLM	Metal powder	20	350
2PP	Photoresists	<1	100

The most used AM technologies in medical field for metals are EBM, SLS, SLS and LENS; while the most used materials are titanium and its alloys, cobalt-based alloys, 316L stainless steel and nickel-titanium [2]. In fact, high biocompatibility for biomedical applications are reached by metals such as stainless steels, cobalt-chromium alloys, titanium alloys and tantalum alloys. Small grains and a better mechanical performance are the advantages that 3D printed metal materials for biomedical applications show compared to traditionally manufactured implants. Ti-6Al-4V is the most used alloy in medical applications. Ti-Nb alloys have a very low elastic modulus and high strength and biocompatibility. Ta can be added to increase the reduction in elastic modulus in order to make stress shielding less dangerous. Ni-Ti shows high resistance to fatigue because of its superelasticity. Magnesium can be used in orthopedics because its elastic modulus is similar to the one of the bone, it can be absorbed by the human body without negative effects and it shows low corrosion, thus lowering the effect of the stress shielding. Co-Cr based alloys are widely used in orthopedics and dentistry because they have high biocompatibility and good mechanical properties.

Ceramics are important materials in medical field because they have got stable physic-chemical characteristics and high biocompatibility and osteoconductivity. SLS and SLM can be adopted for the creation of prosthesis in ceramic materials [53].

Micro AM gives also opportunities in applications for regenerative medicine, tissue engineering with the creation of complex and biomimetic 3D structures [12]. Biological tissue, such as the vascular system with large and small vessels and capillaries, whose characteristic dimension can be 200 μm, can be easily resembled by AM technologies that are able to print multiple material, cell types and biomolecules that are then in vitro cultured. Conventional techniques for creating this kind of structure are: cell sheet engineering, solvent casting, micropatterning techniques, electrospinning and combinatorial techniques. AM techniques, that are preferred today, are: extrusion-based processes, inkjet printing, vat photopolymerization and laser-assisted bioprinting. Direct printing processes bring to the creation of the capillary with coaxial nozzle and bioink, without waste of material; while, indirect printing processes bring to a component with a sacrificial or fugitive material that is then removed in order to create the channel. Combinatorial processes also exist.

For micro biomedical applications some post-treatments should be taken into account [54]. Surface modification can be chemical or physical and its aim is the creation of a morphology able to provide adequate properties to the material when required. At the micro scale is not an easy procedure, because of the reduced surfaces to be treated. Another issue for biomedical implants is FBR, that means Foreign Body Response and it refers to the inflammation process subsequent to implantation. Additionally, pitting and fretting corrosion can deteriorate the components acting in harsh environment.

8.2. GENERALITIES

The pacemaker is an electronic device that stimulates the cardiac tissue when the heart of the patient is not able to work properly [55, 56]. Its main parts are: battery, generator and leads with electrodes. The leads connect the generator to the heart and the battery gives energy to the generator. Circuits and battery, which is usually in lithium, are located in a titanium cage.

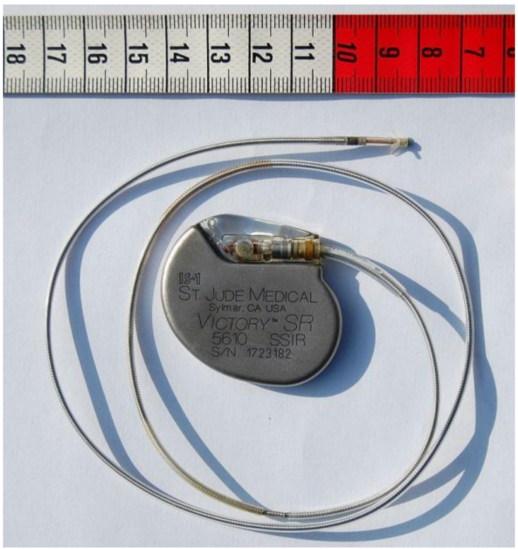

Figure 8.1. *Pacemaker with leads [55]*

The triggered pacemaker produces impulses for the ventricle in function of the activity of the atrium of the heart; while the autonomous pacemaker produces impulses with a fixed frequency. In the triggered pacemaker, electrodes register the cardiac activity and through the leads send information to the processor located in the generator. When activity is unstable, the processor enables the generator to give electrical impulses to the heart through one, two or three leads, that reach the cavities of the heart through veins. Electrodes can be bipolar (cathode and anode internal to the heart) or monopolar (cathode internal to the heart and anode in the metallic cage of the pacemaker).

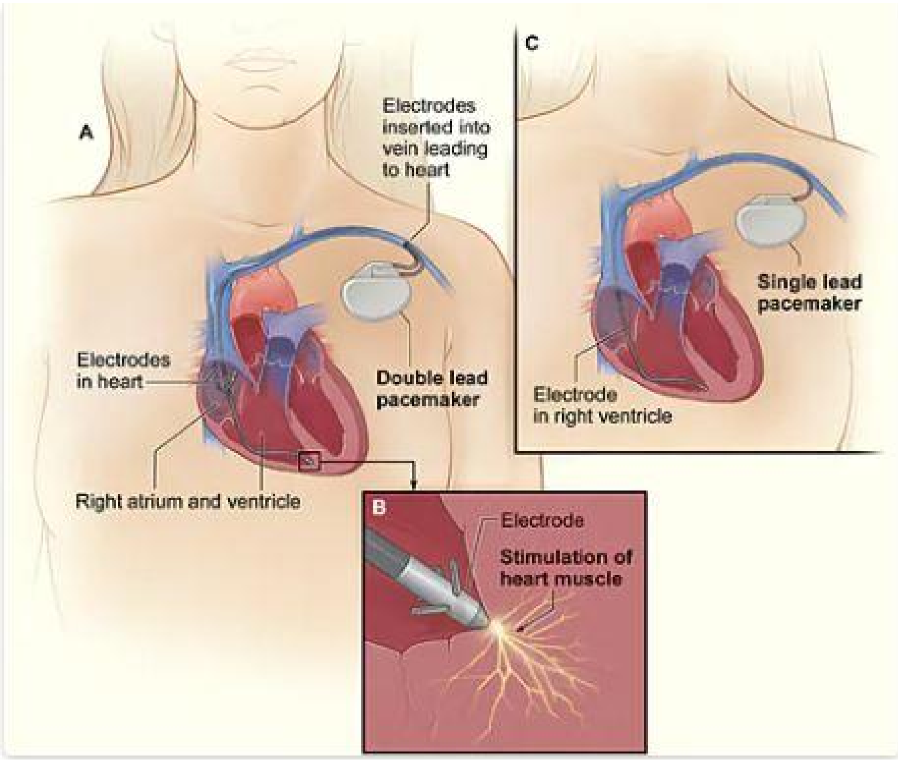

Figure 8.2. *Scheme of an implanted pacemaker with its working principle [56]*

The main risks correlated to the use of pacemakers are [57]:

- cardiac perforation;
- hematoma;
- allergic reaction;
- pulmonary collapse;
- lead dislodgment;
- pocket pain;
- lead fracture;
- lead insulation failure;
- infections.

Recent pacemakers are leadless: the whole device is located inside a capsule clamped to the internal wall of the heart. This modern concept is less invasive, because it does not need a subcutaneous pocket and it is free from possible damages to the leads and consequently to the human body. Nowadays, on the market, it is possible to find two efficient leadless pacemakers: Nanostim Pacemaker (LCP) and Micra Transcatheter Pacemaker (TPS) [58-60].

Figure 8.3. *Nanostim and Micra pacemakers [58]*

Both can present dislodgment of the device and cause perforation of the cardiac tissue. They differ in dimensions, in the way they are attached to the myocardium and in the type of rate response sensor. Micra is smaller and lighter, but its battery has got a shorter life in respect to Nanostim. In table 8.2, the main parameters of the two pacemakers are listed. They are collected according to the fixed programming (ISO 14708) standard guidelines: 2.5 V, 0.4 ms, 600 Ohm, 60 beats/min, and 100% pacing.

Table 8.2. *Parameters of LCP and TPS [58-60]*

	Nanostim Pacemaker (LCP)	Micra Transcatheter Pacemaker (TPS)
Company	St. Jude Medical	Medtronic Inc.
Length [mm]	41.4	25.9
Width [mm]	5.99	6.7
Volume [cm^3]	1	0.8
Weight [g]	2	2
Primary fixation mechanism	Screw-in helix	Self-expanding nitinol tines
Secondary fixation mechanism	Self-expanding nylon tines	Absent
Pacing mode	VVI/VVIR	VVI/VVIR
Sensor	Blood temperature	3- axis accelerometer
Battery	Lithium-carbon mono-fluoride	Lithium silver vanadium oxide/carbon mono-fluoride
Battery life [years]	9.8 (2.5 V @ 0.4 ms) or 14.7 (1.5 V @ 0.24 ms)	4.7 (2.5 V @ 0.4 ms) or 10 (1.5 V @ 0.24 ms)
Threshold at implant	0.82 V @ 0.4 ms	0.63 V @ 0.24 ms
Threshold after 6 months	0.53 V @ 0.4 ms	0.54 V @ 0.24 ms
Implant success	95.8%	99.2%

The project proposes a new concept of leadless pacemaker able theoretically to increase its lifetime and to reduce costs, occupied space and risks. It consists on the production at micro scale of a piezoelectric-based energy vibration harvesting system that stores energy taking it from the vibrations of the heart and giving it to sensors and actuators of the pacemaker. The energy harvester in the pacemaker can avoid the presence of the battery, or at least it can reduce its importance, with all battery correlated risks and discomforts. In fact, the main reason for replacement of the pacemaker is the substitution of the battery, if children, that require more substitutions because of the continuous growing of their organs, are not considered. A prolongation of the battery life until 30 years or the substitution with an energy harvester can save money in medical field because there would be less operations for substitution and a consequent decreasing number of complications during surgery. Moreover, waiting lists for patients would be faster.

The problem in miniaturizing the device is overcome through two possible approaches [61]:

1. develop a high power density macro sized device and then miniaturize it;
2. develop a miniaturized device and then enhance its power density.

The second approach is preferred because if in the end the power density is not high enough, a battery can solve the problem, while if the device is still too big, it is not suitable for the application. In other words, space requirement is more stringent than power requirement.

The energy harvester can be applied directly to the cardiac tissue in order to have simple excitations of the harvester that gets strained, thus producing electric charge. Another solution consists in embedding the harvester inside the pacemaker, not directly in contact with the cardiac tissue, together with the wafer with electronic circuit and the battery. In this way, space is spared and the whole device is insulated making the device less risky for the human health and possible operations for substitution easier. Moreover, the risk connected to a deterioration of the component because of the harsh environment is completely avoided.

In order to create an efficient energy harvester, many design criteria are to be taken into account. First of all, it is necessary to choose the appropriate shape of the main components of the harvester with the definition of the principle of working, that is the piezoelectric concept. Secondly, materials of the components must be chosen. Thirdly, a production process must be identified. Fourthly, dimensions of the device should be appropriately tuned in order to get particular working conditions, being careful of the imposed boundary conditions, such as the available restricted space and weight. Fifthly, the materials involved in the motion of the micro system and chosen for this particular application must be resistant against static rupture and high cycle fatigue and compatible with the other elements of the device.

The concept of working for an energy harvester is based on the behavior of the piezoelectric material: if it gets strained, it produces voltage and electric charge in a reversible process. The electrical energy can be stored in a battery or directly given to the elements that act as pacemaker cells. Hence, in order to work properly, the energy harvester will face a deformation of its elements. As first step, it can be deduced that in order to store more energy, the vibrating piezoelectric component must be designed with its resonance frequency coinciding with the frequency of the dynamic load, that in this case is given by the heartbeats that have got a frequency of 1 Hz in normal conditions, i.e. 60 heartbeats per minute.

In literature, there are already some attempts in creating piezoelectric-based energy harvesting systems for pacemakers. Piezoelectric bimorph beams in a "fan-folded" design have already been studied and they were resonant between 0 and 200 Hz occupying only 2.5 cm^2 and delivering 100 μW of power. In this project, the first observation was that the frequency of the heartbeats is low and the only way to make the structure resonant was to increase the whole length of the system connecting several beams together. A very large mass was put at the end of the beams to enhance vibrations. Flexible piezoelectric nanogenerators with thin films in PMNPT have also been studied and they could provide 8 V and 0.22 mA. It must be underlined that these works were not at micro scale.

The project, proposes as initial target for the specific power generation per unit surface 50 μW/cm^2 to assure a high energy conversion. For a better comprehension, it is to be stressed that modern pacemakers can work properly with a low level of energy (1 millionth of a Watt) per heartbeat [66]. Generally, the main problem in designing such a device is connected to the layout itself, that implies some requirements to the material, that appears in thin and flexible layers: the piezoelectric material must have high electromechanical coupling and low brittleness, it must be lead-free and light. The thickness of the piezoelectric layers is an important parameter of design, because the layer must be thick enough in order to have a sufficient mechanical strength, but it must be also thin enough in order to vibrate. The main problem regarding the design steps will be the miniaturization of the system that requires a resonance vibration range at low frequency, because shape and dimensions must be suitably tuned. This affects also the production steps, because a technology able to create this micro device must be identified. In order to save room, a plane layout for the harvester is chosen, showing out of plane bending motion of its beams, that act as support for the two piezoelectric layers, that are covered with the electrodes whose thickness is negligible in respect to the other elements, even if at micro scale is currently difficult identifying some dimensions negligible in respect to others. The configuration with two piezoelectric layers per supporting beam is called bimorph, hence the system composed by the supporting beam and the two piezoelectric layers can be defined as bimorph beam. The electrical connection between the layers can be either in series or in parallel [62-64]. This depends on the poling directions of the piezoelectric layers and on how the electrode leads are arranged. The project proposes at the moment a parallel connection of the circuits, but electronic engineers will improve this aspect of the device in a subsequent revision of the work.

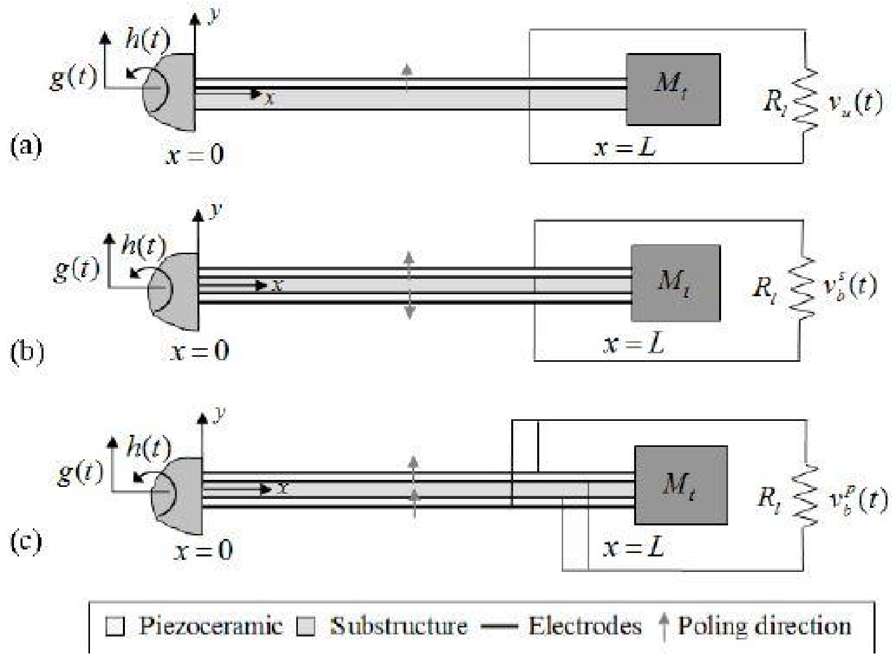

Figure 8.4. *Sketches of the possible layouts: unimorph (a), bimorph with series connection (b) and bimorph with parallel connection (c) [64]*

The design of electric circuitry will be defined by electronic engineers once the harvesting device is designed. Verification and validation on prototypes will be performed to evaluate the real behavior of the device, under the supervision of a medical staff, that will study the possible problems of a rechargeable pacemaker: damages to the nervous system, lead insulation failure, lead fracture, heating and subsequent power loss, inflammation and infection of organic tissues [60, 66].

It is already well known that the production at micro scale of piezoelectric layers has still high costs in respect to the actual price of a pacemaker (i.e. from 8000 to 12000 €) and hence it is not suitable for mass production, but a project of this type can be useful also in the future, when production of this smart materials will have lower costs.

Concerning the mechanical aspect, which is the central point of this thesis, the beams have got a triangular shape if seen from the top or the bottom view. This is a choice that allows to spare material, because it is well known that the utilization factor for rectangular beams is 1/9 and for triangular beams is 1/3. This means that the triangular beam stores energy three times more efficiently than the rectangular beam. A second advantage is subsequent to this choice: under bending moment, the stress will be uniform along the beam and equal to the maximum value. This is good for calculations involving the energy conversion from the mechanical field to the electrical field. In reality, the shape of the beam is not triangular, but trapezoidal, with the shorter basis length tending to zero and negligible with respect to the longer basis length: the triangular shape is an approximation that simplifies the calculations for the reliability of the device and that in the real world would not have got practical applications because of the difficulties in applying loads on the tip of the triangular beam. In order to save room, a circular frame will bond together all the larger sides of the beams and at the free tips of the beams, located at the center of the circular frame, a tuning mass is connected, thus enhancing vibrations and hence energy conversion. Figure 8.5 shows the qualitative shape of the device.

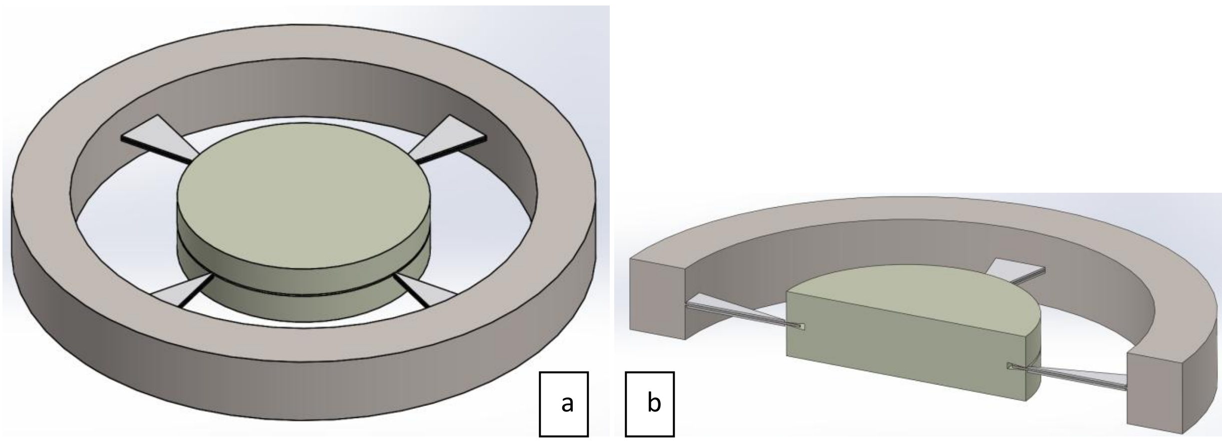

Figure 8.5. *Qualitative shape of the Energy harvester system: three dimensional view (a) and sectioned three dimensional view (b)*

The harvester is packaged inside the pacemaker with electronic circuits and battery in order to avoid corrosion of the device and health problems to the patient connected to possible infections due to contact with medical implants. In order to leave sufficient space for the other elements, the harvesting system should occupy the 75% of the internal space of the pacemaker. This is not a problem for the design steps because the system is miniaturized and in respect to existing pacemakers, space near the energy harvester will be considerable. Anyway, a height of 1.3 mm for the tip mass will be considered as boundary condition.

For this application, the excitation frequency is unfortunately not precisely known, being the heartbeat not constant in time and not sinusoidal (sinusoidal harvesters are generally more performing). Designing the device to make it resonant in a range of frequency and not in a single value of frequency can be a solution to exploit more than one of the possible frequencies of the heartbeat. Another possible solution, that is the chosen one for this project, is to consider an off resonance excitation method based on the shock-induced impulse from the heartbeat [61]. In fact, in the specific environment, the only force that is strongly felt by the device is the force coming from the vibration of the heart (all the other forces are negligible) and this force has got an impulsive nature. The impulse (high acceleration in a small period of time) forces the harvester to operate at its resonant frequency, even if the resonant frequency of the device is not coincident with the main frequency of the heartbeats, i.e. 1 Hz. This is a key point for designing the harvester, because if the targeted resonant frequency for the beams was 1 Hz, it was too difficult to find a solution at micro scale: the beam would be too much long and too much thin and the tip mass would be too much big. According to [61], the acceleration imparted by the heart wall and used for designing pacemakers is 2 g.

An observation is needed: the pacemaker capsule must be located by the cardiologists in the correct position and orientation inside the heart, thus avoiding discrepancies between the way the harvester is supposed to act and the way it acts. This is an important final step for the correct working of the component, because the heart wall causes forces in all three directions with a prevalent one and confusion among the three directions can cause serious problems.

In order to assure that the device does not break statically, the gravitational force with an acceleration of 1 g is taken into account, thus evaluating if the bimorph beams are able to bear the weight of the tip mass. The, the dynamic analysis is performed and 2 g is taken as acceleration value. Considering that the heartbeats are continuous and hence the harvester is continuously deformed according to its own resonant frequency, the fatigue analysis is performed for establishing the life of the device.

Assumptions in the motion of the beams must be taken into account. During the bending moment, the plane sections of the beams remain plane and the effects of rotary inertia and shear deformation are negligible. These assumptions can be made on the basis that the beams are thin in respect to their length.

8.3. CHOICE OF THE MATERIALS

Before proceeding with the calculations for the design, it is necessary to choose the material of every component of the device: the circular supporting frame, the tip mass, the electrodes, the supporting beams, the piezoelectric layers and the thin bonding layers between supporting beams and piezoelectric layers.

All the materials should be lead-free, because biocompatibility is an important requirement, even if the harvester is totally embedded and insulated inside the pacemaker capsule. Additionally, they should not be magnetic, because the patient could face a magnetic resonance imaging (MRI).

The function of the tip mass is simply to enhance the vibrations of the beams and the main constraint for the choice of the material is given by the restricted allowable space. High density is therefore required for the tip mass and tungsten seems to be the most reasonable material.

The electrodes will be made in aluminum, being this material already used for many biomedical applications.

For the supporting beams a metallic material is chosen: the titanium alloy Ti-6Al-4V, also called grade 5. Its main advantages are the high mechanical properties also against fatigue and the high processability in additive manufacturing as many articles in literature can testify. The circular supporting frame, for simplicity, is made in the same material of the supporting beams, being de facto these components only one component. Bimorph beams or supporting metallic beams identify from now only the parts supporting the piezoelectric layers and not the circular frame.

The bonding layers have the triple function of attaching the different components of the device, of damping the possible shear effects between them and of separating their answers to heating. In fact, the materials could have different thermal dilatation coefficients and adhesion could cause problems during working. The material chosen is conductive epoxy (filled with Ag nanoparticles), because it is widely used in additive manufacturing with many examples in literature and it seems to be suitable to be applied in order to attach the piezoelectric layers to the metallic supporting beams. In the design thin bonding layers are not considered, because their thickness is negligible in respect to the other dimensions.

The piezoelectric layers will be made in gallium oxide-doped BCTZ, more precisely 0.08wt%Ga_2O_3-doped $(Ba_{0.99}Ca_{0.01})(Ti_{0.98}Zr_{0.02})O_3$ [67]. It must be underlined that gallium oxide is biocompatible and not toxic, as some biomedical applications involving it testify; however, if it gets in contact with eyes, skin and lungs in great quantity, it can cause inflammation. Anyway, this is not the case, because it is inserted in the BCTZ matrix in small quantity and there is no danger it gets dispersed from the piezoelectric material. Its function is only to increase the processability of the material without reducing the piezoelectric properties.

BCTZ is a solid solution with a single phase perovskite structure and a piezoceramic with the outstanding piezoelectric coefficient $d_{33} = 650\ pC/N$ if it gets calcined at 1300 °C and sintered at 1540 °C. This sintering temperature is unfortunately too high for a low consumption of energy during production penalizing the mass production that is required for this application. Many researchers studied the possibility of doping the material with metal oxides in order to decrease the sintering temperature without penalizing the piezoelectric properties of BCTZ. A preliminary comparison among all the possible additives and their effects on BCTZ is performed by Ting Zheng et al. (2018) [65], that shows the many possible integrations with doping.

As shown by Jiafeng Ma et al. (2013) [67], with the small weight percentage of 0.08, gallium oxide is able to decrease the sintering temperature to 1350 °C and, contrariwise to many other additives, allows also to keep the Curie temperature almost at its standard value: it is decreased only from 120 to 115 °C. This is good because a high Curie temperature implies that increasing temperature the deterioration of the main properties of the material is postponed, widening the temperature stability range, as figure 8.6 shows.

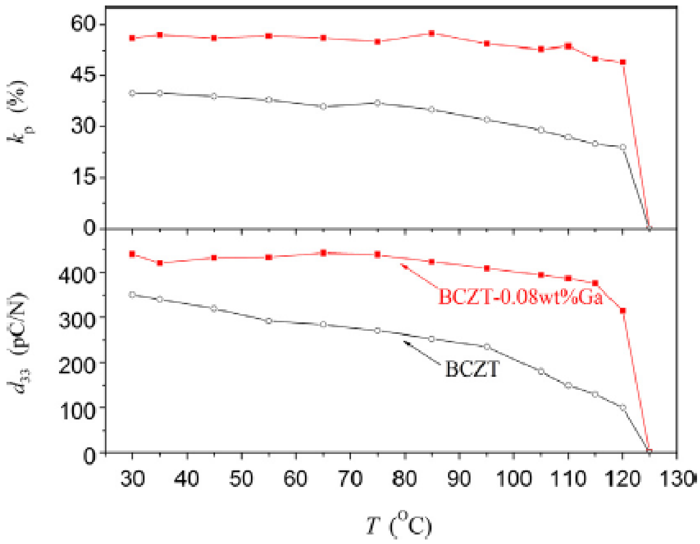

Figure 8.6. *The planar electromechanical coupling factor and the piezoelectric coefficient as a function of temperature: the stable temperature range is wide before the deteriorating of the piezoelectric properties [67]*

Attention is given to the preparation of the powder of Ga_2O_3-doped BCTZ, because it is the key material in the harvesting device of the particular application studied in the project. The process can be simply the conventional solid-state method. Raw materials of $BaCO_3$, $CaCO_3$, ZrO_2, and TiO_2 are milled in alcohol using ZrO_2 balls for 24 hours. After this, the calcination process occurs at 1250 °C for 4 hours. Increasing the calcination temperature (reasonable values range from 1000 to 1300 °C) has got the effect of increasing the volume density of BCTZ, the electromechanical coupling factor, the dielectric constant, the dielectric loss, the piezoelectric coefficient and, if the sintering temperature is not too much high, the quality factor [68]. Subsequently, Ga_2O_3 powder is added in the appropriate percentage. Another ball-milling is performed for 12 hours before drying process that brings to micro sized particles of the final powder, obtained only after a mixing with PVA.

Considering 1350 °C as sintering temperature, increasing the content of gallium oxide gives positive effects to the piezoelectric coefficient and the electromechanical coupling factor until the weight percentage of the additive is 0.08. The mechanical quality factor, increases as gallium oxide content increases because the partial substitution of $(Zr, Ti)^{4+}$ by Ga^{3+} generates oxygen vacancies, pinning the motion of the ferroelectric domain walls. The reached values for the mechanical quality factor and the piezoelectric coefficient ($440\ pC/N$) at 0.08wt%Ga_2O_3 are not high as for BCTZ, but this is the price to pay in order to decrease the sintering temperature. On the other hand, the electromechanical coupling factor is 56%, hence comparable to the one of BCTZ.

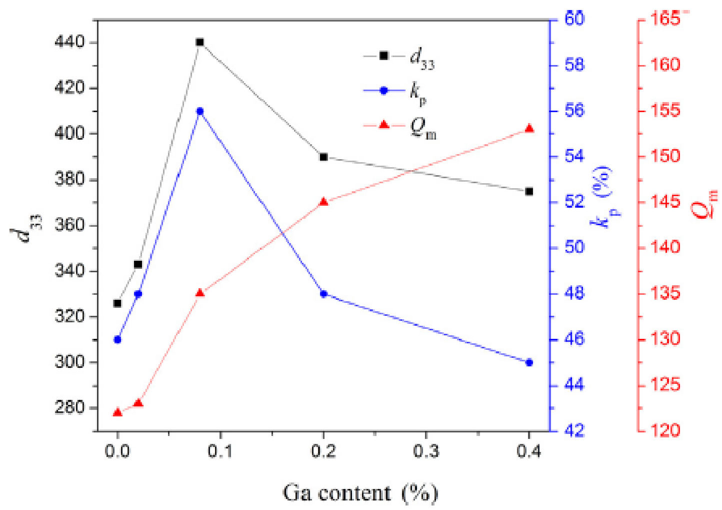

Figure 8.7. *Piezoelectric properties as functions of Ga_2O_3 content [67]*

It is needed to underline that in [67] the previous image contains a mistake (the abscissa should be “Ga_2O_3 content wt%”) and that tested specimen are not prepared by additive manufacturing, but the work can give an idea of the reachable values in the piezoelectric properties with gallium oxide doping.

8.4. CHOICE OF THE TECHNOLOGY

The additive manufacturing chosen in order to produce the energy harvester is the selective laser sintering. This technology presents many advantages, because it is a fast production method for geometrically complex and end usable parts with high strength, stiffness, chemical stability and durability. The main disadvantage is the porosity presented by the printed components that can reduce fatigue life.

There is a wide plethora of printable materials: metals, ceramics and polymers. In fact, in literature there are many examples about the printability by SLS of the materials present in this energy harvester. Moreover, the process can create micro scale components. However, to reach such a small dimension for the thickness of the components, the technology needs further developments. Additionally, a SLS machine able to print in one step many different materials does not exist yet. A future improvement, in order to allow fast production of the whole energy harvester, could be the integration around the build platform of the machine of different powder feed suppliers, different lasers and a ventilation system. In this way, when there is the micro step of the build piston in the vertical direction, powder of only one material is distributed on the platform and sintered. Subsequently, the ventilation system eliminates the residual not sintered powder from the build platform and the powder of the next material can be distributed and sintered by the specific laser with the required power. The procedure is repeated for every material present in the horizontal layer and then the next vertical micro step of the build piston can be done. This procedure is repeated until the part is totally created.

It is not known if this technology is feasible, but in future with continuous further studies, it can not be excluded that such a detailed machine can be presented on the market.

8.5. DESIGN STEPS

A premise is needed: because of the difficulty in finding in literature many data regarding the particular material used for the piezoelectric layers of the harvester, reasonable assumptions on the values are taken, considering also the possible effects that a micro additive manufacturing process can present. In table 8.3, the collected data of the two materials are listed.

Table 8.3. *Technical data for gallium oxide-doped BCTZ (subscript "p") and Ti-6Al-4V (subscript "s") fabricated by SLS*

Rm_p	$850\ MPa$
Rm_s	$1250\ MPa$
Ry_s	$820\ MPa$
E_p	$200\ GPa$
E_s	$105\ GPa$

The design of the energy harvester is optimized by an iterative procedure aimed at finding acceptable dimensions and energy conversion. Input data are the weight of the tip mass, length, height and base of the triangular cantilever for the ceramic piezoelectric parts and for the metallic supporting parts. These dimensions are related also to the number of supporting cantilevers, another input data. In table 8.4, the optimal values after iteration are listed:

Table 8.4. *Optimal values for the tip mass weight, base, height, length of the triangular piezoelectric layers (subscript “p”) and of the triangular metallic support layers (subscript “s”) and for the number of supports.*

$m_{beam} = 0.04\ g$
$b_p = 500\ \mu m$
$h_p = 20\ \mu m$
$l_p = 1500\ \mu m$
$b_s = 500\ \mu m$
$h_s = 20\ \mu m$
$l_s = 1500\ \mu m$
$num_{sup} = 3$

The first step of calculation is aimed at finding the maximum weight of the tip mass that the bimorph beam is able to bear statically.

The area moments of inertia of the piezoelectric and of the metallic parts are:

$$I_p = \frac{b_p h_p^3}{12} + b_p h_p \left(\frac{h_p + h_s}{2}\right)^2 = 4.33 \cdot 10^{-6}\ mm^4 \tag{8.1}$$

$$I_s = \frac{b_s h_s^3}{12} = 3.33 \cdot 10^{-7}\ mm^4 \tag{8.2}$$

The flexural stiffness for the piezoelectric layer and for the supporting metallic beam can be calculated as:

$$k_p = \frac{2E_p I_p}{l_p^3} = 5.14 \cdot 10^{-1}\ N/mm \tag{8.3}$$

$$k_s = \frac{2E_s I_s}{l_s^3} = 2.07 \cdot 10^{-2}\ N/mm \tag{8.4}$$

The bimorph beam is composed by the metallic support and the two piezoelectric layers: all these elements are mechanically connected in parallel, because the sum their flexural stiffness in order to bear the force and they face the same displacement being attached one to the others.

Therefore, the equivalent flexural stiffness of each bimorph beam is:

$$k_{eq} = 2k_p + k_s = 1.05\ N/mm \tag{8.5}$$

For the application, a safety factor S_f equal to 9 is chosen: the maximum allowable stress that the elements can face without showing fracture or yielding are:

$$\sigma_{p_{all}} = \frac{Rm_p}{S_f} = 94.4\ MPa \tag{8.6}$$

$$\sigma_{s_{all}} = \frac{Ry_s}{S_f} = 91.1\ MPa \tag{8.7}$$

Now, it is possible to calculate the force that generates the maximum allowable stress:

$$F_{p_{all}} = \frac{\sigma_{p_{all}} \cdot I_p}{l_p \cdot \left(\frac{h_s}{2} + h_p\right)} = 9.09 \cdot 10^{-3}\ N \tag{8.8}$$

$$F_{s_{all}} = \frac{\sigma_{s_{all}} \cdot I_s}{l_s \cdot \frac{h_s}{2}} = 2.02 \cdot 10^{-3}\ N \tag{8.9}$$

The total force generated by the gravitationally accelerated mass on the bimorph beam is:

$$F_{max_{all}} = 2F_{p_{all}} + F_{s_{all}} = 2.02 \cdot 10^{-2}\ N \tag{8.10}$$

The maximum allowable weight of the tip mass per bimorph beam can be determined as:

$$m_{max_{all}} = \frac{F_{max_{all}}}{g} = 2.06\ g \tag{8.11}$$

The tip mass vertical displacement is:

$$f_{max_{all}} = \frac{F_{max_{all}}}{k_{eq}} = 19\ \mu m \tag{8.12}$$

This value underlines the absence of normal tension in the piezoelectric layer, because for the Pythagorean theorem the vertical displacement does not make the structure elongate.

Knowing that the dynamic condition is more dangerous for the device, a lower value of the tip mass weight per bimorph beam (0.04 g) is chosen for the dynamic iteration steps. In this way, the device is surely able to bear statically the stress generated by the gravitational acceleration.

The total tip mass, considering the presence of three bimorph beams, results:

$$m_{tot} = m_{beam} \cdot num_{sup} = 0.12\ g \tag{8.13}$$

The tip mass is big in respect to the mass of the bimorph beams, making this latter negligible. It must be reasonably lighter than 1 gram to be easily located in already existing pacemakers such as Nanostim Pacemaker, although piezoelectric energy harvesters for pacemakers with a tip mass of more than 18 grams have been already presented. Moreover, a difficulty is to concentrate the tip mass in such a small available space. Considering the density of tungsten, i. e. 0.0193 g/mm^3, the volume occupied by the tip mass is:

$$V = \frac{m_{tot}}{\delta} = 6.22\ mm^3 \tag{8.14}$$

Considering the total dimensions of Nanostim Pacemaker, whose global width is 5.99 mm, it can be reasonably deduced that the allowable external diameter of the circular frame, that will be clamped in the internal wall of the pacemaker, is 5.8 mm. With a thickness of the circular frame equal to 0.1 mm, the diameter of the cylindrical-shaped tip mass can be detected easily by the SolidWorks 3D model: it turns out to be $d = 2.56\ mm$.

The constraint coming from the maximum limit for the tip mass height $h_{mass} = 1.3\ mm$, is therefore respected, because there is coherence between the volume occupied by the tip mass, its weight and its density. More precisely, the height of the tip mass will be:

$$h_{mass} = \frac{V}{\pi \cdot \left(\frac{d}{2}\right)^2} = 1.19\ mm \tag{8.15}$$

Now, it is possible to calculate the natural pulsation of each bimorph beam as:

$$\omega_{nat} = \sqrt{\frac{k_{eq}}{m_{beam}}} = 5118\ rad/s \tag{8.16}$$

This corresponds to:

$$f_{nat} = \frac{\omega_{nat}}{2\pi} = 815\ Hz \tag{8.17}$$

The resonance pulsation is related to the natural pulsation:

$$\omega_{res} = \omega_{nat}\sqrt{1 - 2\xi^2} = 5106\ rad/s \tag{8.18}$$

This corresponds to:

$$f_{res} = \frac{\omega_{res}}{2\pi} = 813\ Hz \tag{8.19}$$

Where $\xi = 0.05$ is the damping ratio considered reasonable for the involved materials. The damping of the structure is mechanical and electrical and for the preliminary design the damping ratio can be assumed taking into account that a tuning of this value should be performed.

The mean force generated by the impulse of the heart wall can be expressed as:

$$F_0 = \frac{m_{beam}(v_f - v_0)}{\tau} = 7.85 \cdot 10^{-4}\ N \tag{8.20}$$

Where $\tau = 0.035\ s$ is the time interval of the impulse, $v_f = 2g\tau$ is the velocity of the tip mass imparted by the impulse that has got an acceleration equal to $2g$, v_0 is the initial velocity of the tip mass that is equal to zero, because with the assumed damping value, the oscillations of the harvester end before the subsequent impulse is performed.

The force coming from the impulse generates a vertical displacement of the tip mass:

$$f_0 = \frac{F_0}{k_{eq}\sqrt{(1-r^2)^2+(2\xi r)^2}} = 7\ \mu m \tag{8.21}$$

Where $r = \frac{f_{res}}{f_{nat}}$ is the ratio between the resonant frequency at which the harvester is forced to vibrate because of the shock-impulse of the heart and the natural frequency.

The force applied to the tip of the cantilever beam is due to the heartbeat that moves the circular frame and it is assumed to be transmitted without losses from the heart, to the circular frame and finally to the tip mass. The force is distributed to the components of the composed beam:

$$F_p = f_0 \cdot k_p \cdot \sqrt{(1-r^2)^2+(2\xi r)^2} = 3.85 \cdot 10^{-4}\ N \tag{8.22}$$

$$F_s = f_0 \cdot k_s \cdot \sqrt{(1-r^2)^2+(2\xi r)^2} = 1.55 \cdot 10^{-5}\ N \tag{8.23}$$

The forces generate constant stress along the piezoelectric layers and the metallic supporting beam:

$$\sigma_p = \frac{F_p \cdot l_p}{I_p} \cdot \left(h_p + \frac{h_s}{2}\right) = 3.99\ MPa \tag{8.24}$$

$$\sigma_s = \frac{F_s \cdot l_s}{I_s} \cdot \frac{h_s}{2} = 6.99 \cdot 10^{-1}\ MPa \tag{8.25}$$

The moment experienced by the piezoelectric layer can be calculated as:

$$M = F_p l_p = 5.77 \cdot 10^{-4}\ Nmm \tag{8.26}$$

The energy of deformation for small displacements and elastic behaviour depends on the moment and it is:

$$E_{def} = \frac{l_p M^2}{6 E_p I_p} = 9.60 \cdot 10^{-8}\ mJ \tag{8.27}$$

The bimorph beams oscillate according to their resonant frequencies because the exciting force is an impulse and hence the energy is stored in a time interval equal to:

$$\Delta t = \frac{T_{res}}{4} = 3.08 \cdot 10^{-4}\ s \tag{8.28}$$

Where $T_{res} = \frac{1}{f_{res}}$ is the period of the oscillation.

The mechanical power can be calculated as:

$$P_{mec} = \frac{E_{def}}{\Delta t} = 3.12 \cdot 10^{-4}\ mW \tag{8.29}$$

The total power, considering the number of cantilever beams and the fact that every metallic support is equipped with two piezoelectric layers, is:

$$P_{\substack{mec \\ tot}} = P_{mec} \cdot 2 \cdot num_{sup} = 1.87 \cdot 10^{-3}\ mW \tag{8.30}$$

The electromechanical planar coupling coefficient for BCTZ with oxide gallium is $k_P = 56\%$ (not to be confused with the flexural stiffness of the piezoelectric layer) and it is defined as the ratio between the mechanical energy accumulated and the electrical energy input or vice versa. Being 31 the flexural studied mode and evaluating the general relationship between k_P and k_{31}, a value of 30% for k_{31} is chosen. A ratio that involves two energies can be considered the same if it involves two powers, hence:

$$P_{\substack{el \\ tot}} = k_{31} P_{\substack{mec \\ tot}} = 5.62 \cdot 10^{-4}\ mW \tag{8.31}$$

This is the total electrical power that the bimorph beams generate every time they get deflected.

In order to give sufficient power for a single heartbeat, 1 millionth of a Watt is required. This amount of power is overcome by only two periods of deflection of the piezoelectric layers. The damping of the oscillating structures makes the oscillations smaller and smaller and there is also an electrical damping, but the power for a single heartbeat is guaranteed by the high number of oscillations between two subsequent heartbeats.

It remains to evaluate the high density power request. The total area of the piezoelectric layers from the top view is:

$$A = \frac{b_p l_p}{2} \cdot num_{sup} = 1.13 \cdot 10^{-2}\ cm^2 \tag{8.32}$$

The power density is therefore calculated as:

$$P_d = \frac{P_{el_{tot}}}{A} = 50\ \mu W/cm^2 \tag{8.33}$$

This value meets the requirement of the project. It must be underlined that the power requirements are respected with three bimorph beams, because if two beams do not work properly, there should be energy enough for the correct functioning of the device.

It is possible to evaluate also a power density considering the volume of the employed piezoelectric material:

$$P_{d_V} = \frac{P_{el_{tot}}}{V} = 7.49 \cdot 10^4\ \mu W/cm^3 \tag{8.34}$$

Where V is the volume occupied by the piezoelectric layers.

The elements experience a dynamic stress and hence it is important to evaluate the fatigue behaviour. The piezoelectric layer and the metallic supporting beam turns out to have got infinite life against fatigue, because stress is lower than the fatigue limits of the components, calculated as:

$$\sigma^C_{D-1_p} = \frac{C_S C_F C_L}{K_f} \sigma_{D-1_p} = 255\ MPa \tag{8.35}$$

$$\sigma^C_{D-1_s} = \frac{C_S C_F C_L}{K_f} \sigma_{D-1_s} = 350\ MPa \tag{8.36}$$

Where C_S is the scale factor and it is equal to 1 because of the reduced dimensions of the components, C_F is the roughness factor depending on the ultimate tensile strength of the material and on the surface roughness ($C_F = 0.70$ for the metallic support and $C_F = 0.75$ for the piezoelectric layer) and C_L is the load factor and it is equal to 1 for flexural excitations, K_f is the notch factor and it is equal to 1 because there are no notches and σ_{D-1} are the fatigue limits calculated as:

$$\underset{p}{\sigma_{D-1}} = 40\% \ \underset{p}{Rm} = 340\ MPa \tag{8.37}$$

$$\underset{s}{\sigma_{D-1}} = 40\% \ \underset{s}{Rm} = 500\ MPa \tag{8.38}$$

In fact, a higher safety factor and the influence of the still not well investigated micro dimensions of the components are considered choosing 40% of the flexural strength as the approximated fatigue limit for the metallic component instead of the 50% suggested by Bach criterion. The fracture due to fatigue, that is fragile, for ceramic components happens rarely, because the component does not present plastic behavior [69]. Many tests in real components have demonstrated that a higher limit of fatigue in respect to metallic materials can be considered, in fact 70% of the flexural strength seems to be a reasonable value. In order to take into account the micro scale of the component and to get a higher safety factor, 40% of the flexural strength is considered as the fatigue limit for the ceramic material.

The elements of the harvester are hence resistant against yielding, rupture and fatigue. Additionally, they meet the power and space requirements of the particular application.

8.6. EXPLANATION OF THE ITERATION

An explanation of the way of reasoning is here summarized. An initial theoretical design can be set with the limits constraints in space and in the technology chosen to fabricate the device. Usually, a μ-SLS machine is able to print 20 μm thick components as lower limit: the thickness of the piezoelectric layers and of the supporting beams is therefore set as 20 μm thick. However, it must be underlined that smaller features until 1 μm of thickness can be produced, for example using 100 nm size particle powders. The length of the bimorph beam is constrained, as explained before, by the internal wall of the capsule of the pacemaker. In order to allow a reasonable space for the tip mass, is can be deduced that the length of the beams could be 1800 μm. The basis of the triangular shaped cantilevers can be set equal to 600 μm, in order to make a sufficient stiff structure. The number of supports is initially set equal to 1 and the tip mass weight equal to 0.1 g.

The first thing that can be noticed is the low level of power per heartbeat, because although the target is reached, there is no sufficient safety factor for the operational condition, being all the power based on a single bimorph beam. If two bimorph beams are present, the tip mass would be excessive and it would be difficult to allocate it in the pacemaker. It is hence necessary to decrease the weight of the tip mass. This value is decreased until 0.5 g, i. e. until the power density reduces approaching its target.

At this point, it is possible to compact the design reducing the length and the basis of the triangular shaped bimorph beams until their final values. In this way, a further reduction of the tip mass is possible without penalizing excessively the power density. With a tip mass per bimorph beam equal to 0.04 g the power density of 50 μW/cm^2 is reached. In order to increase the power per heartbeat, three bimorph beams are designed: if 2 beams do not work properly, the target is still reached. This design is optimal because the space occupied by the total tip mass is at its limit, while the power density is guaranteed. Stress values in the supporting beam and in the piezoelectric layers are within the limits.

In table 8.5 the effects of the manipulation of the input data are summarized.

Table 8.5. *Main negative effects caused by a decreasing of an increasing of the input data. The listed effects are to be intended overcoming the limits if all the other not correlated parameters are kept constant.*

Parameter	**Decreasing**	**Increasing**
$m = 0.04\ g$	Decreased power density	Increased tip mass volume
$b_p = 500\ \mu m$	X	Decreased power density
$h_p = 20\ \mu m$	Not possible	Decreased power density
$l_p = 1500\ \mu m$	Decreased power density	Increased piezoelectric volume
$b_s = 500\ \mu m$	X	Decreased power density
$h_s = 20\ \mu m$	Not possible	Decreased power density
$l_s = 1500\ \mu m$	Decreased power density	Increased piezoelectric volume
$num_{sup} = 3$	Decreased power per heartbeat	Increased tip mass volume

It is to be observed that reducing b_s and consequently b_p (they are set to be equal), there are not apparent problems. However, no further decreasing in their values are chosen in order to keep a triangular-shaped bimorph beam configuration.

The final design is shown in the following images.

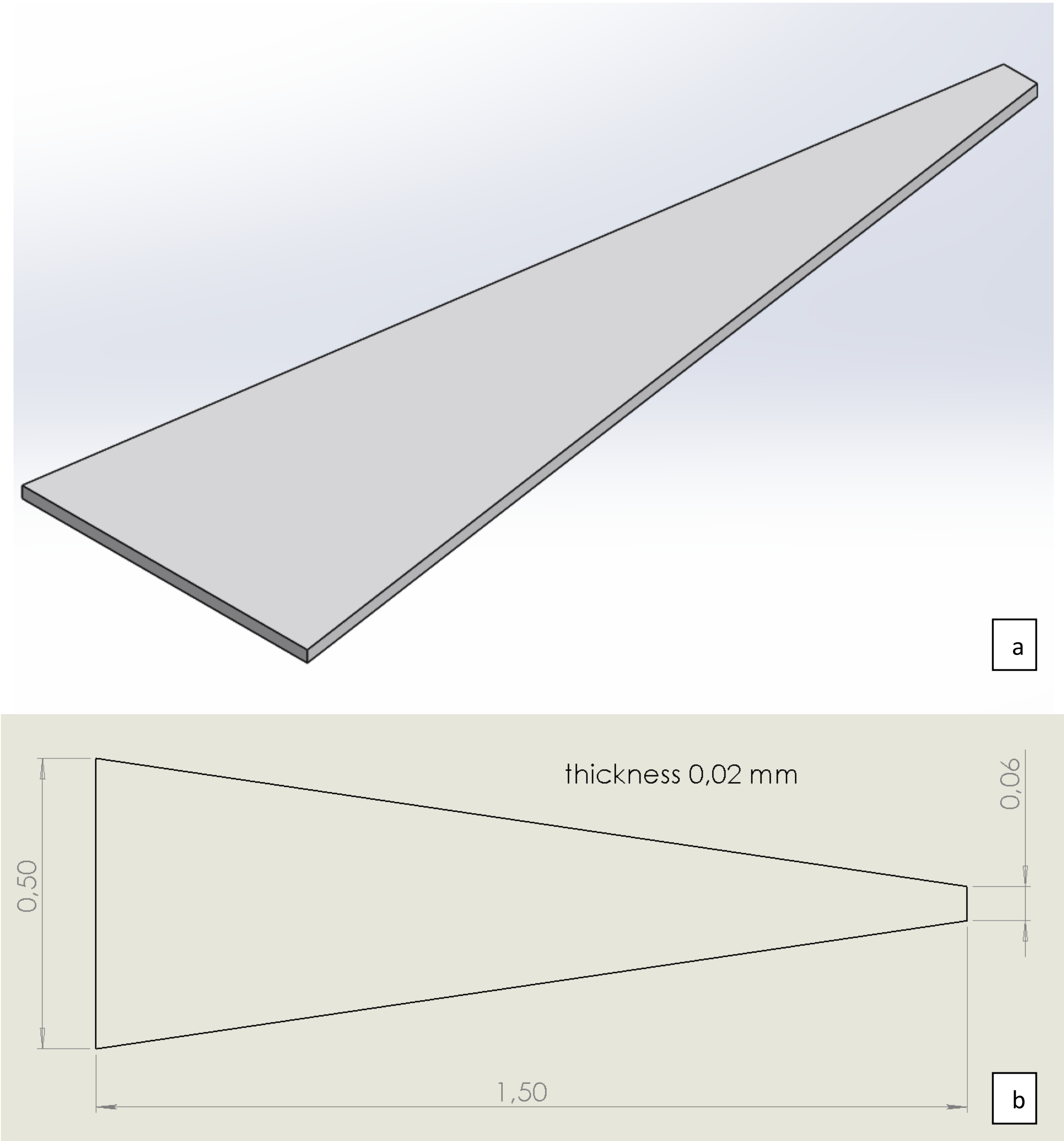

Figure 8.8. *Piezoelectric layer: three dimensional view (a) and technical design (b)*

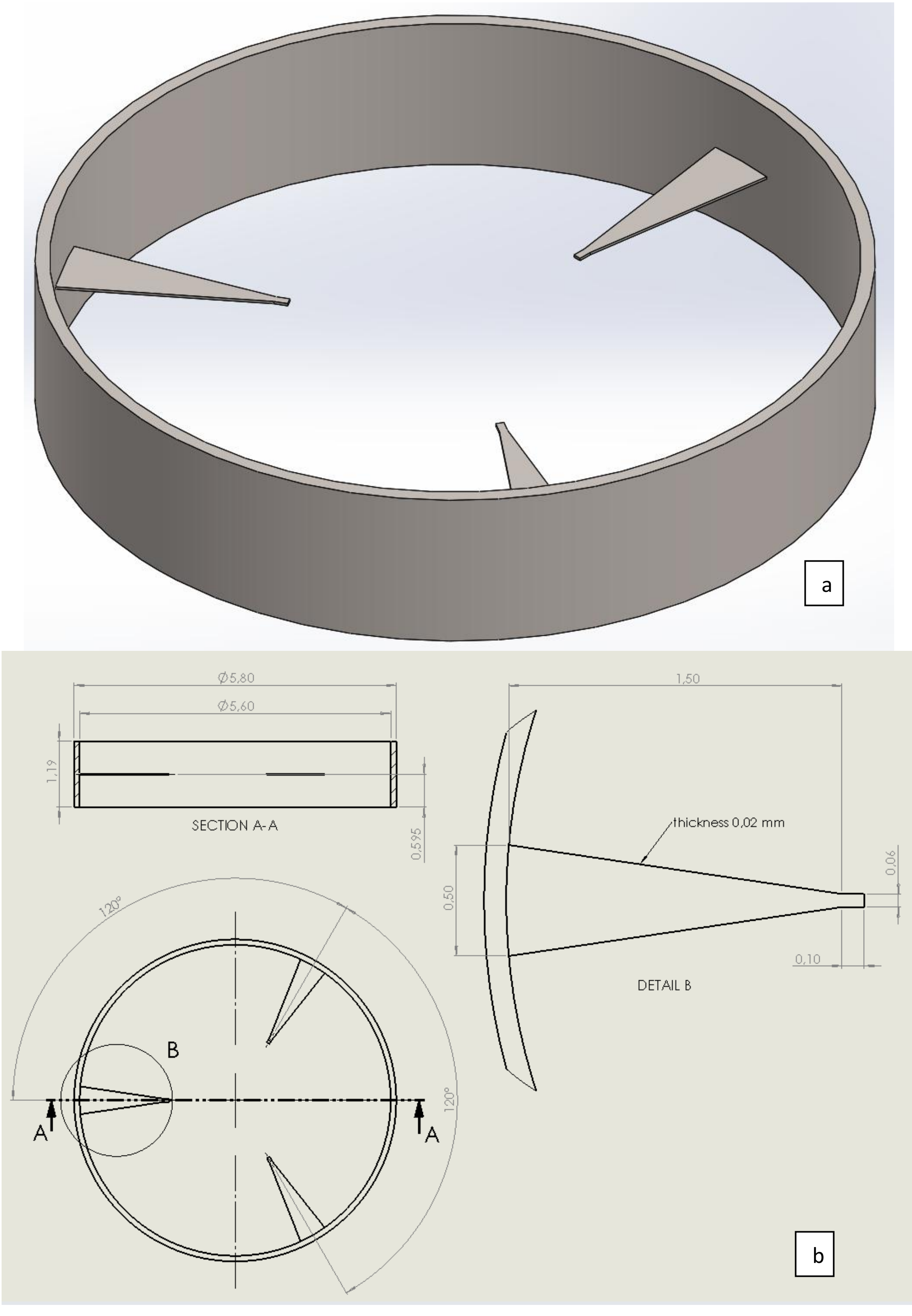

Figure 8.9. *Circular supporting frame with the supporting beams: three dimensional view (a) and technical design (b)*

As shown by figure 8.10, the particular profile is studied in order to make the bimorph beams deforming only under bending moment and avoiding stretches in the materials.

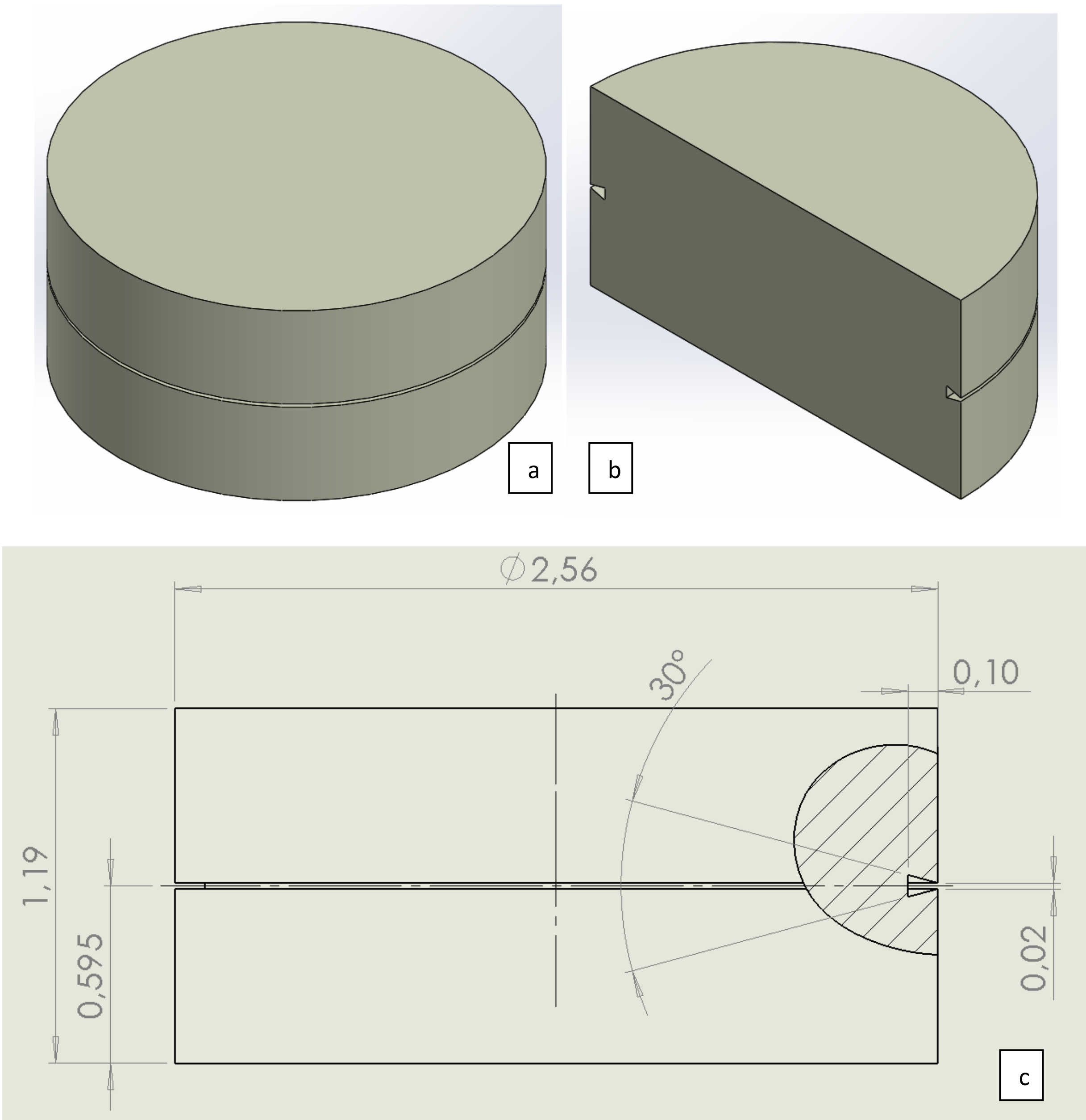

Figure 8.10. *Tip mass: three dimensional view (a), sectioned three dimensional view (b) and technical design (c)*

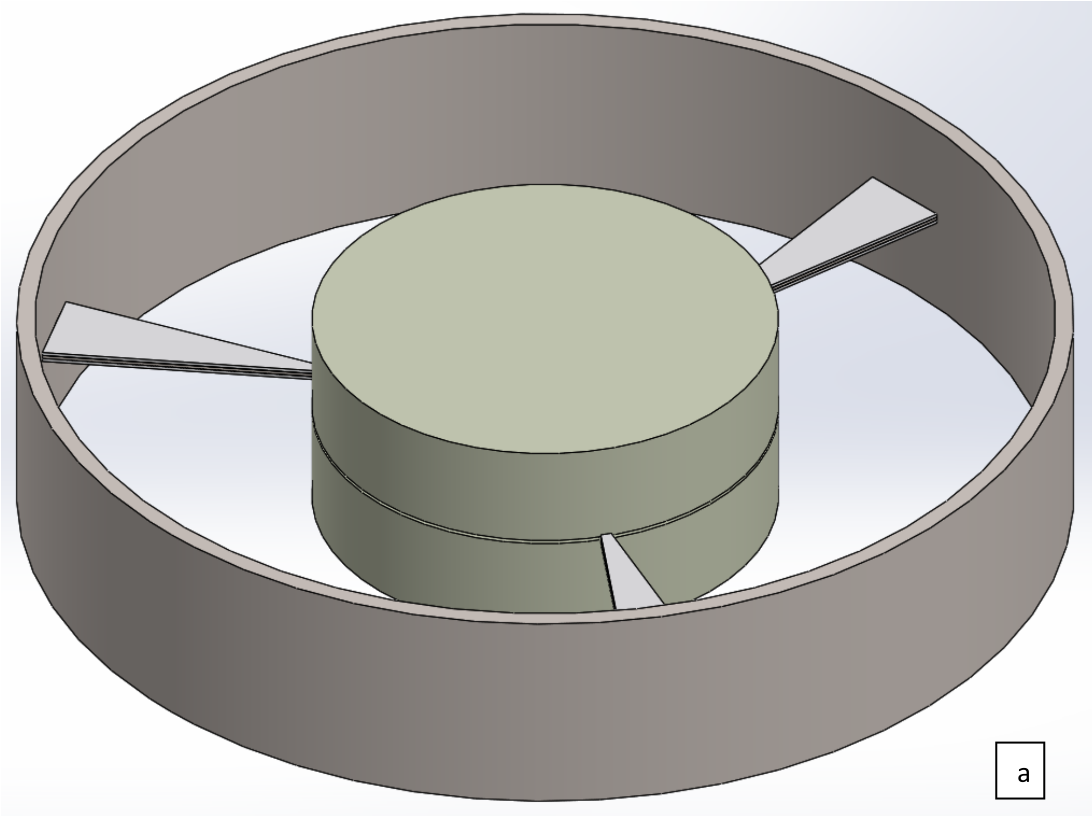
a

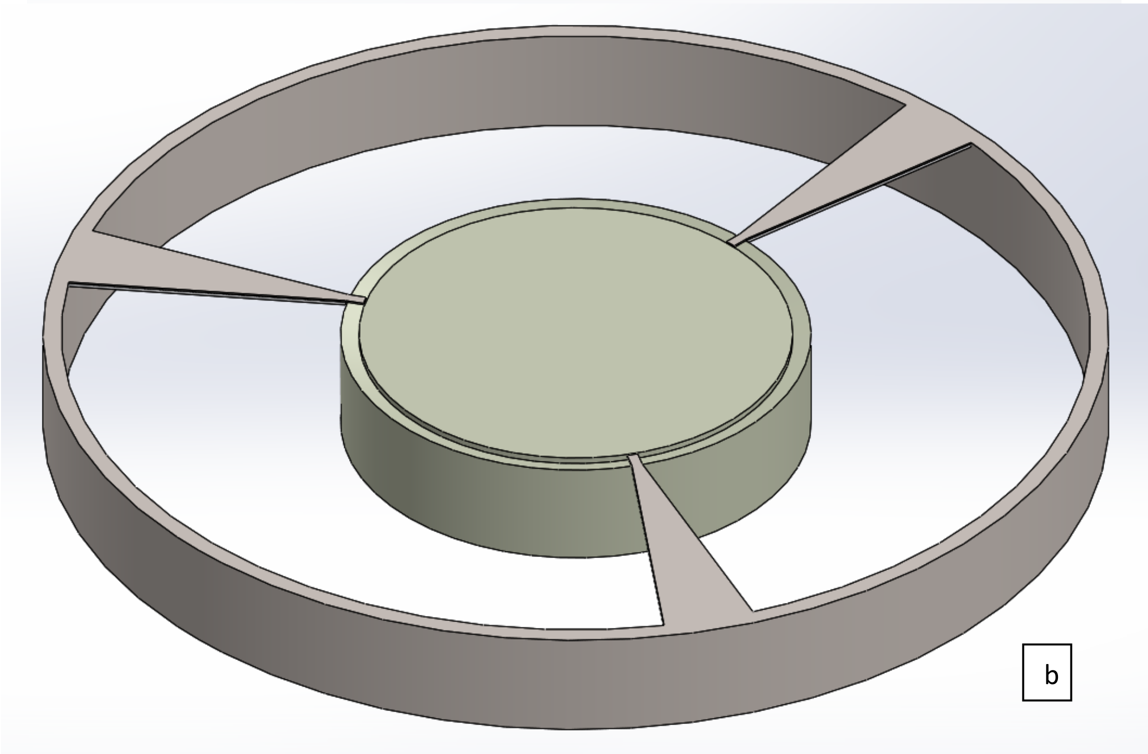
b

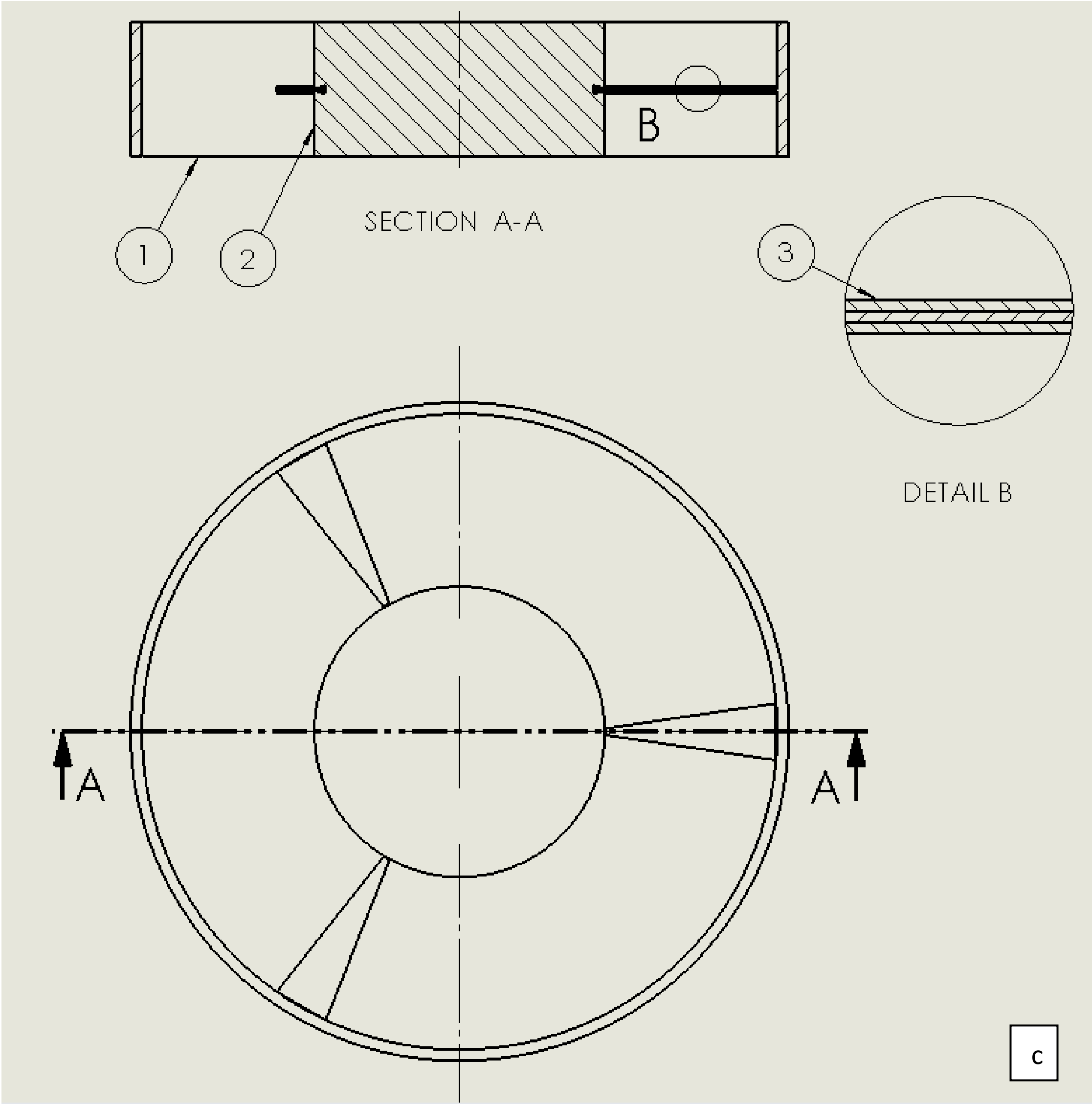

Figure 8.11. *Energy harvester device: three dimensional view (a), sectioned three dimensional view (b) and technical design (c)*

The bill of materials for the designed components (negligible parts are omitted) is:

Table 8.6. *BOM of the designed device*

Number	**Component**	**Material**	**Quantity**
1	Support	Ti-6Al-4V	1
2	Tip mass	Tungsten	1
3	Piezoelectric layer	0.08wt%Ga_2O_3-BCTZ	6

In conclusion, an energy harvester can be preliminary designed respecting the more and more stringent space and power requirements that biomedical applications need. This approach can be a starting step in order to get simple-shaped piezoelectric-based energy harvesting systems, that can be improved by an heterogeneous team of surgeons, mechanical and electronic engineers.

Materials can be studied deeply in order to get higher efficiencies, although gallium oxide-doped BCTZ is a promising piezoelectric material for this application. Recently, natural onion skin has been used to fabricate bio-piezoelectric nanogenerators with high energy conversion efficiency, showing the great variety of possible materials suitable in biomedical field [70].

9. CONCLUSION

Additive manufacturing presents a great variety of possible printable micro scale components and research tries always to reach an incremented level of miniaturization. In next years, improved new AM machines will be shown on the market in order to print smaller and smaller features, until the nanoscale will be obtained. At the moment, already important progress have been done, but new applications, in medical and electronic fields especially, will need more stringent space requirements. Hence, it is important to keep on elaborating on this topic.

10. REFERENCES

1. K. Satish Prakash, T. Nancharaih, V. V. Subba Rao, *Additive Manufacturing Techniques in Manufacturing - An Overview,* Materials Today: Proceedings 5, 3873-3882, Elsevier Ltd. (2018)
2. W. S. W. Harun, M. S. I. N. Kamariah, N. Muhamad, S. A. C. Ghani, F. Ahmad, Z. Mohamed, *A review of powder additive manufacturing processes for metallic biomaterials,* Powder Technology 327, 128-151, Elsevier Ltd. (2018)
3. Available online: https://it.wikipedia.org/wiki/Prototipazione_rapida#Le_tecniche_RP
4. S. A. Mantri, R. Banerjee, *Microstructure and micro-texture evolution of additively manufactured β-Ti alloys,* Additive Manufacturing 23, 86-98, Elsevier Ltd. (2018)
5. F. Krujatz, A. Lode, J. Seidel, T. Bley, M. Gelinsky, J. Steingroewer, *Additive Biotech-Chances, challenges and recent applications of additive manufacturing technologies in biotechnology,* New BIOTECHNOLOGY 39, 222-231, Elsevier Ltd. (2017)
6. T. D. Ngo, A. Kashani, G. Imbalzano, K. T. Q. Nguyen, D. Hui, *Additive manufacturing (3D printing): A review of materials, methods, applications and challenges,* Composites Part B 143, 172-196, Elsevier Ltd. (2018)
7. E. D. Burnham-Fay, T. Le, J. A. Tarbutton, J. D. Ellis, *Strain characteristics of additive manufactured polyvinylidene fluoride (PVDF) actuators,* Sensors and Actuators A 266, 85-92, Elsevier Ltd. (2018)
8. A. Vyatskikh, S. Delalande, A. Kudo, X. Zhang, C. M. Portela, J. R. Greer, *Additive manufacturing of 3D nano-architected metals,* NATURE COMMUNICATIONS, 9-593 (2018)
9. S. Bose, D. Ke, H. Sahasrabudhe, A. Bandyopadhyay, *Additive manufacturing of biomaterials,* Progress in Materials Science 93, 45-111, Elsevier Ltd. (2018)

10. R. D. Sochol, E. Sweet, C. C. Glick, S. Wu, C. Yang, M. Restaino, L. Lin, *3D printed microfluidics and microelectronics,* Microelectronic Engineering 189, 52-68, Elsevier Ltd. (2018)

11. A. C. de Leon, Q. Chen, N. B. Palaganas, J. O. Palaganas, J. Manapat, R. C. Advincula, *High performance polymer nanocomposites for additive manufacturing applications,* Reactive and Functional Polymers 103, 141-155, Elsevier Ltd. (2016)

12. C. Vyas, R. Pereira, B. Huang, F. Liu, W. Wang, P. Bartolo, *Engineering the vasculature with additive manufacturing,* Current Opinion in Biomedical Engineering 2, 1-13, Elsevier Ltd. (2017)

13. Available online: https://www.custompartnet.com/wu/fused-deposition-modeling

14. Available online: https://www.custompartnet.com/wu/laminated-object-manufacturing

15. Available online: http://insite.cavs.msstate.edu/publications/docs/2007/12/174218_JMSE2007.pdf

16. Available online: https://www.custompartnet.com/wu/3d-printing

17. Available online: https://www.custompartnet.com/wu/stereolithography

18. Available online: https://www.custompartnet.com/wu/selective-laser-sintering

19. Available online: https://www.custompartnet.com/wu/ink-jet-printing

20. Available online: https://www.custompartnet.com/wu/jetted-photopolymer

21. M. K. Thompson, L. H. Clemmensen, *Generalized requirements and decompositions for the design of test parts for micro additive manufacturing research,* Procedia CIRP 34, 229-235, Elsevier Ltd. (2015)

22. M. K. Thompson, M. Mischkot, *Design of test parts to characterize micro additive manufacturing processes,* Procedia CIRP 34, 223-228, Elsevier Ltd. (2015)

23. F. Liravi, M. Vlasea, *Powder bed binder jetting additive manufacturing of silicone structures,* Additive Manufacturing 21, 112-124, Elsevier Ltd. (2018)

24. F. Liravi, E. Toyserkani, *A hybrid additive manufacturing method for the fabrication of silicone bio-structures: 3D printing optimization and surface characterization,* Materials and Design 138, 46-61, Elsevier Ltd. (2018)

25. A. Davoudinejad, L. C. Diaz-Perez, D. Quagliotti, D. B. Pedersen, J. A. Albajez-Garcìa, J. A. Jagüe-Fabra, G. Tosello, *Additive manufacturing with vat polymerization method for precision polymer micro components production,* Procedia CIRP 75, 98-102, Elsevier Ltd. (2018)

26. X. Chen, H. O. T. Ware, E. Baker, W. Chu, J. Hu, C. Sun, *The development of an all-polymer-based piezoelectric photocurable resin for additive manufacturing,* Procedia CIRP 65, 157-162, Elsevier Ltd. (2017)

27. J. Tarbutton, T. Le, G. Helfrich, M. Kirkpatrick, *Phase transformation and shock sensor response of additively manufactured piezoelectric PVDF,* Procedia Manufacturing 10, 982-989, Elsevier Ltd. (2017)

28. N. Li, S. Huang, G. Zhang, R. Qin, W. Liu, H. Xiong, G. Shi, J. Blackburn, *Progress in Additive Manufacturing on New Materials,* Materials Science and Technology (2018)

29. S. Westbeek, J. A. W. van Dommelen, J. J. C. Remmers, M. G. D. Geers, *Influence of particle shape in the additive manufacturing process for ceramics,* Computers and Mathematics with Application, Elsevier Ltd. (2018)

30. S. Martìnez-Pellitero, M. A. Castro, A. I. Fernàndez-Abia, S. Gonzàlez, E. Cuesta, *Analysis of influence factors on part quality in micro-SLA technology,* Procedia manufacturing 13, 856-863, Elsevier Ltd. (2017)

31. Z. Chen, X. Song, L. Lei, X. Chen, C. Fei, C. T. Chiu, X. Qian, T. Ma, Y. Yang, K. Shung, Y. Chen, Q. Zhou, *3D printing of piezoelectric element for energy focusing and ultrasonic sensing,* Nano Energy 27, 78-86, Elsevier Ltd. (2016)

32. H. Xing, B. Zou, Q. Lai, C. Huang, Q. Chen, X. Fu, Z. Shi, *Preparation and characterization of UV curable Al_2O_3 suspensions applying for stereolithography 3D printing ceramic microcomponent,* Powder Technology 338, 153-161, Elsevier Ltd. (2018)

33. B. Derby, *Additive Manufacture of Ceramics Components by Inkjet Printing,* Engineering 1, 113-123 (2015)

34. Available online: https://pubs.acs.org/doi/10.1021/la204440w

35. S. P. Bathurst, S. G. Kim, *Printing of uniform PZT thin films for MEMS applications,* CIRP Annals – Manufacturing Technology 62, 227-230, Elsevier Ltd. (2013)

36. Editorial, *Highlights of the special issue on metal additive manufacturing,* Materials Characterization 143, 1-4, Elsevier Ltd. (2018)

37. K. L. Kirsch, K. A. Thole, *Isolating the effects of surface roughness versus well shape in numerically optimized, additively manufactured micro cooling channels,* Experimental Thermal and Fluid Science 98, 227-238, Elsevier Ltd. (2018)

38. O. Gharbi, D. Jiang, D. R. Feenstra, S. K. Kairy, Y. Wu, C. R. Hutchinson, N. Birbilis, *On the corrosion of additively manufactured aluminum alloy AA2024 prepared by selective laser melting,* Corrosion Science, Elsevier Ltd. (2018)

39. H. S. Fiaz, C. R. Settle, K. Hoshino, *Metal additive manufacturing for microelectromechanical systems: Titanium alloy (Ti-6Al-4V)-based nanopositioning flexure fabricated by electron beam melting,* Sensors and Actuators A 249, 284-293, Elsevier Ltd. (2016)

40. G. Rotella, S. Imbrogno, S. Candamano, D. Umbrello, *Surface integrity of machined additively manufactured Ti alloys,* Journal of Materials Processing Tech. 259, 180-185, Elsevier Ltd. (2018)

41. G. Bonaiti, P. Parenti, M. Annoni, S. Kapoor, *Micro-milling machinability of DED additive titanium Ti-6Al-4V,* Procedia Manufacturing 10, 497-509, Elsevier Ltd. (2017)

42. A. G. Demir, *Micro laser metal wire deposition for additive manufacturing of thin-walled structures,* Optics and Lasers in Engineering 100, 9-17, Elsevier Ltd. (2018)

43. G. Scotti, P. Kanninen, V. Matilainen, A. Salminen, T. Kallio, *Stainless steel micro fuel cells with enclosed channels by laser additive manufacturing,* Energy 106, 475-481, Elsevier Ltd. (2016)

44. P. Parandoush, D. Lin, *A review on additive manufacturing of polymer-fiber composites,* Composite Structures 182, 36-53, Elsevier Ltd. (2017)

45. Y. Hu, W. Cong, *A review on laser deposition-additive manufacturing of ceramics and ceramic reinforced metal matrix composites,* Ceramics International, Elsevier Ltd. (2018)

46. N. K. Roy, C. S. Foong, M. A. Cullinan, *Effect of size, morphology, and synthesis method on the thermal and sintering properties copper nanoparticles for use in microscale additive manufacturing processes,* Additive Manufacturing 21, 17-29, Elsevier Ltd. (2018)

47. Y. Chen, X. Bao, C. Wong, J. Cheng, H. Wu, H. Song, X. Ji, S. Wu, *Pzt ceramics fabricated based on stereolithography for an ultrasound transducer array application,* Ceramics International, Elsevier Ltd. (2018)

48. K. Gnanasekaran, T. Heijmans, S. van Bennekom, H. Woldhuis, S. Wijnia, G. de With, H. Friedrich, *3D printing of CNT- and graphene-based conductive polymer nanocomposites by fused deposition modeling,* Applied Materials Today 9, 21-28, Elsevier Ltd. (2017)

49. G. Postiglione, G. Natale, G. Griffini, M. Levi, S. Turri, *Conductive 3D microstructures by direct 3D printing of polymer/carbon nanotube nanocomposites via liquid deposition modeling,* Composites: Part A 76, 110-114, Elsevier Ltd. (2015)

50. M. Angjellari, E. Tamburri, L. Montaina, M. Natali, D. Passeri, M. Rossi, M. L. Terranova, *Beyond the concepts of nanocomposite and 3D printing: PVA and nanodiamonds for layer-by-layer additive manufacturing,* Materials and Design 119, 12-21, Elsevier Ltd. (2017)

51. N. S. Hmeidat, J. W. Kemp, B. G. Compton, *High-strength epoxy nanocomposites for 3D printing,* Composites Science and Technology 160, 9-20, Elsevier Ltd. (2018)

52. M. Seol, R. Ivaškevičiūtė, M. A. Ciappesoni, F. V. Thompson, D. Moon, S. J. Kim, S. J. Kim, J. Han, M. Meyyappan, *All 3D printed energy harvester for autonomous and sustainable resource utilization,* Nano Energy 52, 271-278, Elsevier Ltd. (2018)

53. Q. Yan, H. Dong, J. Su, J. Han, B. Song, Q. Wei, Y. Shi, *A Review of 3D Printing Technology for Medical Applications,* Engineering, Elsevier Ltd. (2018)

54. S. Bose, S. Ford Robertson, A. Bandyopadhyay, *Surface modification of biomaterials and biomedical devices using additive manufacturing,* Acta Biomaterialia 66, 6-22, Elsevier Ltd. (2018)

55. Available online: https://it.wikipedia.org/wiki/Pacemaker

56. Available online: https://www.farmacoecura.it/interventi/pacemaker-al-cuore-intervento-controindicazioni-cambiamenti-di-vita/

57. J. Z. Lee, S. K. Mulpuru, W. K. Shen, *Leadless pacemaker: Performance and complications,* Trends in Cardiovascular Medicine 28, 130-141, Elsevier Ltd. (2018)

58. M. F. El-Chami, F. M. Merchant, A. R. Leon, *Leadless Pacemakers,* Elsevier Ltd. (2016)

59. D. G. Della Rocca, C. Gianni, L. Di Biase, A. Natale, A. Al-Ahmad, *Leadless Pacemkaers: State of the Art and Future Perspectives,* Card Electrophysiol Clin 10, 17-29, Elsevier Ltd. (2018)

60. H. M. Seriwala, M. S. Khan, M. B. Munir, I. Riaz, H. Riaz, S. Saba, A. H. Voigt, *Leadless pacemakers: A new era in cardiac pacing,* Journal of Cardiology 67, 1-5, Elsevier Ltd. (2016)

61. N. Jackson, O. Z. Olszewski, C. O'Murchu, A. Mathewson, *Shock-induced aluminum nitride based MEMS energy harvester to power a leadless pacemaker,* Sensors and Actuators A 264, 212-218, Elsevier Ltd. (2017)

62. M. H. Ansari, M. A. Karami, *Experimental investigation of fan-folded piezoelectric energy harvesters for powering pacemakers,* Smart Materials and Structures, IOP Publishing 26 (2017)

63. A. Erturk, D. J. Inman, *An experimentally validated bimorph cantilever model for piezoelectric energy harvesting from base excitations,* Smart Materials and Structures, IOP Publishing 18 (2009)

64. A. Erturk, D. J. Inman, *Issues in mathematical modeling of piezoelectric energy harvesters,* Smart Materials and Structures, IOP Publishing 17 (2008)

65. T. Zheng, J. Wu, D. Xiao, J. Zhu, *Recent development in lead-free perovskite piezoelectric bulk materials,* Progress in Materials Science 98, 552-624, Elsevier Ltd. (2018)

66. S. Reddy, L. He, S. Ramakrishana, *Miniaturized-electroneurostimulators and self-powered/rechargeable implanted devices for electrical-stimulation therapy,* Biomedical Signal Processing and Control 41, 255-263, Elsevier Ltd. (2018)

67. J. Ma, X. Liu, W. Li, *High piezoelectric coefficient and temperature stability of Ga_2O_3-doped $(Ba_{0.99}Ca_{0.01})(Ti_{0.98}Zr_{0.02})O_3$ lead-free ceramics by low-temperature sintering,* Journal of Alloys and Compounds 581, 642-645, Elsevier Ltd. (2013)

68. P. Wang, Y. Li, Y. Lu, *Enhanced piezoelectric properties of $(Ba_{0.85}Ca_{0.15})(Ti_{0.9}Zr_{0.1})O_3$ lead-free ceramics by optimizing calcinations and sintering temperature,* Journal of the European Ceramic Society 31, 2005-2012, Elsevier Ltd. (2011)

69. Available online: http://www.2c2m.it/Argomenti/materiali/ceramici/rottfatica.htm

70. S. Maiti, S. K. Karan, J. Lee, A. K. Mishra, B. B. Khatua, J. K. Kim, *Bio-waste onion skin as an innovative nature-driven piezoelectric material with high energy conversion efficiency,* Nano Energy 42, 282-293, Elsevier Ltd. (2017)